Microstructure Map of 17-4 Precipitation Hardening Stainless Steel

by

Anne McDonald

A thesis submitted in partial fulfillment of the requirements for the degree of

Master of Science

in

Materials Engineering

Department of Chemical and Materials Engineering

University of Alberta

Abstract

17-4PH is a precipitation hardenable stainless steel alloy with good corrosion resistance and excellent mechanical properties. Due to this combination of properties, 17-4PH is used in a range of industries including marine, nuclear, aerospace, and paper. These wide industrial applications make 17-4PH an attractive candidate for additive manufacturing (AM) to enable on-the-spot replacement part printing at distributed work locations. To be used as an industrial AM alloy, the solidification behaviour of 17-4 PH must be well-understood.

To study the solidification behaviour of 17-4 PH, samples were created using differential scanning calorimetry (DSC), wire and arc additive manufacturing (WAAM), and impulse atomization (IA). In DSC samples that featured cooling rates from 2 - 20 °C/min, a martensitic matrix with interdendritic δ-ferrite was observed. To create uniform, single-pass beads using a WAAM system, a stable welding region was established for 17-4PH stainless steel over a torch travel speed of 4.1 - 2.5 $\frac{mm}{s}$ and a wire feed speed of 38.5 - 76.2 $\frac{mm}{s}$. These parameters gave current and voltage parameters of 80 - 130 A and 12 - 14 V, respectively, for an overall heat input range of 200 - 650 $\frac{J}{mm}$. The cooling rates, calculated from two-colour pyrometer data, ranged from 140 - 490 °C/s. The microstructure of the WAAM samples featured a largely columnar microstructure with a small equiaxed region at the surface of the bead. The phases of the WAAM samples, similar to those of the DSC, consisted of martensite and δ-ferrite. The fraction of δ-ferrite over the range of heat inputs

measured was fairly uniform, with an average δ-ferrite fraction of 0.21 ± 0.09 in the WAAM samples. The IA powders had a liquid cooling rate range of 600 - 12000 °C/s. In the IA samples, two major morphologies were observed, martensitic lathes and dendrites. Based on EBSD data, the dendrites were identified as δ-ferrite. At the lowest cooling rates, the powder particles were completely martensitic. As the cooling rate was increased, the alloy did not spend enough time in the austenite forming region of solidification and reached room temperature as δ-ferrite. Starting at cooling rates of 1900 °C/s, more than 50 % of the powder particles were fully δ-ferrite. At the highest cooling rates, more than 90 % of the powder experienced austenite by-passing and was fully δ-ferrite.

To further study the solidification behaviour of the WAAM beads over the cooling rates studied, the velocity of the solidification front in the beads was calculated from the angle of solidification of the columnar microstructure. As the heat input of the WAAM process was increased, a slight decrease in the angle of growth was observed. As WAAM is a consumable electrode process, the wire feed speed increases as the heat input increases. Due to this relationship, as the heat input was increased, a strong linear increase in bead area was observed. The velocity of solidification was normalized with respect to the cross-sectional bead area and the resulting normalized velocity of solidification decreased as the heat input was increased, reflecting a slower solidification front movement as the solidification cooling rate decreased.

To assess the effect of these microstructural changes on the properties of the alloy, microhardness measurements were taken for all the samples. From the DSC to the WAAM samples, the microhardness increased from 290 HV 0.5 to a maximum of 360 HV 0.5. These samples are composed of the same microstructural phases so this increase in hardness is likely due to grain refinement from the increasing cooling rate. The microhardness of the IA powders was around 290 HV 0.5 at all cooling rates measured. This significant drop in hardness at higher cooling rates is due to retained δ-ferrite in samples that appear fully martensitic.

Acknowledgements

First, I would like to thank my supervisor, Dr. Hani Henein, for his patience, trust, and guidance. I've learned so much from your breadth and depth of knowledge and drive for excellence. My other supervisor Kim Meszaros, for her strong voice and her photographic memory for welding standards. You have taught me so much about how to carry myself and working alongside you made me a better professional and researcher.

I owe thanks to my sponsors Syncrude, HI-AM, and NSERC without whose generous funding this research would not have been possible.

I would also like to thank all of my labmates for their friendship and advice, especially Dany, Vanda, and Shiyu for showing me how to use everything the first time and then helping me fix it when it broke.

Thank you to Drs. Paul Lu and Duane Szafron for getting me back on campus. This all started with you both. Most of all, thank you to my family. They don't give me enough pages to say here what your support and love mean.

Contents

List of Tables

List of Figures

Chapter 1

Introduction

17-4PH is a precipitation hardenable stainless steel alloy with good corrosion resistance and excellent mechanical properties. Due to this combination of properties, 17-4PH is used in a range of industries including marine, nuclear, aerospace, and paper. These wide industrial applications make 17-4PH an excellent candidate for additive manufacturing (AM) to enable on-the-spot replacement part printing at various distributed locations.

In order to confidently use 17-4PH in AM, more information is required on how rapid solidification affects the microstructure of the alloy. Additionally, as 17-4PH is used in its heat-treated form in order to nucleate and grow the copper precipitates that give the alloy its characteristic strength, most of the literature available is on the heat-treated microstructure. This work aims to create a microstructure map that tracks the evolution of the as-deposited microstructure of 17-4PH over a range of different heat inputs. To obtain high cooling rate samples with a well understood thermal history, 17-4 PH powder was created using impulse atomization (IA). To observe the as-deposited 17-4 PH in AM, wire and arc additive manufacturing (WAAM) was chosen for its promising industrial applications as a large-volume, high-throughput AM process. Finally samples were created at low cooling rates using differential scanning calorimetry (DSC).

The main objective of the microstructure map is to aid in the development of a digital database of the process-structure-property relationship for this alloy.

Chapter 2

Literature Review

2.1 Additive Manufacturing

Additive manufacturing (AM) is a manufacturing method that involves the fabrication of parts through joining of materials, usually in a layer-by-layer method, in a pattern defined by a 3D model [1]. Compared with traditional manufacturing methods, AM gives greater economic advantage for specialized parts, prototyping, or in situations where multiple parts can be replaced with a single, more complex shape [2]. Beyond the economic benefits, there is an environmental advantage to AM that makes it increasingly desirable. By building the desired part instead of machining it out of a bulk, less waste is created. Paired with AM design thinking, the final part can require less material than items manufactured by more traditional means [3]. In addition to less waste in building the final part, long supply chains can be avoided and part inventory reduced by using AM to repair existing tools or produce replicate parts on-site.

Within AM, there are seven main branches: vat photopolymerization, material jetting, powder bed fusion, directed energy deposition, material extrusion, binder jetting, and sheet lamination [2]. This work will focus on directed energy deposition (DED). DED is a method of AM that uses a heat source to fuse material, either to produce a coating, repair a previously-built piece, or produce a new, near-net part [4]. Specifically, the AM process considered in this work is wire and arc additive manufacturing (WAAM).

2.1.1 Wire and Arc Additive Manufacturing

Wire and arc additive manufacturing (WAAM) is defined as a DED AM process by ASTM F3413-19 [5]. A schematic of the WAAM set-up is shown in Figure 2.1.

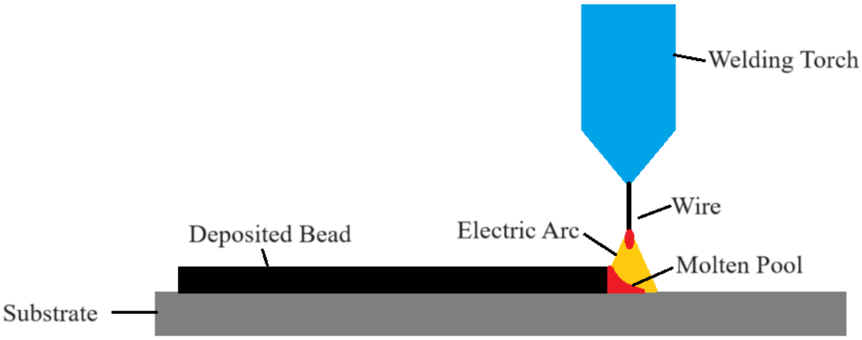

Figure 2.1: WAAM set-up schematic

A WAAM system consists of a wire feedstock and an electric arc heat source that can be a gas metal arc welding (GMAW), gas tungsten arc welding (GTAW), or plasma transferred arc (PTA) welding torch [6]. WAAM is attractive as an industrial AM process for a variety of reasons. Compared to powder-fed processes, WAAM has a significantly higher deposition rate, wire feedstock is less prone to porosity defects as it does not contain trapped gas, and the wire feedstock is safer as it eliminates the risk of inhalation [5], [6]. In applications with a high value feedstock, WAAM also provides benefits as wire is less expensive to manufacture than DED-grade metal powder and less material is wasted since all of the wire material is contacted by the arc and melted [5].

As WAAM is adapted from a welding process, it is sensitive to the same flaws and drawbacks as the traditional welding process it is based on. Welding manufacturers have created new welding technology to improve the characteristics of welds and help avoid common welding issues. One such technology is Fronius' cold metal transfer (CMT). CMT is an adapted GMAW short-circuit process that involves a controlled droplet transfer [6], [7]. When the wire begins to melt and a droplet forms, the wire continues to feed until the droplet contacts the melt pool. At the point of contact, a short circuit occurs and the arc is extinguished. In the CMT process, the wire is retracted at the moment of contact, while in traditional short-circuit GMAW the amperage is increased in order to pinch off the droplet and reestablish the arc [8]. By introducing a mechanical servo for more control over the wire movement, CMT has a lower heat input and the risk of splatter during droplet transfer is much reduced compared to traditional GMAW [6], [7], [9].

2.1.2 Challenges of AM

Though AM is a promising processing route, there are still many challenges related to its use that must be addressed [3]. New parameters must be established compared to welding in order to build parts, as the heat input requirements for AM are much lower than traditional welding to maintain part integrity during building. Similar to multi-pass traditional welding, previous layers are re-melted or heated by subsequent welding passes leading to microstructural changes that can be hard to predict or characterize. These complex thermal cycles can also contribute to large residual stresses within the final parts. Additionally, while complex shapes are one of the promising final products of AM, dimensional accuracy is still a challenge for many methods and a post-build machining step must be implemented. This post-build machining can be very difficult and time consuming for intricate parts, contributing to cost and manufacturing time [10].

2.2 17-4 Precipitation Hardening Stainless Steel

17-4 precipitation hardening (PH) stainless steel (UNS S17400, Type 630) is a grade of stainless steel employed widely across many industries with composition limits defined by ASTM A564 as seen in Table 2.1. The combination of excellent strength and hardness and good corrosion resistance makes 17-4 PH a good fit for applications in chemical and power plants, nuclear and marine industries, and aerospace [11]–[13]. PH stainless steels are designed to achieve their primary hardening through the precipitation of a secondary phase during heat treatment. In 17-4 PH, this phase is a coherent FCC copper precipitate in the martensitic matrix [11], [12].

Table 2.1: 17-4 PH Composition Ranges [14]

Element	**Composition Limit (wt%)**
C	0.07
Mn	1.00
Si	1.00
P	0.040
S	0.030
Cu	3.00-5.00
Ni	3.00-5.00
Cr	15.00-17.50
Nb & Ta	0.15-0.25

2.2.1 Weldability

Precipitation hardening stainless steels have been shown to be weldable– an important consideration when choosing feedstock material for a DED-type AM process [15]–[19]. The procedure for welding PH steels is similar to any 300-series stainless steel and the welds are not sensitive to cracking and do not require a preheat [18]. It is possible to achieve comparable mechanical properties to cast or wrought 17-4 PH when using it as a filler metal and only slight modifications to chemistry are required to obtain better weldability [15], [18]. Multiple studies have shown worsened mechanical properties in the as-deposited weld material and in the heat affected zone (HAZ) of the 17-4 PH base metal. This softening effect is the result of an increase in retained austenite and a redissolving of any precipitates [20]. When an aging treatment was applied to single-pass welded samples without a solutionizing step, the tensile and yield strengths as well as the hardness conformed to the properties of the cast alloy but the ductility, as represented by the percent elongation, was very poor [21]. This poor ductility stemmed from the formation of full dendritic network of δ-ferrite through the martensitic matrix. A full post-weld heat treatment (PWHT) was already required for any multi-pass weld due the effect of subsequent passes on the as-deposited microstructure. It was shown in multiple studies that any 17-4 PH weld sample that was given the full solutionize and aging treatment common to the alloy, regained the characteristic strength, ductility, and hardness of the alloy [20]–[22].

2.2.2 Microstructure

17-4 PH is classified as a martensitic, precipitation-hardenable stainless steel. Every stainless steel, depending on its ratio of austenite stabilizing to ferrite stabilizing elements will experience one of five solidification paths – single-phase ferrite (F) or austenite (A), primary-phase ferrite with secondary phase austenite (FA), primary-phase austenite with secondary phase ferrite (AF), or eutectic ferrite and austenite (E) [23], [24]. A vertical section of the Fe-Cr-Ni phase diagram is displayed in Figure 2.2. The simplified diagram illustrates the relationship between the Cr/Ni ratio and the solidification path of stainless steels.

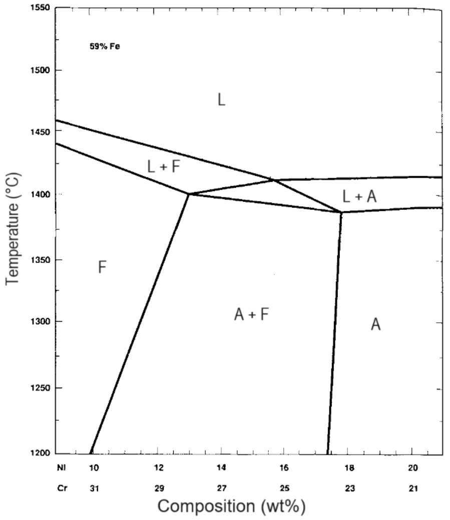

Figure 2.2: Fe-Cr-Ni phase diagram for 59% Fe (Adapted from [24])

A common way to predict the final solidification structure of a stainless steel is using the Schaeffler diagram. Schaeffler diagrams provide a formula to calculate the ratio of Cr equivalent alloying elements (ferrite stabilizers) to Ni equivalent alloying elements (austenite stabilizers)[25]. In addition to the five solidification paths mentioned above, stainless steels can also form martensite if the conditions and compositions are correct. As seen in Figure 2.3, final ferrite, austenite, and martensite phases are all predicted on the Schaeffler diagram represented as F, A, and M respectively.

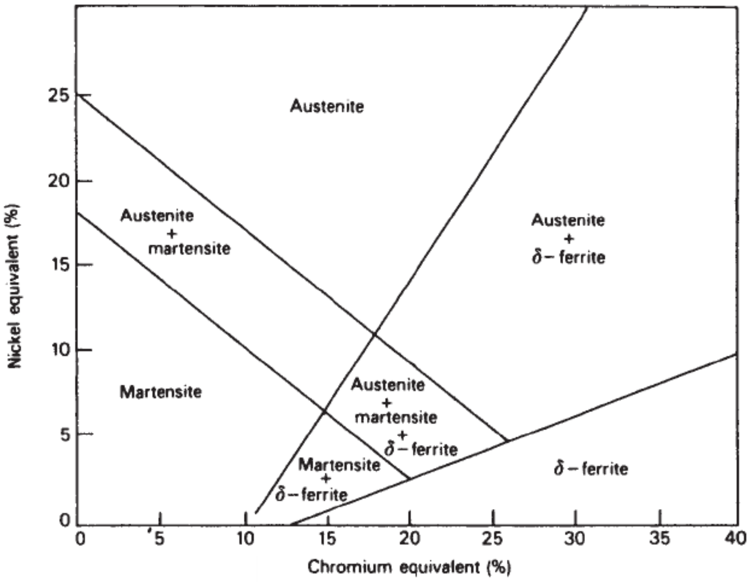

Figure 2.3: Schaeffler diagram [26]

The Schaeffler diagram does not take into account the effect of nitrogen as an austenite stabilizer, later work by DeLong included a $30x\%N$ factor to the Ni_{eq} equation [17]. Further work by the Welding Research Council considered the effect of copper on ferrite percentages, resulting in the WRC-1992 equations and diagram which give very good ferrite predictions. However, WRC-1992 does not consider the effect of Mn, an alloying element that contributes to the stability of austenite at low temperatures, and therefore cannot be used like the Schaeffler diagram in predicting martensite [17].

17-4 PH has Schaeffler 1949 Cr_{eq} and Ni_{eq} values of roughly 16 and 5, respectively. These Cr_{eq} and Ni_{eq} values put the alloy in the M + F solidification zone of the Schaeffler diagram. The solidification path of 17-4PH has been found to be L $\rightarrow$ F $\rightarrow$ F + A $\rightarrow$ M which agrees with the Schaeffler prediction [20], [27]. The alloy is designed to have a martensite start temperature of 95 - 150 °C giving a very complete transformation from austenite to martensite upon cooling to room temperature without a subzero quench required[16], [18], [28]. Commercial 17-4 PH products are typically available in

Condition A or in a fully aged condition. Condition A, or annealed condition, involves a solution heat treatment at 1038 °C for one hour, followed by an air cool [12], [16]. There are various aging heat treatments available depending on the desired final properties or service conditions. A list of aging temperatures and times can be seen in Table 2.2.

Table 2.2: 17-4 PH Aging Heat Treatments

Condition	**Temperature (°C)**	**Time (hours)**
H900	482	1
H925	496	4
H1025	551	4
H1075	580	4
H1150	621	4

In all cases, the final heat treated structure of 17-4 PH is a tempered martensite with minimal δ-ferrite and retained austenite. In the aged condition, the copper is precipitated out as coherent BCC Cu precipitates that can transform into incoherent, FCC $\mathcal{E}$-Cu precipitates upon over-aging [16]. 17-4 PH produced through traditional manufacturing routes has a microstructure that is composed of a martensitic matrix with δ-ferrite stringers. In the case of rolled material, the δ-ferrite stringers are oriented in the rolling direction and usually make up less than 10% of the overall microstructure [29], [30]. An example of 17-4 PH microstructure from a solution-treated round bar can be seen in Figure 2.4. In the micrographs shown, the prior austenite grain boundaries are well visualized indicating that the martensite packets did not propagate across the austenite grain boundaries when they formed [30].

While the final heat-treated microstructure is well understood, the initial solidification microstructure of 17-4 PH can be more complex, especially under the rapid solidification conditions seen in welding and AM applications. While there has not been much comprehensive work on phase formation during welding of 17-4 PH stainless steel, the work that has been done on other stainless steels can be useful to the understanding of 17-4 PH weld metal solidification. Before the austenite transforms to martensite on cooling, 17-4 PH shares a solidification path with FA stainless steels.

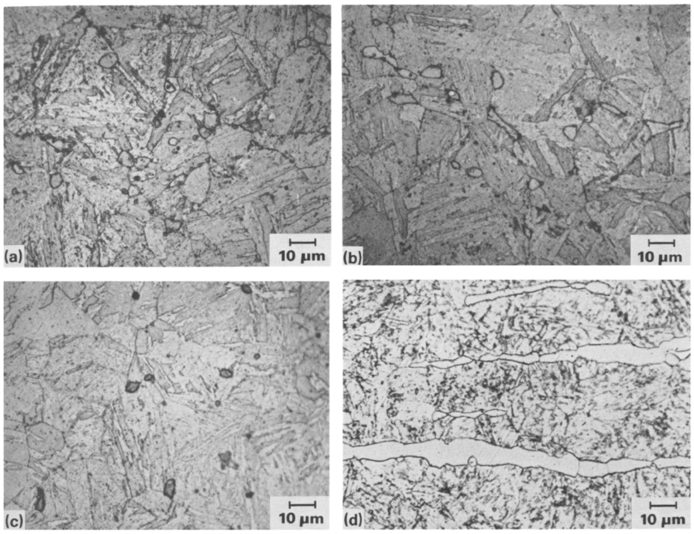

Figure 2.4: Microstructure of round bar where (a)-(c) are transverse cross-sections to show martensite matrix with δ-ferrite and carbides precipitates and (d) is a longitudinal cross-section showing large δ-ferrite stringers [30]

Duplex stainless steels are steels designed to consist of a balanced ratio of both δ-ferrite and austenite in their final structure [31]. In these alloys, since δ-ferrite does not completely transform to austenite, the nucleation behaviour of austenite can be observed. After the primary ferrite phase forms, it is common for austenite to form at the ferrite grain boundaries and then grow into the prior ferrite grains in a Widmanstätten structure [24], [25], [32]. An example of this allotriomorphic structure that has grown into Widmanstätten needles can be seen in Figure 2.5. This Widmanstätten morphology is a common and well-known structure in welding metallurgy [25], [33]. In Figure 2.6, the allotriomorphic austenite nucleation and growth can be seen along the former ferrite grain boundaries. In Figure 2.7, the austenite nucleation and growth can be seen as the lighter phase, with a clear Widmanstätten needle growing on the left of the image.

In FA stainless steels with a more complete transformation of δ-ferrite into austenite, the untransformed δ-ferrite appears in the structure in two major morphologies - vermicular (or skeletal) ferrite and lathy (or lacy) ferrite [34]. Studies of 304 stainless steel, an FA stainless steel, showed that the as-welded structure consists of austenite with a small remaining fraction of δ-ferrite.

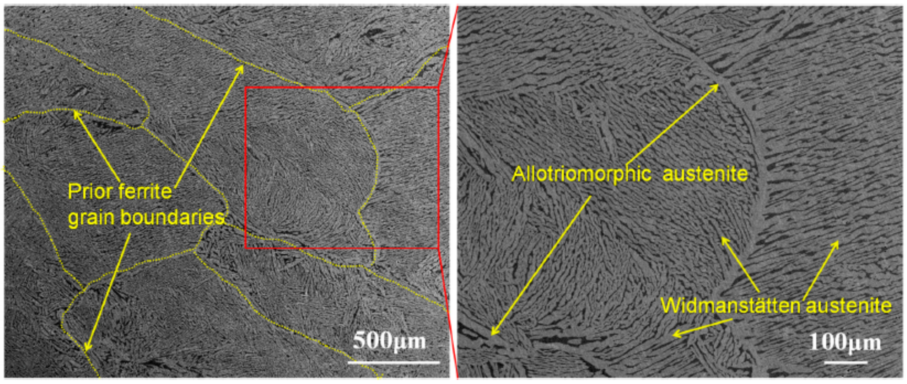

Figure 2.5: Austenite Widmanstätten needles in a ferrite matrix [32]

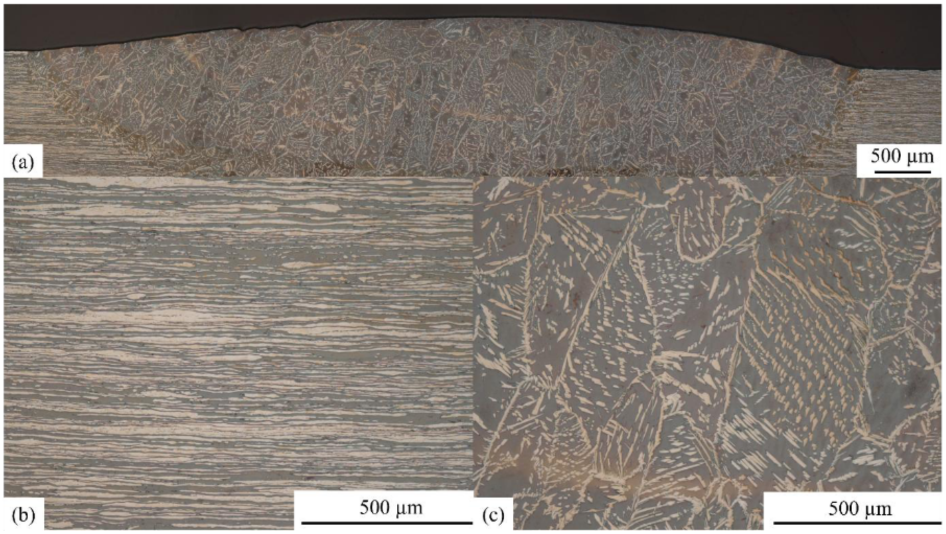

Figure 2.6: Allotriomorphic austenite growth in a ferrite matrix [31]

Examples of skeletal and lathy ferrite in these can be seen in Figure 2.8.

The orientation of the austenite and ferrite with respect to one another is what governs whether the remaining ferrite in the structure is vermicular or lathy after solidification [24], [34].

2.2.3 Effect of Rapid Solidification on Microstructure

While the Schaeffler diagram is a widely used tool due to its general accuracy in predicting final weld structure, the cooling rate can have an effect on the solidification microstructure that is not captured. Studies on the effect of cooling rate on the accuracy of Schaeffler showed that at very high cooling rates, the Schaeffler diagram did not always accurately predict the final microstructure

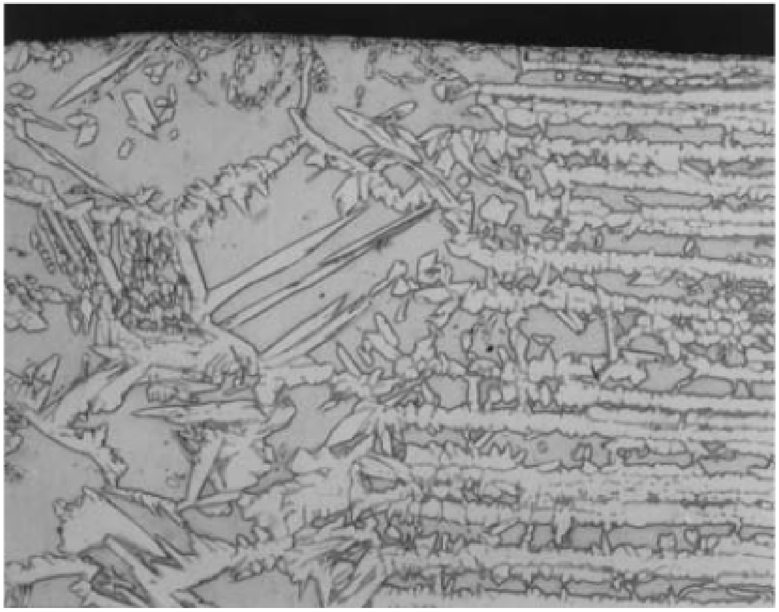

Figure 2.7: Austenite growth in a duplex stainless steel weld [33]

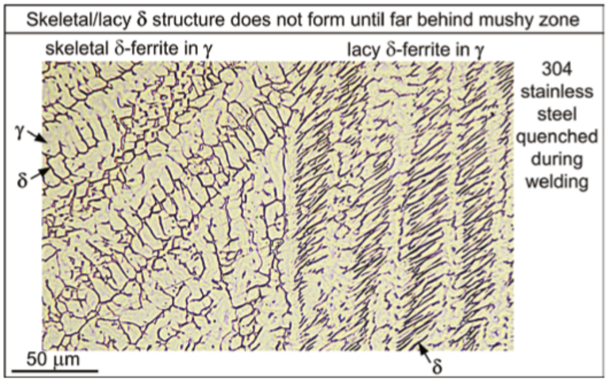

Figure 2.8: Quenched weld microstructure of 304 stainless steel showing skeletal (SF) and lathy (LF) ferrite [34]

[35]. In this study, steels with various Cr_{eq}/Ni_{eq} were cast into ingots and hot rolled before autogenous laser welding occurred. The resulting laser weld microstructure was observed and the cooling rate was calculated [35]. Many of the steels studied showed significantly altered microstructures at the highest cooling rates of $1.2*10^6$ $°C/s$. In the case of high Cr_{eq}/Ni_{eq} steels that formed duplex microstructures under normal welding conditions, a fully ferritic microstructure was observed at the highest laser speeds showing that the steels were capable of completely bypassing the transition to austenite [35]. In order to account for the effect of cooling rate on solidification mode, the authors

recommend some alterations to the Cr_{eq}/Ni_{eq} calculations to more accurately predict ferrite fraction. However, their alterations only affect extremely high cooling rates, as up to 7000 $°C/s$ they saw very good fit with the Schaeffler predictions [35].

While there has not been a comprehensive study on the effect of high cooling rates on 17-4 PH microstructure, the effect of different AM processes on the initial solidification microstructure has been observed in some cases. For a reference of conditions in each study, the cooling rate of common welding processes can be seen in Table 2.3.

Table 2.3: Estimated cooling rates for common welding processes [24]

Process	**Cooling Rate (K/s)**
Arc Welding	10^1 to 10^3
Electron Beam Welding	10^2 to 10^4
Laser Beam Welding	10^2 to 10^6

It should also be noted that various studies discussed have used XRD to identify the microstructural phases present in samples of 17-4 PH. However, because 17-4 PH has a very low carbon content, XRD cannot distinguish between martensite and δ-ferrite. Martensite has a body centered tetragonal (BCT) microstructure but in steels with less than 0.2% C, the c/a ratio approaches that of BCC [36]–[39]. These very similar lattice parameters means that the BCC structure identified by XRD or EBSD techniques can be either martensite or δ-ferrite, making microstructure identification not a trivial task.

In a study by Ziewiec et. al., 17-4 PH welds were created using a GTAW without a filler material [27]. The resulting as-welded microstructure was a majority martensitic matrix with a fraction of untransformed δ-ferrite retained at the grain boundaries. As seen in Figure 2.9, the δ-ferrite appears in the vermicular morphology. In addition, as seen in region 2 in Figure 2.10, a very continuous δ-ferrite network can be observed in the heat affected zone (HAZ) of the weld. It has been observed in many GTAW studies of 17-4 PH that the cooling rates using this welding method are high enough to suppress the solid state diffusion required for the transformation of δ-ferrite to austenite and result in a duplex martensite-ferrite structure [22], [27], [40].

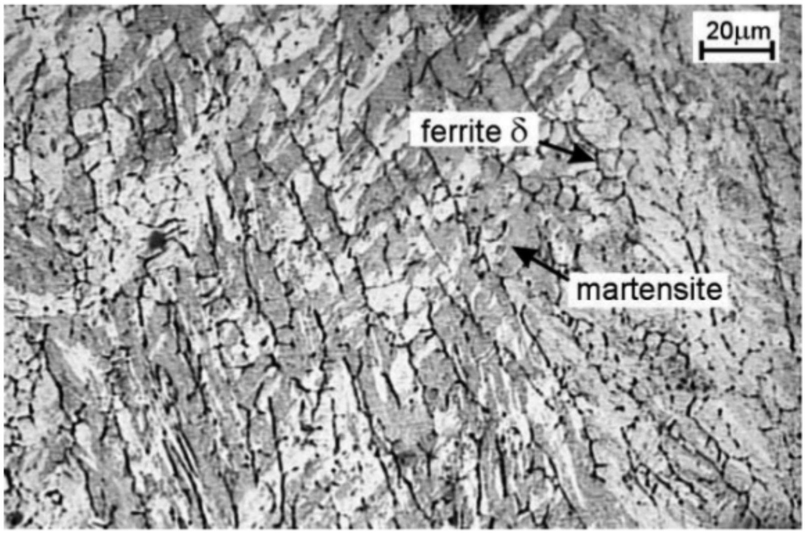

Figure 2.9: As-welded 17-4 PH martensitic and δ-ferrite microstructure [27]

Another study, by Hamlin, was also done using autogenous GTAW welds on 17-4 PH plates [22]. These welds, designed to study the potential of depositing 17-4 PH overlays, were performed at heat inputs of up to 2000 $\frac{J}{mm}$ [22]. While the heat input in this study is more than twice that of the Ziewiec study, the as-solidified structure still consists of a martensitic matrix with δ-ferrite retained at the grain boundaries [22], [27]. This microstructure can be observed in Figure 2.11 with the martensite labelled as as-quenched martensite (AQM) and the ferrite as δ.

Only one study, by Caballero et. al., has been published on the use of WAAM with 17-4 PH. Using a Fronius cold metal transfer (CMT) power source and a 38% He and 2% CO_2 in argon shielding gas inside an argon filled chamber, a wall was built on a 12 mm thick 304 stainless steel substrate [20]. The as-deposited microstructure featured a dendritic martensitic matrix with interdendritc δ-ferrite (Figure 2.12).

Using the same WAAM set-up as described above, the effect of shielding gas on the amount of retained austenite was observed using EBSD. In Figure 2.13, the EBSD phase maps of two different samples are shown. In 2.13(a) the sample was built using the 38% He and 2% CO_2 in argon shielding gas and in 2.13(b) the sample was built using a 2.5% CO_2 in argon shielding gas [20]. Red in the colour map represents BCC microstructure and blue is FCC.

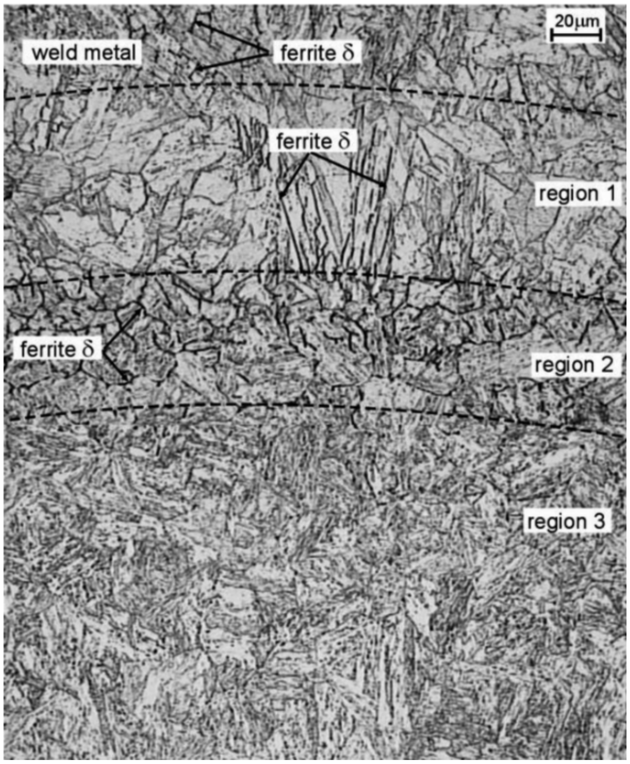

Figure 2.10: As-welded fusion zone showing continuous δ-ferrite network in martensitic matrix [27]

On the right, the FCC phase fraction of the images have been isolated. It can be seen that by removing the He fraction of the shielding gas, the heat input is lower and the cooling rate of the sample is faster [20]. This faster cooling rate results in a smaller grain size. It has been shown that the smaller the original austenite grain size, the greater the energy barrier for the martensite transformation and, as a result, the great fraction of retained austenite [20], [41], [42].

The plasma-based welding and AM studies observed have shown the existence of metastable states in rapidly cooled 17-4 PH samples. As seen in Table 2.3, the cooling rate in laser-based welding or AM is orders of magnitude faster than in plasma-based processes. Looking at samples produced through laser-based methods, more significant fractions of metastable phases can be found.

In a study by Facchini et. al., 17-4 PH samples were produced using selective laser melting (SLM) from argon atomized metal powder. The as-cast

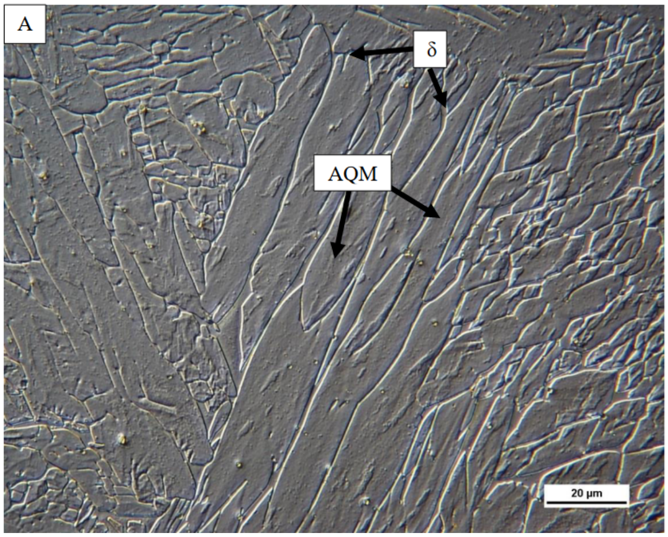

Figure 2.11: As-welded 17-4 PH with a martensite and δ-ferrite structure [22]

samples in this study were heat treated at 600°C for 2 h to relieve residual stress from printing before they were able to be removed from the base plate and analyzed. In Figure 2.14, the microstructure of the as-built part can be seen in 2.14a. The large grains with fine dendrites in the substructure that are characteristic of the SLM process can be seen [43]. XRD analysis (2.14b) shows that the sample is about 72% austenite and 28% martensite [43].

Other studies have replicated the existence of a metastable or retained austenite in SLM. All of these attribute the formation of austenite to an increase in nitrogen in the sample composition, a powerful austenite stabilizer [28], [44]–[46]. However, the majority of 17-4 PH SLM samples share a microstructure that consists of a martensite matrix with a very modest amount of retained austenite. This martensitic microstructure appears in the very fine columnar morphology that is characteristic of the very high cooling rates of SLM processes. An example of this can be seen in Figure 2.15, an SEM image of a transverse cross-section of an SLM printed part.

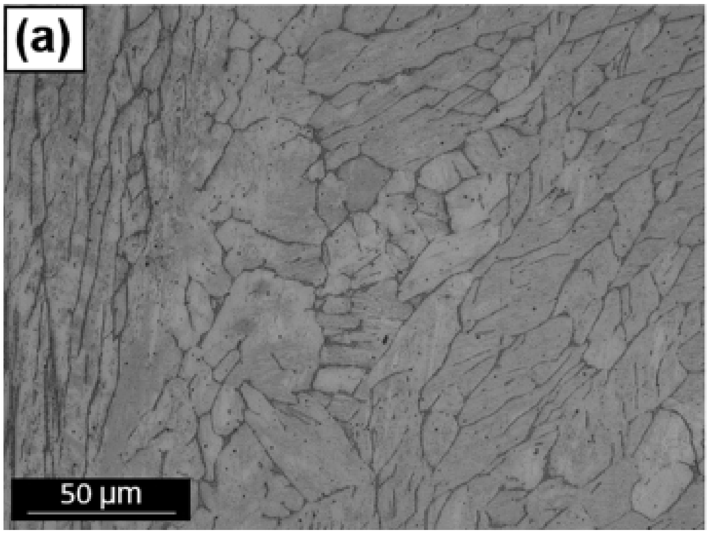

Figure 2.12: As-deposited microstructure of a WAAM wall built using a He-CO_2-Ar shielding gas mixture [20]

As previously discussed, studies have found the existence of a metastable ferrite morphology during rapid solidification of duplex stainless steels as in the work of David et. al. [35]. In a study by Alnajjar et. al., the phenomenon of austenite bypassing was observed in SLM samples of 17-4 PH [37]. Samples were observed to have a relatively coarse grained microstructure without martensitic lathes or other large misorientations that are characteristic of the structure (Figure 2.16). To analyse how this metastable phase could be formed, the thermal cycle of an SLM melt pool was studied. As shown in Figure 2.17, upon cooling and heating the thermal cycles are rapid enough that the material does not spend enough time in the austenite-forming temperature range for austenite formation to occur. Without this austenite formation, no martensite can form upon further cooling.

While austenite bypassing can occur at high cooling rates, not all high cooling rate samples are fully ferritic. In a study by Vunnam et. al., 17-4 PH samples were manufactured using SLM from powders with three different chemistries [39]. Using the WRC-1992 equations, Cr_{eq}/Ni_{eq} ratios were calculated for all three powders. The results of this can be seen in Table 2.4

When printed using the same SLM machine and identical process parameters the resulting microstructure varied greatly (Figure 2.18). In powders

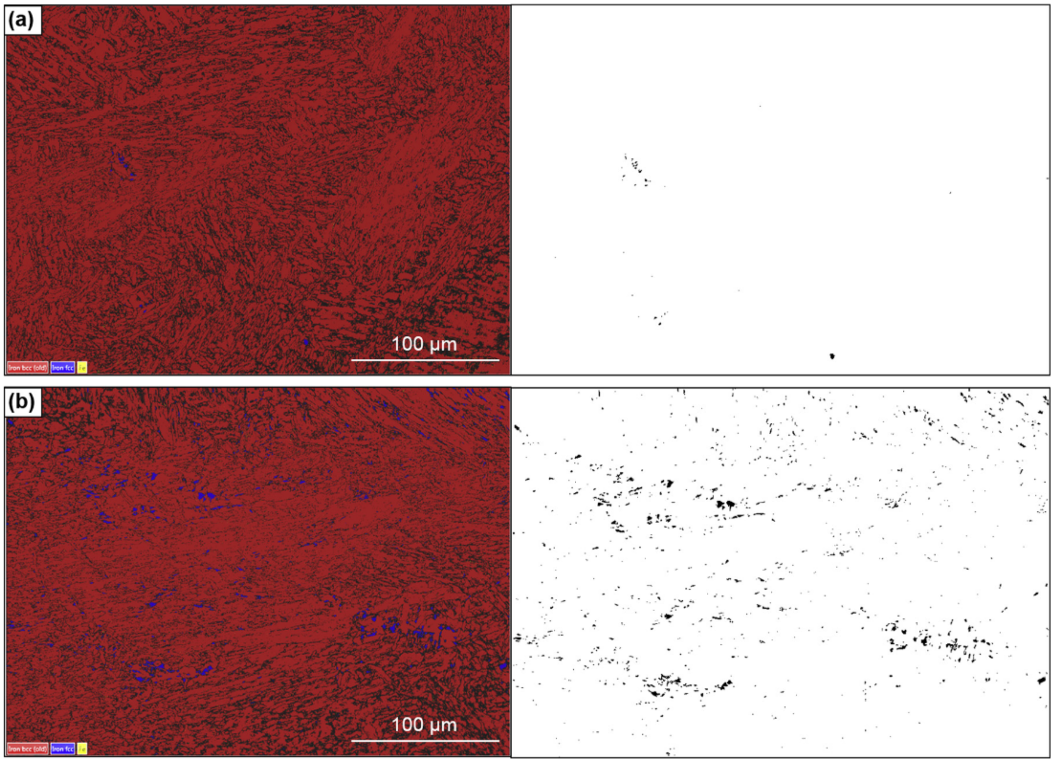

Figure 2.13: EBSD of as-deposited samples where (a) is the shielding gas that contains He and the (b) is the shielding gas without [20]

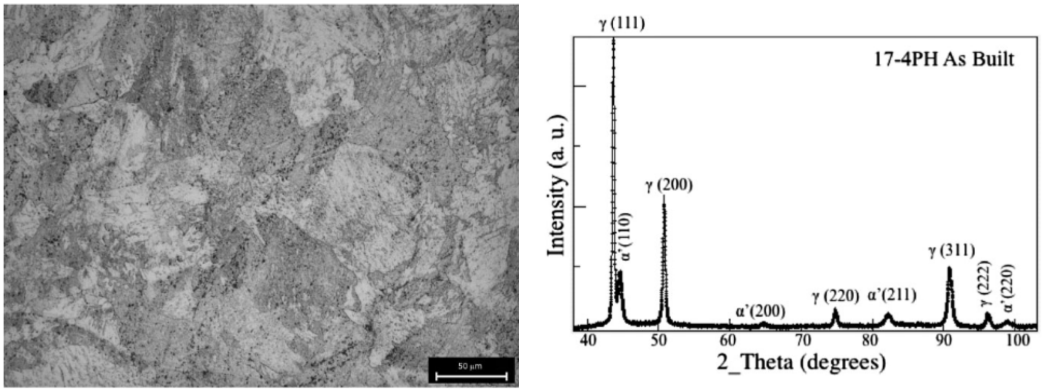

(a) SLM as-built microstructure

(b) SLM as-built XRD

Figure 2.14: As-built part assessment from an SLM process [43]

A and B, a coarse, columnar ferrite structure is observed, very similar to microstructures reported by Alnajjar et. al. [37]. However, in powder C samples, the microstructure is a very fine grained martensite with small fractions of retained austenite and δ-ferrite [39]. This change in final microstructure is attributed to the change in the temperature range where austenite forms.

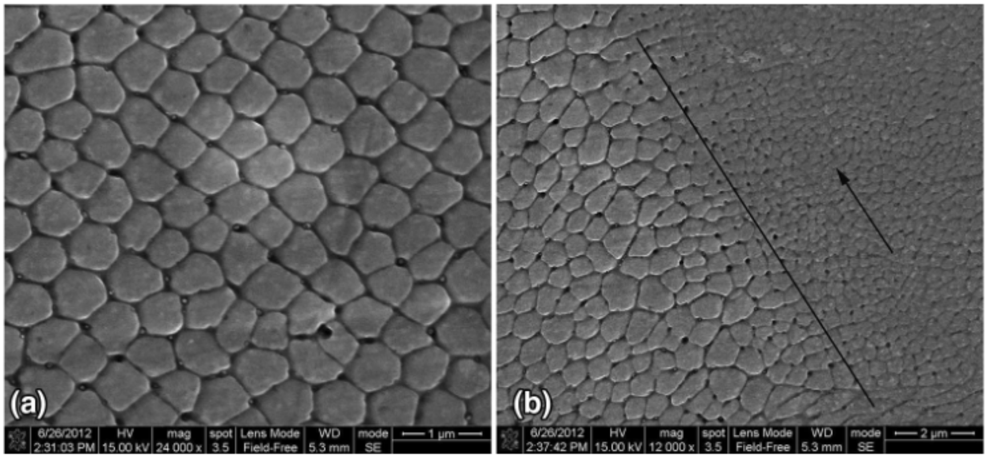

Figure 2.15: Transverse cross section of an SLM part where (b) shows the microstructural change between laser tracks [44]

Table 2.4: Cr_{eq}/Ni_{eq} ratios for three 17-4 PH powders [39]

Powder	Cr_{eq}/Ni_{eq}
A	2.81
B	2.65
C	2.36

When the range of temperatures that austenite forms over is extended, the austenite has more time to form in samples with the same cooling rate. In the case of the chemistries studied, powder C spent 700 μs in the austenite range compared to powder A which spent closer to 600 μs in the austenite-forming range [39].

These results have been duplicated in a work by Sabooni et. al. that found a distinct microstructural difference between SLM parts based on the Cr_{eq}/Ni_{eq} ratio [47]. The as-printed microstructures of the parts can be seen in Figure 2.19. It can be concluded that within the alloy definition of 17-4 PH stainless steel, feedstocks with a lower Cr_{eq}/Ni_{eq} ratio are more likely to form martensite at high cooling rates.

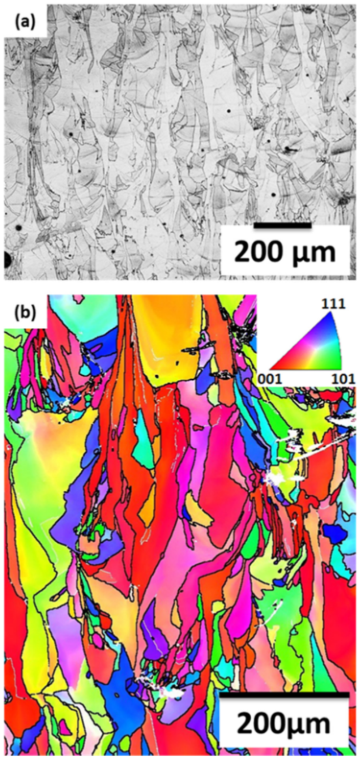

Figure 2.16: SEM and EBSD images of epitaxial grains in 17-4 PH SLM samples [37]

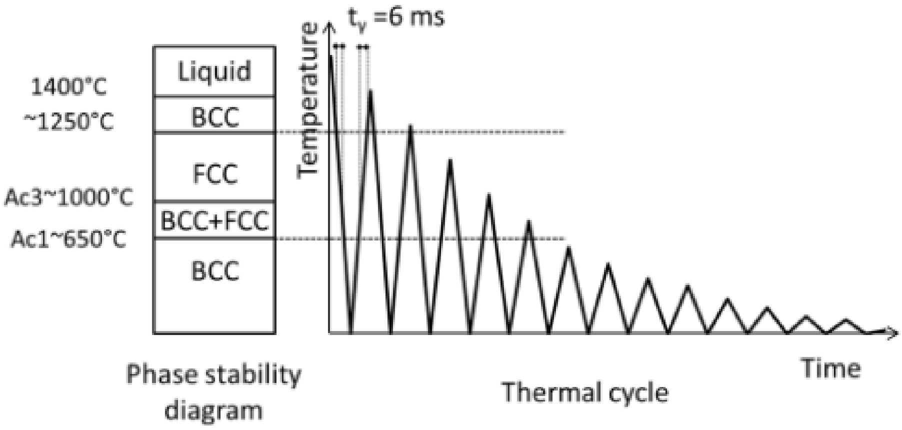

Figure 2.17: Schematic of SLM thermal cycles [37]

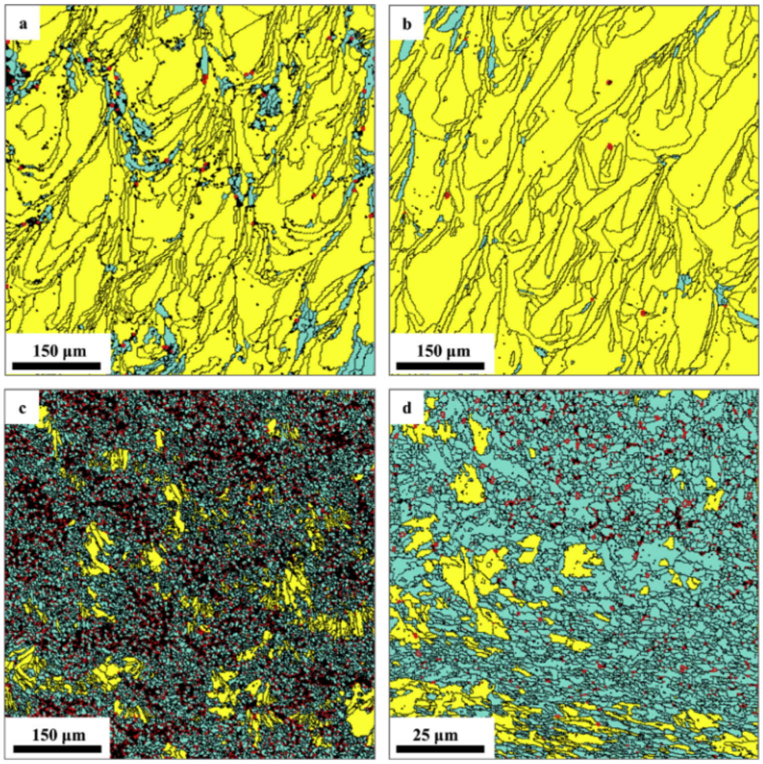

Figure 2.18: EBSD results showing austenite (red), ferrite (yellow), and martensite (blue) for powder a (a), powder b (b), and powder c (c and d) [39]

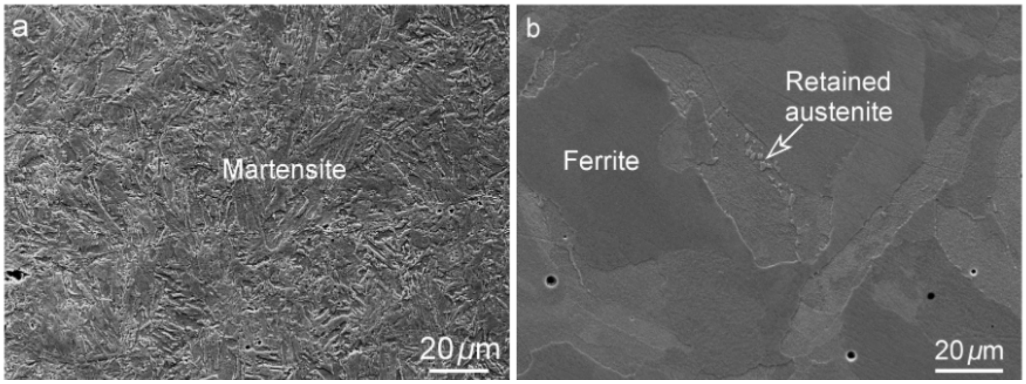

Figure 2.19: Micrographs of SLM parts made from a low Cr_{eq}/Ni_{eq} powder (a) and a high Cr_{eq}/Ni_{eq} powder (b) [47]

Chapter 3

Experimental Procedure

This chapter presents an overview of the methodology used to generate 17-4PH powder, 17-4PH additively manufactured samples, and to analyse the major features of all samples.

3.1 Impulse Atomization

Impulse atomization (IA) was done in a custom-built drop tower, a schematic of which can be seen in Figure 3.1.

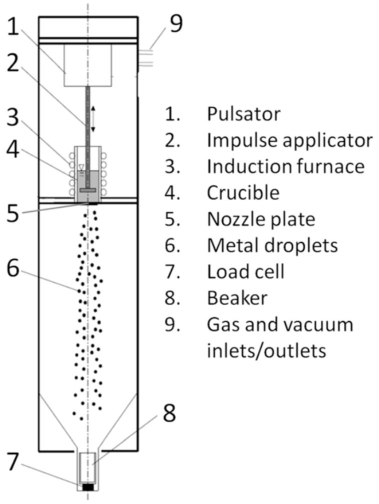

Figure 3.1: Impulse atomization tower schematic [48]

As described in Valloton et al [48], a vibratory plunger was impacted upon a superheated melt pool to force liquid metal through a specifically chosen orifice size. The resulting fluid jets broke up due to Raleigh instability and resulted in droplets. The fluid droplets solidified while falling through the inert atmosphere and were collected in an oil bath at the bottom of the tower.

The parameters of the IA run can be seen in Table 3.1, where the atomization temperature was chosen as a 200 - 300 °C superheat based on the liquidus of the alloy found using Thermocalc 2020a simulation using the TCFE10 database.

Table 3.1: Conditions for Impulse Atomization

Atmosphere	**Oxygen Level (ppm)**	**Atomization Temperature (°C)**	**Orifice Size (μm)**	**Number of Orifices**
He	0.01	1650 - 1750	100	37

The composition of the 17-4PH sample used to generate the IA powders can be found in Table 3.2.

Table 3.2: Powder consumable compositions

Element	**Composition (wt%)**
C	0.01
Mn	0.2
Si	0.3
P	0.007
S	n.d.
Cu	4.3
Ni	4.1
Cr	16.4
Mo	0.01
N	0.02
Nb	0.3
Fe	Bal.

3.1.1 Powder Cleaning and Separation

After atomization, the collected powders were drained of extra oil. To completely remove oil residue the powders were manually agitated with toluene. The toluene was completely replaced and the manual agitation repeated in cycles until the powders and the rinse toluene were visibly free of oil. To ensure full cleaning, two to three more toluene rinses were performed after the rinse liquid appeared oil-free. To complete the cleaning of the powders, an ethanol rinse was performed in a similar manner to remove the toluene. When fully cleaned, the powders were left to air dry.

The solidification of droplets in IA is strictly connected to the size of the powders. The smaller the powder particle, the greater the surface area to volume ratio, and as a result, the faster the cooling rate. This relationship means that to obtain reliable information on the effect of cooling rate on the solidification, careful separation of the powder sizes must be achieved. The powders were separated using a RO-TAP Sieve Shaker and sieve sizes from 1.18mm-125 μm.

3.1.2 Powder Liquid Cooling Rates

IA is a containerless solidification method with very controllable parameters. This closely controlled nature, combined with previous work to define the heat transfer properties of the process means that accurate modelling of the cooling rate of different sizes of powders can be done [49], [50]. A model created for IA powders was applied only to the temperature range where the droplets were liquid and therefore was used to calculate the cooling rate as the droplets cooled from the superheat temperature to the liquidus as they fell.

In the semi-empirical model, the Nusselt number (Nu) is averaged over the droplet surface using the Whitaker correlation equation shown in Equation (3.1) and used to estimate the effective heat transfer coefficient h_{eff}.

$$\begin{aligned} Nu = \frac{h_{eff}D}{k_s} = 2 \cdot \frac{B}{k_s(m+1)} \cdot \frac{(T_s^{m+1} - T_\infty^{m+1})}{(T_s - T_\infty)} + \\ (0.4Re^{1/2} + 0.06Re^{2/3})Pr^{0.4}\left(\frac{\mu_\infty}{\mu_s}\right)^{1/4} \end{aligned} \tag{3.1}$$

where D is the diameter of the droplet, k_s is the gas conductivity at the droplet surface temperature, B and m are the pre-power and power coefficients from the variation of the gas conductivity with temperature, T_s is the temperature at the surface of the droplet, T_∞ is the temperature of the free stream gas, Re is the Reynolds number, Pr is the Prandlt number, and $\frac{\mu_\infty}{\mu_s}$ is the ratio of the viscosity of the shielding gas at the free stream temperature and the temperature at the surface of the droplet.

An assumption is made that there are no temperature gradients within the metal droplets. This assumption is confirmed when the Biot number is less than 0.1. Following this assumption, the general heat transfer equation for the cooling of the droplets is shown in Equation (3.2).

$$\frac{dT_m}{dt} = -\frac{6h_{eff}}{\rho_m Cp_m D}(T_m - T_\infty) \tag{3.2}$$

where $\frac{dT_m}{dt}$ is the change in droplet temperature with time, ρ_m is the density of the liquid metal, and Cp_m is the specific heat capacity of the liquid metal.

To understand the acceleration of the droplets as they fall through the atomization chamber, the initial velocity of the droplet as it exits the plate orifice is assumed to be 0.5 m/s [49] and the instantaneous droplet acceleration is calculated using Equation (3.3).

$$\frac{dv}{dt} = \frac{(\rho_m - \rho_g)}{\rho_m}g - 0.75\frac{\rho_g}{\rho_m}\frac{C_d}{D}v^2 \tag{3.3}$$

where v is the velocity of the falling droplet, ρ_g is the density of the gas, g is the acceleration due to gravity and is considered to be 9.81 m/s^2, C_d is the drag coefficient. The drag coefficient can be calculated using Equation (3.4).

$$C_d = \frac{18.5}{Re^{0.6}} \tag{3.4}$$

A Fourth Order Runge-Kutta method was used to solve Equation (3.2) and Equation (3.3) was solved using a simple Euler method.

Finally, based on further work done by Valloton et. al. to refine the liquid cooling model, the size of the droplet has been found to change how much heat the droplets transfer to their environment and how much the properties of the gas change surrounding the particles [51]. As a result, for particles 400 μm or smaller, the effect on the gas properties is considered to be negligible and the gas properties are taken at T_∞. For power particles with diameters greater than 400 μm, the gas properties are taken at the film temperature, where T_{film} is calculated based on Equation (3.5).

$$T_{film} = \frac{T_s + T_\infty}{2} \tag{3.5}$$

3.2 Additive Manufacturing

All weld bead samples were fabricated using the WAAM system shown in Figure 3.2. The WAAM system consisted of a Fronius Transpuls Synergic 5000 CMT welding power supply, a VR 7000 CMT wire feeder, and a Fronius Robcata welding torch. The torch system was mounted on a custom-built three-axis robotic gantry. Instead of using the Fronius welding control pendant, control of the welding and the movement of the torch was combined through one computer using Robotic Operating System (ROS) controls. To monitor the temperature of weld beads and obtain experimental cooling rates, an Optris two-colour pyrometer, model number CTRF2MH1SFVFC3, was set up 40 cm from the substrate plate. The focusing optics of the pyrometer meant that this measurement distance resulted in a measurement area of 4 mm, a spot size fine enough to ensure only the weld bead was being measured [52].

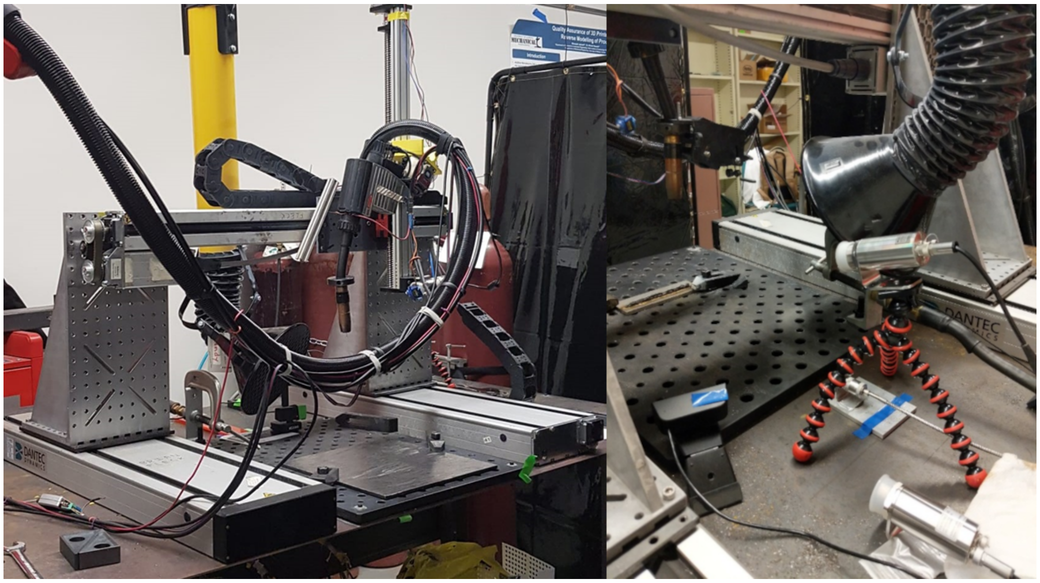

Figure 3.2: WAAM system set up including torch and gantry (left) and pyrometer positioning (right)

In order to ensure the pyrometer was measuring the cooling rate of the steady-state bead and to minimize the measurement of the welding substrate, the pyrometer was focused on an area just above the surface of the plate at the centerline of the bead. The location of the pyrometer measurement area is represented as a green circle in Figure 3.3.

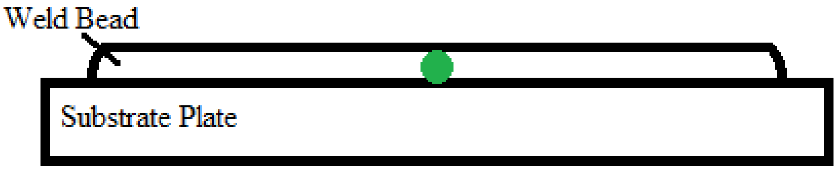

Figure 3.3: Schematic of pyrometer measurement area

Each AM sample was printed using ER630 (17-4PH) 1.2 mm welding wire on 6 x 51 x 152 mm 17-4PH substrate plates using argon shielding gas. The composition of the base plate and welding wire material can be found in Table 3.3.

Table 3.3: Welding consumable compositions

Element	Wire	Plate
C	0.012	0.04
Mn	0.44	0.61
Si	0.41	0.2
P	0.022	0.025
S	0.001	0.001
Cu	3.33	3.28
Ni	4.57	4.78
Cr	16.11	15.5
Mo	0.04	0.22
N	0.03	0.024
Nb+Ta	0.23	0.28*
Fe	Bal.	Bal.

* Nb = 0.27 Ta = 0.01

Figure 3.4 shows an example of a completed sample plate. Each plate consisted of two 101 mm single-pass beads, one bead printed onto a room temperature substrate plate called the cold bead, and one printed directly after the first onto the plate that had been preheated by the initial welding pass, called the warm bead. The centerlines of the two beads were 25 mm apart (the torch moved 25 mm in the y-axis before printing the second bead) regardless of welding parameters. Before welding, plates were prepared by polishing with stainless steel polishing pads on an angle grinder until all mill scale was removed.

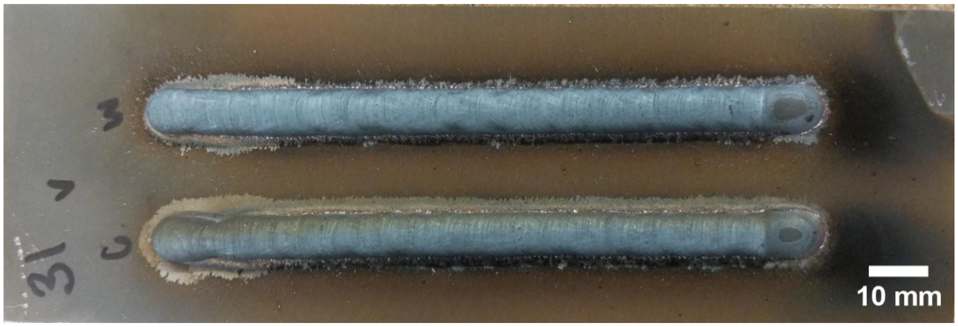

Figure 3.4: Completed sample plate with warm (top) and cold (bottom) bead

3.3 Welding Parameters and Beads

The available literature for 17-4PH in plasma-based AM was very limited, as a result parameter sets were not available to set the basis for testing. In the CMT process, a synergic line must be used. This synergic line is a programmed relationship between the various welding parameters that has been designed based on historical welding data to give the optimum deposition for a user-set wire feed speed (WFS). There is no available 17-4 PH synergic line for the Fronius CMT system used in this work. Based on recommendations from the manufacturer, the ER70S-6Ar-18CO_2 synergic line, a database created for a mild steel deposited under an 18% CO_2 environment, was used as the synergic line for all experiments. The optimized parameters for this steel formed the basis for the initial parameter set tested. The baseline parameters used for 17-4PH can be seen in Table 3.4.

Table 3.4: Initial WAAM Parameters

Property	**Value**
Gas Flow Rate	0.99 $\frac{m^3}{h}$
Torch Travel Speed	5.9 $\frac{mm}{s}$
Wire Feed Speed	29.6 $\frac{mm}{s}$

The parameters used for a mild steel proved to be inadequate for a 17-4PH deposition. As seen in Figure 3.5, the deposition using these parameters was a series of disjointed balls. The heat input was too low, not enabling the steel to overcome the surface tension of the liquid and form a continuous bead.

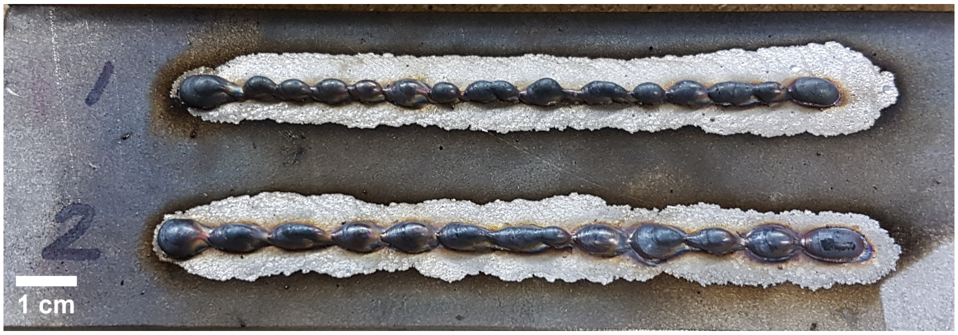

Figure 3.5: Balled weld deposit

After multiple trials, a stable parameter set was established. The purpose of this work was not to develop a range of optimized parameters, but instead to observe the initial solidification of 17-4PH stainless steel over a range of heat inputs that formed a stable weld. In the name of that goal, a stable weld was considered to be one that formed a continuous bead with reasonably uniform dimensions and a somewhat level surface in the central, measurement area. The final range of parameters and their resulting heat input values can be seen in Table 3.5.

Table 3.5: Stable Weld Zone Parameters

Property	**Value**
Torch Travel Speed	4.1 - 2.5 $\frac{mm}{s}$
Wire Feed Speed	38.5 - 76.2 $\frac{mm}{s}$
Current	80 - 130 A
Voltage	12 - 14 V
Heat Input	200 - 645 $\frac{J}{mm}$

The bead profiles of the highest and lowest heat input plates can be seen in Figure 3.6.

Both the highest and the lowest heat input samples are on the limit of the printable range. At the highs and lows of the tested heat inputs, the samples began to see the occurrence of some local waviness and the welds became slightly ropey. Increasing or decreasing the wire feed speed from this

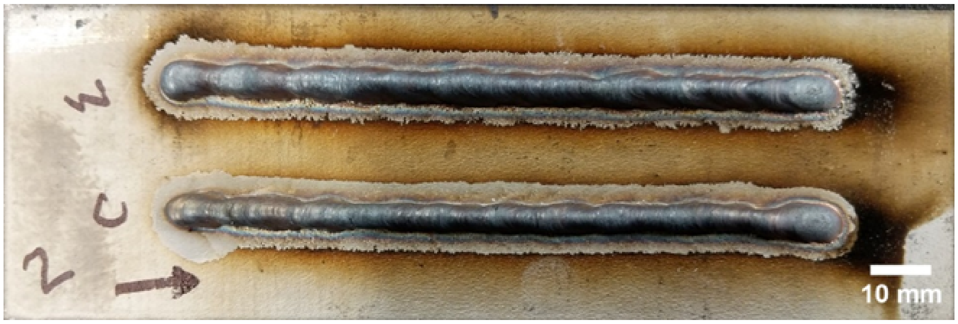

(a) 204 $\frac{J}{mm}$ Sample Beads

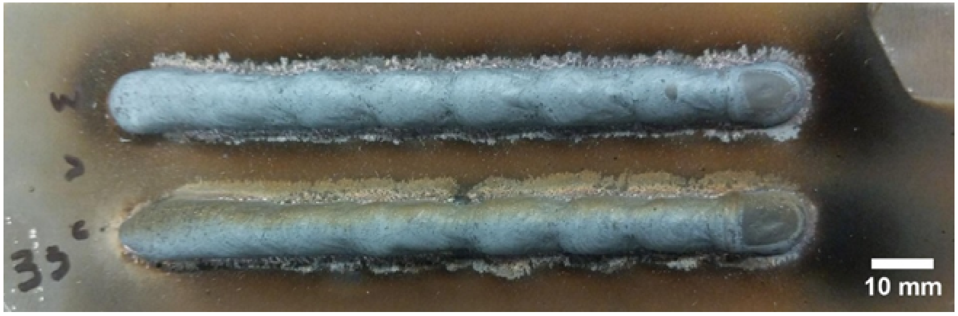

(b) 644 $\frac{J}{mm}$ Sample Beads

Figure 3.6: Bead profile of lowest and highest heat input samples

point would result in balling at the low heat input range and porosity and instability at the high heat input range.

3.4 Sample Preparation and Analysis

For metallographic analysis, the samples were prepared using the following methods.

3.4.1 Cutting, Grinding and Polishing

For AM samples, the section of weld bead that was measured by the pyrometer (indicated in Figure 3.3) was cut out from the bulk of the sample using a Magnum Industrial M1-93200 horizontal bandsaw. As shown in Figure 3.7, the resulting 12.7 - 25.4 mm subsection of the bead was then cut along the centerline using an IsoMet 4000 linear precision saw to allow visualization of the weld bead parallel to the welding direction.

Samples were also prepared perpendicular to the weld direction in order to

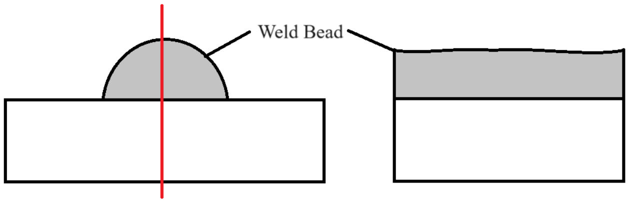

Figure 3.7: Schematic of parallel bead samples; precision saw cut (left) and resulting sample (right)

visualize bead size and shape. The samples were sectioned from either side of the pyrometer measurement area using the horizontal bandsaw.

Both the cut weld bead samples and the sieved powders were cold mounted in an epoxy resin with a Ni powder addition for conductivity. The weld samples were placed in the molds precision saw cut side down to visualize the weld and the IA powder samples were spread in a single layer on the bottom of the mold before epoxy was added. All samples were ground and polished using a Buehler EcoMet 250 Automatic Grinder-Polisher. The first grinding step, using 240 grit paper, was conducted until the centerline of the weld samples was reached or until the powder particles' edges were touching to try to ensure the central bulk of each powder particle was analyzed. After samples were planed to an appropriate depth, weld samples were ground with 320, 600, and 800 grit papers and polished with 9, 3, 1, and 0.05 μm polishing solutions. After planing, powder samples were only ground with 800 grit paper to increase powder retention and lower the risk of the polishing through fine samples. Polishing of powder samples followed the same method as bulk weld samples.

3.4.2 Etching

Three different etchants were used over the course of this work. Etchant compositions, times, and methodology can be found in Table 3.6. For more information on etching, a full description of etchants and results can be found in Appendix A.

While trials were also done with Le Pera's reagent, no positive results were observed so it is not included in this work.

Table 3.6: Etchant Compositions and Methodology

Etchant	**Composition [53]**	**Methodology**
Kalling's	$1.5g\ CuCl_2 + 11ml\ H_2O + 11ml\ HCl + 11ml$ ethanol	Immersion for 10 - 12 seconds followed by water and ethanol rinse
Vilella's	$100ml$ 1% picric acid in ethanol + $5ml\ HCl$ + $1-2$ drops H_2O_2	Immersion for 6 - 12 minutes followed by ethanol rinse
Fry's	$30ml\ H_2O + 40ml\ HCl + 25ml$ ethanol + $5g\ CuCl_2$	Immersion for 10 - 15 seconds followed by water and ethanol rinse; samples must be freshly polished

3.4.3 Microscopy

A combination of microscopic and spectroscopic techniques were used to fully analyze the macro- and microstructures of all samples. Optical microscopy was done using a Olympus BX61 optical microscope and lenses from 2.5X to 100X magnification. Scanning electron microscopy (SEM) was done using a Tescan Vega3 SEM equipped with a tungsten filament and an Oxford Energy-dispersive X-ray Spectroscope (EDX) detector. SEM images were taken with an accelerating voltage of 20kV and the secondary electron (SE) detector.

For more detailed imaging of sample grains and phases, Electron Backscatter Diffraction (EBSD) was performed using a Sigma Field Effect SEM (FE-SEM) equipped with an Oxford EBSD detector.

3.4.4 Differential Scanning Calorimetry

Differential Scanning Calorimetry (DSC) was performed on welding wire samples to observe transformation temperatures and microstructure of samples with slower, controlled cooling rates. All DSC was done with a Linseis DSC PT 1600, a high-temperature DSC to allow for full melting of the alloy. An additional 17-4 PH sample bar was also tested in the DSC to observe the effect of altering the Cr_{eq}/Ni_{eq} on microstructure at slow cooling rates. The composition of the other samples tested can be seen in Table 3.7

Table 3.7: DSC sample bar consumable composition

Element	**Composition (wt%)**
C	0.03
Mn	0.83
Si	0.41
P	0.0023
S	0.022
Cu	3.68
Ni	4.22
Cr	15.22
Mo	0.19
N	0.031
Nb	0.26
Fe	Bal.

3.4.5 Secondary Dendrite Arm Spacing

Secondary dendrite arm spacing (SDAS) was measured for all powder sizes with dendritic features. The secondary dendrite arm spacings were taken according to the linear intercept method described in ASTM E112 [54]. The specific methodology used was based on the recommendations by Vandersluis et. al. [55]. An example of SDAS measurements can be seen in Figure 3.8.

The length of each measurement line was recorded along with the number of secondary dendrite arms it passed through. The SDAS was then calculated according to Equation 3.6.

$$\lambda_2 = \frac{L}{N-1} \tag{3.6}$$

where λ_2 is the SDAS, L is the length of the line drawn on the sample, and N is the number of secondary dendrite arms that intersected the line.

SDAS have a well-known relationship with cooling rate that can be described by Equation (3.7) [56].

$$\lambda_2 = B\dot{T}^{-n} \tag{3.7}$$

where B and n are material dependent constants and $\dot{T}$ is the cooling rate.

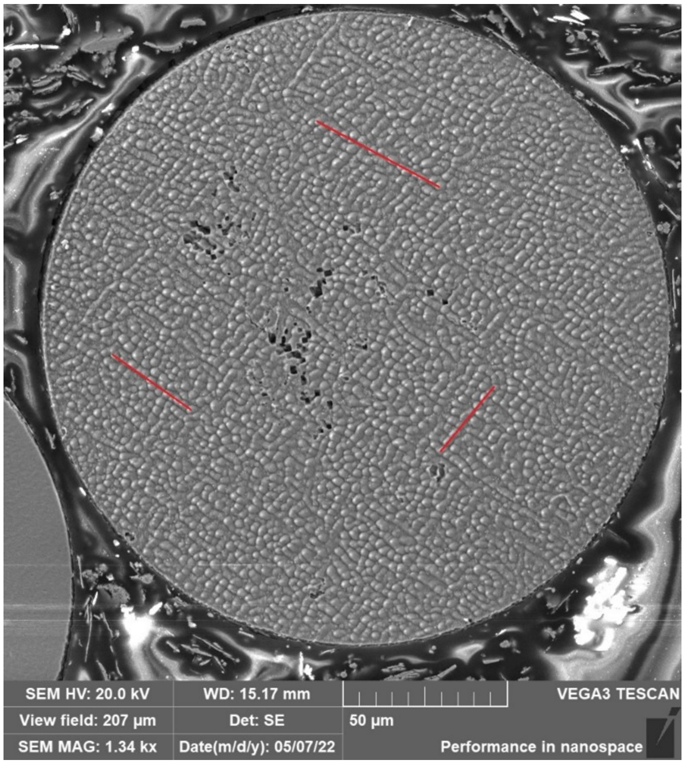

Figure 3.8: Example SDAS measurements on a 17-4PH IA powder particle

3.4.6 Velocity of Solidification

Velocity of solidification was calculated for each weld bead. The velocity of the solidification front through the bead was calculated by measuring the angle of columnar growth along the centerline of the bead. The measured θ was then used to calculate the velocity of solidification using the trigonometric relationship described in Equation 3.8.

$$v_s = TTS \cdot cos(\theta) \tag{3.8}$$

where TTS is the torch travel speed and θ is the angle of columnar growth [57].

Chapter 4

Microstructure

Microstructural phases were identified and characterized for all sample fabrication methods studied in this work. The results are presented in this chapter.

4.1 Scheil-Gulliver Solidification Modelling

To predict the phases that will form on solidification, a Scheil-Gulliver (SG) simulation was run using Thermo-Calc 2020a and the TCFE10 database (Figure 4.1).

The first phase to solidify is the body-centered cubic (BCC) phase, δ-ferrite. The next stage of solidification is a BCC and face-centered cubic (FCC) region where FCC austenite begins to form from the previously solidified δ-ferrite. The final solidification phase involves the formation of Z-phase, which in stainless steels is a complex, NbCrN nitride [58]. Thermo-Calc predicts this nitride will consist of less than 0.005 mole fraction of the phases present after solidification, so Z-phase was not considered as a major phase constituent.

4.2 Impulse Atomized Powders

IA powder samples, prepared according to the method described in 3.1, were imaged using SEM to observe the microstructure. Two main morphologies were found to dominate in the rapidly solidified 17-4PH particles: dendrites and martensitic lathes or needles. At the smallest particle sizes, which correspond with the fastest cooling rates, the dendritic microstructure was the

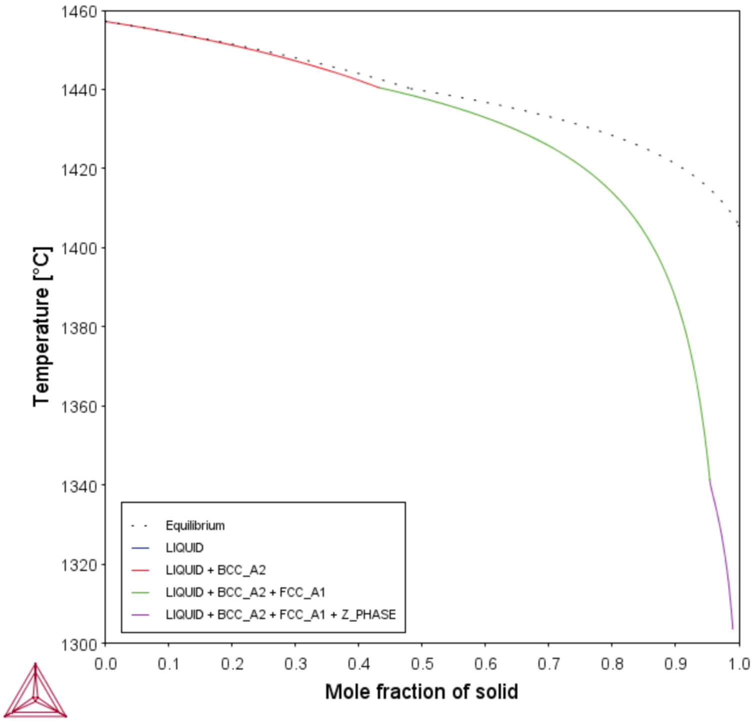

Figure 4.1: Scheil-Gulliver solidification simulation

major microstructural phase. The typical microstructure of a 150 - 180 μm size particle can be seen in Figure 4.2.

As the particle size increased and the cooling rates decreased, it became more common to see particles that were largely dendritic but contained small sections of martensite. In Figure 4.3, a 300 - 250 μm size range particle can be seen that consists of a majority of dendritic microstructure but with a small martensitic section on the left side of the particle.

Within a selection of particles in the 300 - 250 μm size range, particles with different amounts of martensite were seen (Figure 4.4), showing the variability of martensite formation even among particles with the same thermal history.

While martensitic particles formed at every size range, as the size increased the fully martensitic particles began to present as the most common microstructure. Above 700 μm, there were no longer any fully dendritic particles. All particles in the largest two size ranges were at least partly martensitic. The microstructure of the 1.18 mm - 850 μm size particles can be seen in Figure 4.5.

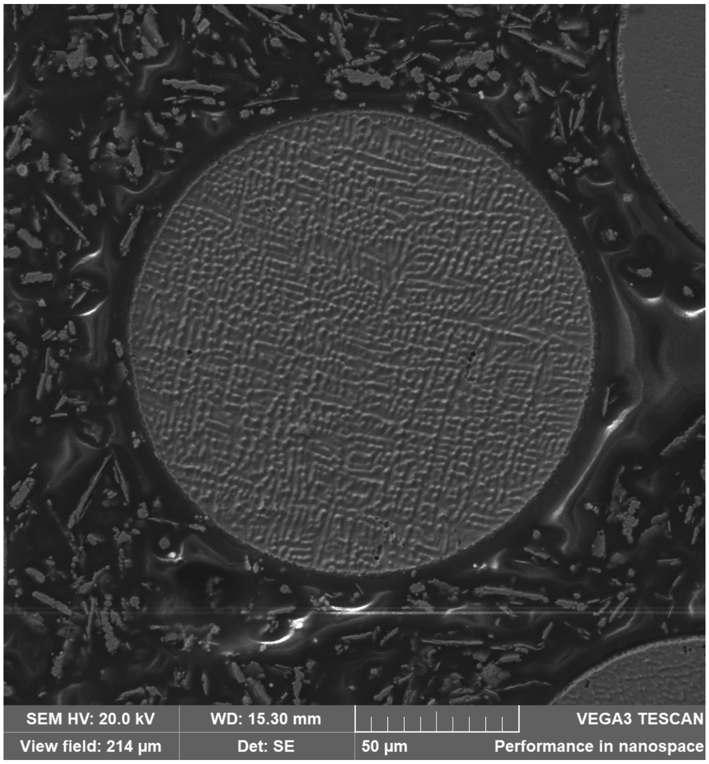

Figure 4.2: Dendritic microstructure in 180 - 150 μm powder size range

Microstructures observed at more powder sizes can be seen in Appendix B.

4.2.1 Electron Backscatter Diffraction

To analyse the phases in greater detail, electron backscatter diffraction (EBSD) was conducted on 1.18 mm - 850 μm, 500 - 425 μm, and 300 - 250 μm powder size ranges.

In the largest powder size range, the central area of shrinkage porosity was examined, as well as the solid bulk of the powder. In Figure 4.6, a solid section of a 1.18 mm - 850 μm size powder particle was imaged. The entire range measured was indexed as BCC, indicating that the phase(s) present was either δ-ferrite and/or martensite [37], [39]. Based on the grains shown in 4.6b, it is likely that this section of the powder is largely martensitic.

Another 1.18 mm - 850 μm powder particle was imaged around the central shrinkage porosity that was common to many of the IA powders in this study. The shrinkage revealed a dendritic structure, making this portion of

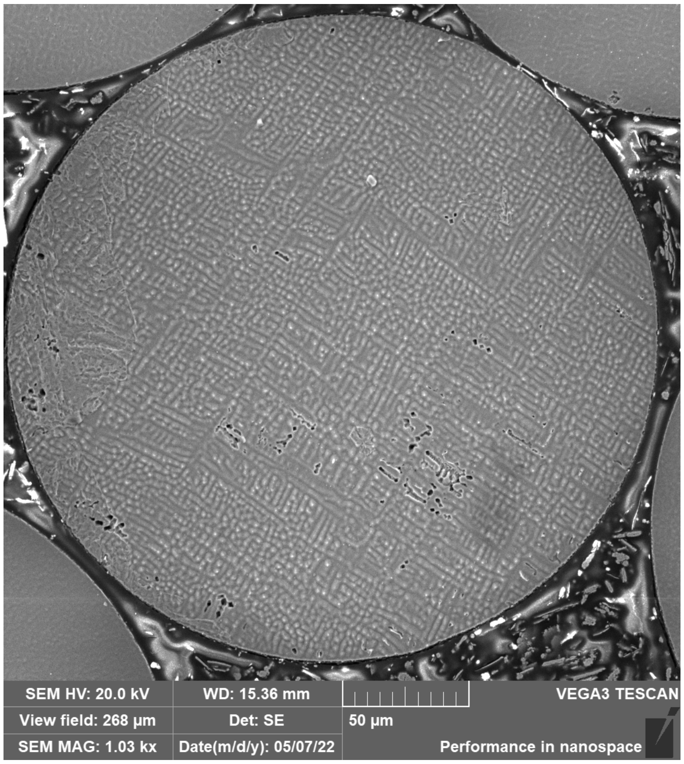

Figure 4.3: Dendritic microstructure with martensitic section in 300 - 250 μm Particle

the particle especially interesting for phase identification. Figure 4.7 shows the phase and grain maps of the measured area. In 4.7a, it can be seen that the majority of the indexed pixels are δ-ferrite or martensite. All white pixels represent non-indexed phases, the bulk of which are located in the right of the image where the porosity was in the particle. There are a few pixels that were indexed as austenite (FCC) in this image, however these austenite pixels do not represent any significant portion of the sample and may be mis-indexing due to surface texture. In Figure 4.7b, the grains around the shrinkage porosity are visible. Based on the morphology of the grains, it can be observed that even in areas where dendritic growth is visible, a full transformation to martensitic lathes has occurred upon cooling.

In the midsize powder range, 500 - 425 μm, both major microstructural phases observed in the optical micrographs were found. The majority of particles observed in this size range had the martensitic lathe morphology shown in Figure 4.8. The EBSD image was taken around the central shrinkage porosity

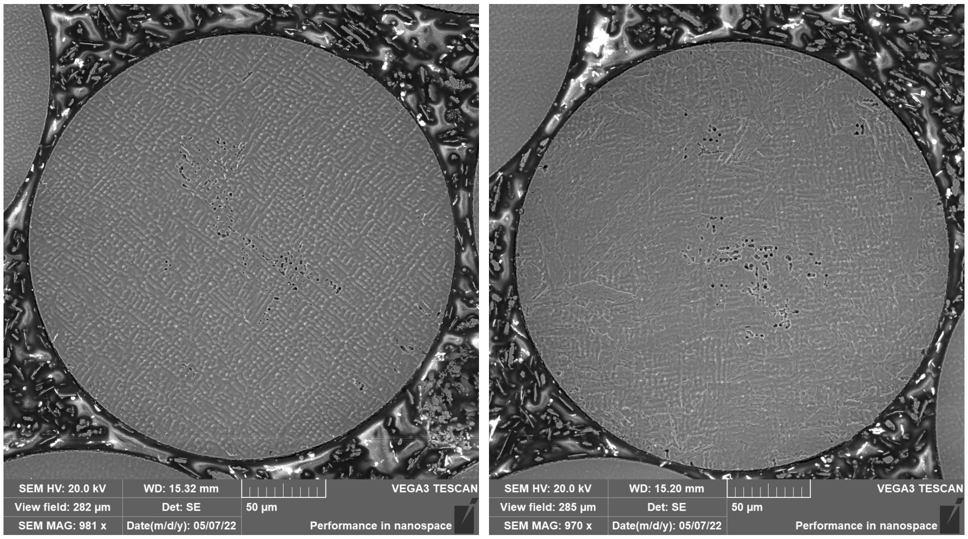

(a) Fully dendritic (b) Partially martensitic

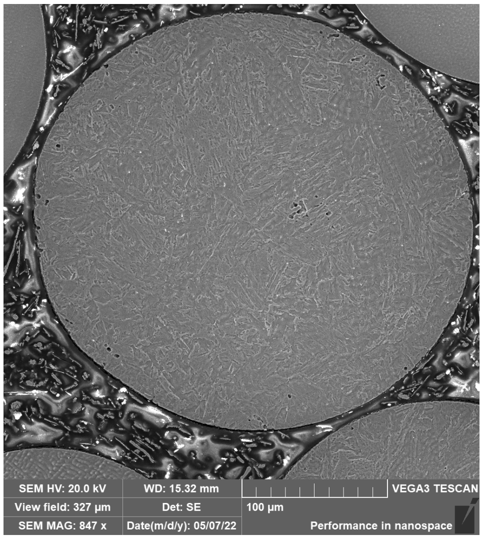

(c) Fully martensitic

Figure 4.4: A range of martensite fractions over the same cooling rate in the 300 - 250 μm size range

of the powder and the characteristic porosity can be seen in the white voids shown in Figure 4.8a.

In addition to the martensitic particles, multiple 500 - 425 μm powders were observed to have a single grain BCC structure. This single grain particle corresponded with the dendritic microstructure seen in the optical micrographs. The presence of a fully dendritic BCC microstructure that is stable at room temperature indicates that the same austenite bypassing seen in works

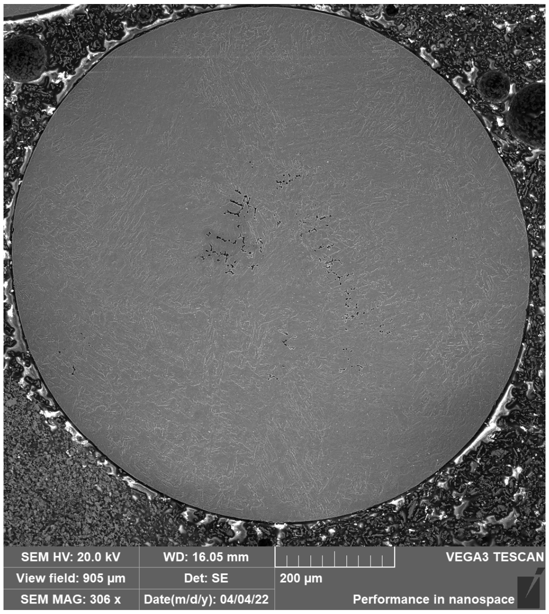

Figure 4.5: A 1.18 mm - 850 μm particle with a martensitic microstructure

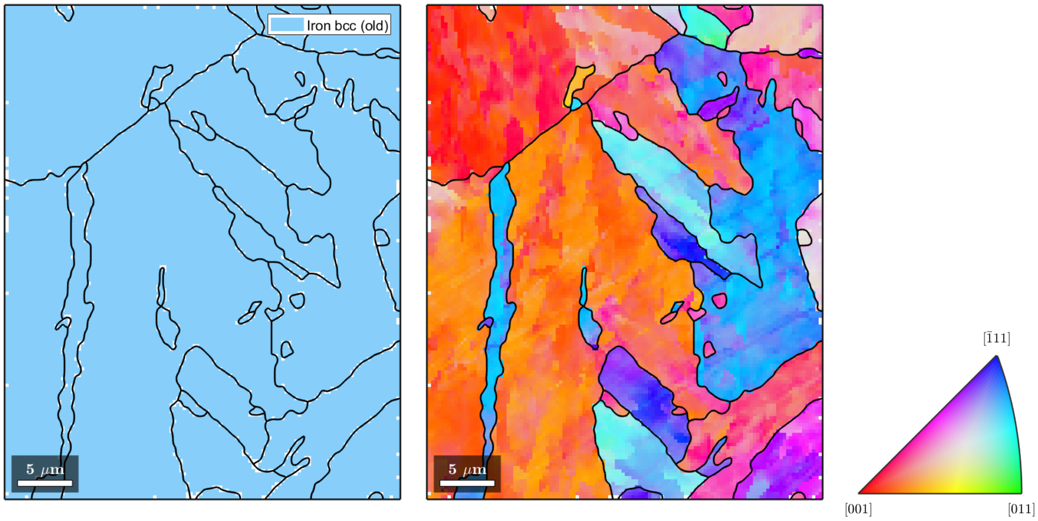

(a) Phase map

(b) Grain orientation

Figure 4.6: 1.18 mm - 850 μm powder bulk EBSD

by Vunnam et. al, Alnajjar et. al., and Sabooni et. al. occurred during the impulse atomization of this 17-4 PH alloy [37], [39], [47].

The same single grain δ-ferrite structure was seen in the smallest powder size analyzed with EBSD (Figure 4.9). In the 300 - 250 μm size range, the majority of the powder particles imaged consisted of a single, BCC grain. However, as observed in the OM images, there were still fully martensitic

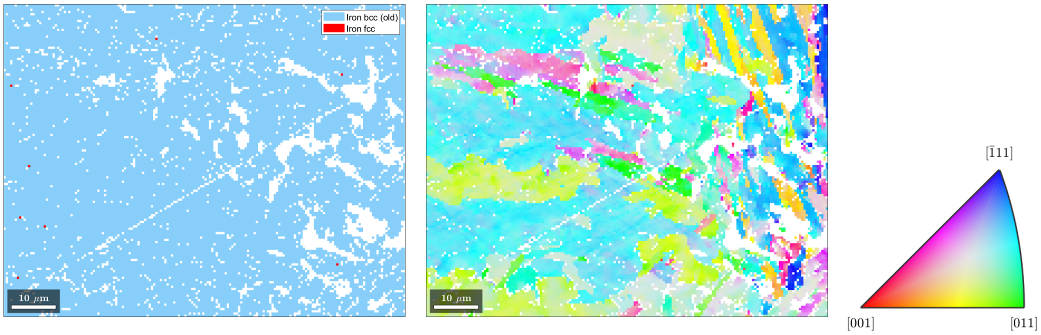

(a) Phase map (b) Grain orientation

Figure 4.7: 1.18 mm - 850 μm powder center EBSD

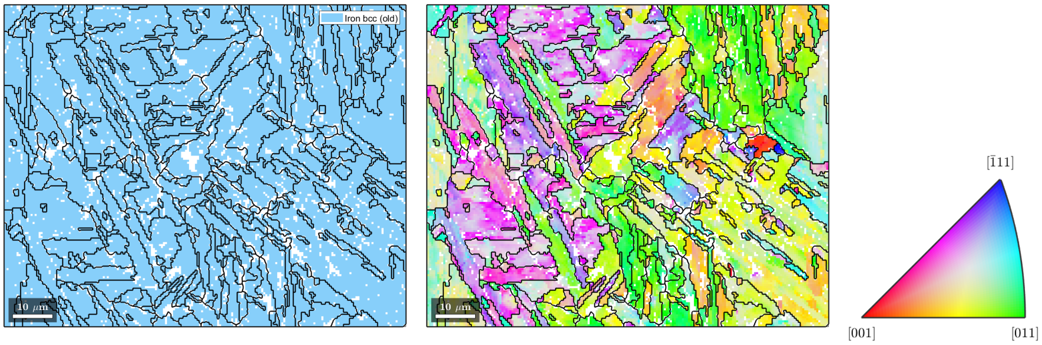

(a) Phases (b) Grain orientation

Figure 4.8: 500 - 425 μm powder center EBSD

particles formed at this cooling rate (Figure 4.9a). Along with fully dendritic and fully martensitic powders, the 300 - 250 μm size range contained particles that were a mix of dendritic and martensitic microstructures (Figure 4.9b). In these powders, the majority of the powder particle was composed of a single large grain of BCC δ-ferrite with a surface nucleation and growth a secondary phase. The secondary phase showed that austenite nucleation and growth occurred that subsequently transformed to martensite on cooling to room temperature. The EBSD data shown illustrates the grain orientations in the powder samples, the phase maps indicated that the samples were entirely BCC.

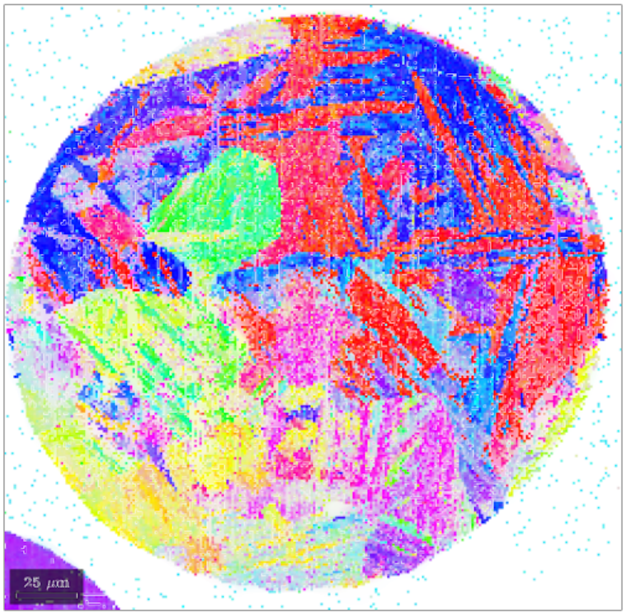

(a) Fully martensitic

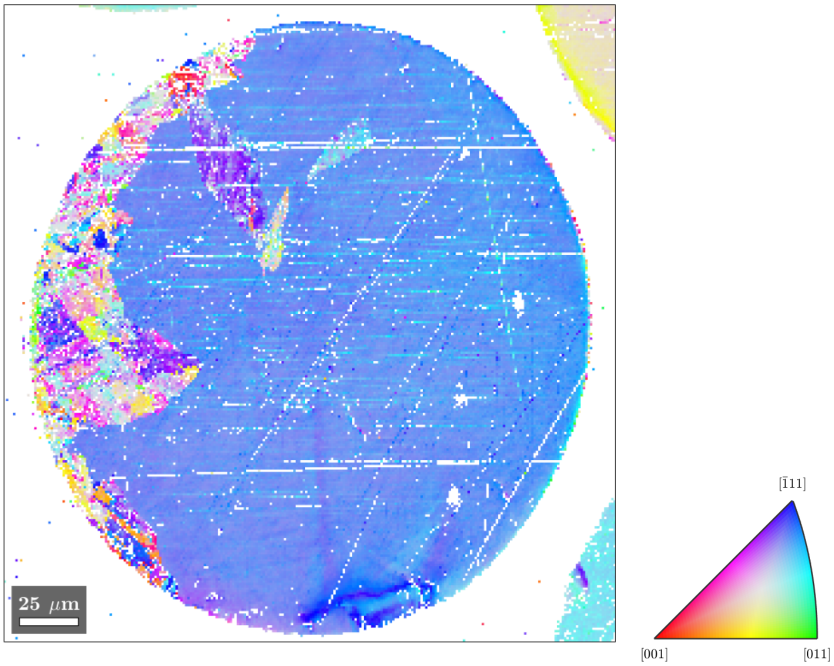

(b) Mixed dendritic and martensitic

Figure 4.9: 300 - 250 μm powder particles

4.3 WAAM

The WAAM microstructure was characterized by several key features; columnar grains through the thickness of the bead, an equiaxed grain structure along the top of the bead, and a mixed martensite and δ-ferrite microstructure. All of these features can be observed at all solidification cooling rates and heat inputs studied.

4.3.1 Optical Microscopy

In Figure 4.10, the major features of a WAAM microstructure bead can be observed. Figure 4.10a shows the equiaxed top region of a WAAM bead. Beads at all heat inputs transitioned from a columnar microstructure (4.10b) that was present through the thickness of the bead to an equiaxed region at the top. In terms of phases present, the WAAM samples appeared to consist of a martensite matrix with untransformed δ-ferrite remaining in intergranular regions. Figure 4.10c shows a typical WAAM microstructure with larger remaining δ-ferrite grains indicated with arrows. This mixed martensite and ferrite structure reflects the predictions of the Schaeffler diagram based on the Cr_{eq}/Ni_{eq} of the welding wire of 3.28 [59].

The effect of heat input on the WAAM microstructure was subtle over the heat inputs and cooling rates studied. The microstructure of the highest and lowest heat input samples can be seen in Figure 4.11. A similar columnar microstructure with a mix of δ-ferrite and martensite can be seen. At a higher magnification, there does appear to be a a change in the scale of the microstructure, but the phases present at all cooling rates remain the same. All samples had the same Cr_{eq}/Ni_{eq} and as indicated by previous research, it would take a wider range of cooling rates before the predictions of the Schaeffler diagram become inaccurate. It is therefore consistent with the findings of David et. al. that the phase constituents were the same at all WAAM cooling rates studied [35].

4.3.2 EBSD

EBSD of the low heat input, high cooling rate sample is shown in Figure 4.12 and of the high heat input, low cooling rate sample in Figure 4.13. The EBSD analysis of the highest and lowest cooling rate samples showed that all samples had a BCC structure. As previously discussed in Section 2.2.3 due

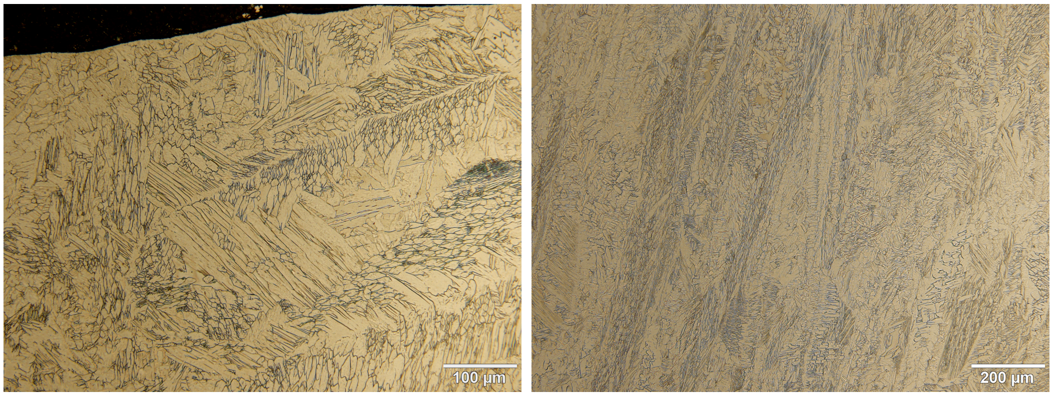

(a) Equiaxed region (b) Columnar region

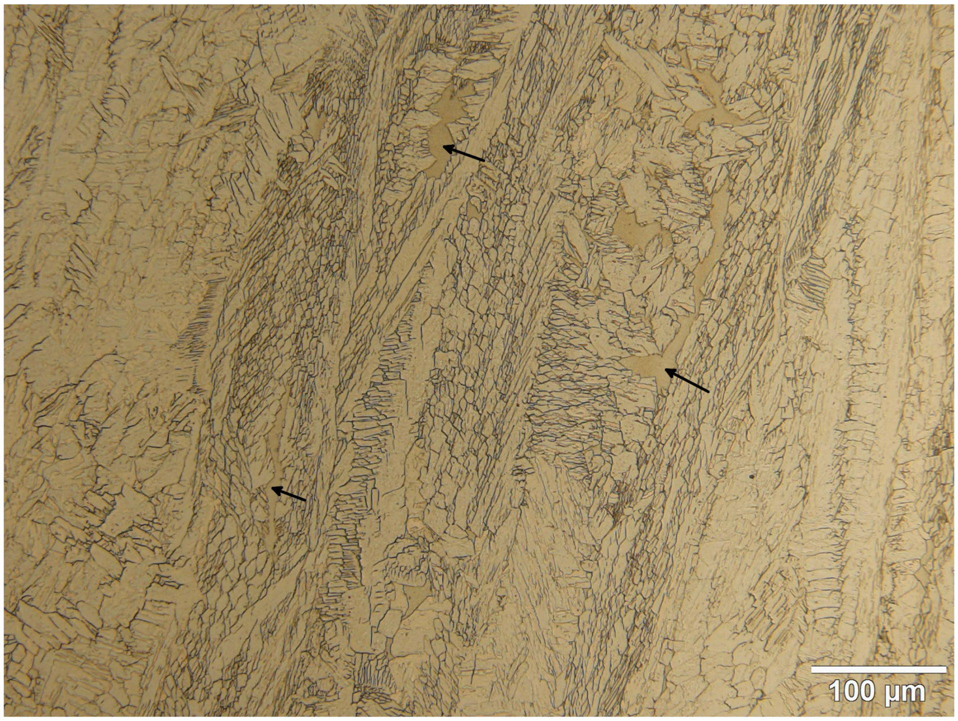

(c) 204 $\frac{J}{mm}$ sample with δ-ferrite marked with arrows

Figure 4.10: Major microstructural features in a WAAM bead

to the low carbon content of the steel, both δ-ferrite and martensite index as BCC in EBSD analysis. The microstructure of the WAAM samples was therefore confirmed to be δ-ferrite and martensite as shown in the optical microscopy images. Grain analysis through EBSD showed that all samples contain a mix of small and large grains corresponding relatively well with the columnar structure that was observed in the OM images. While both samples contain these small and large grains, the average grain size in the high cooling

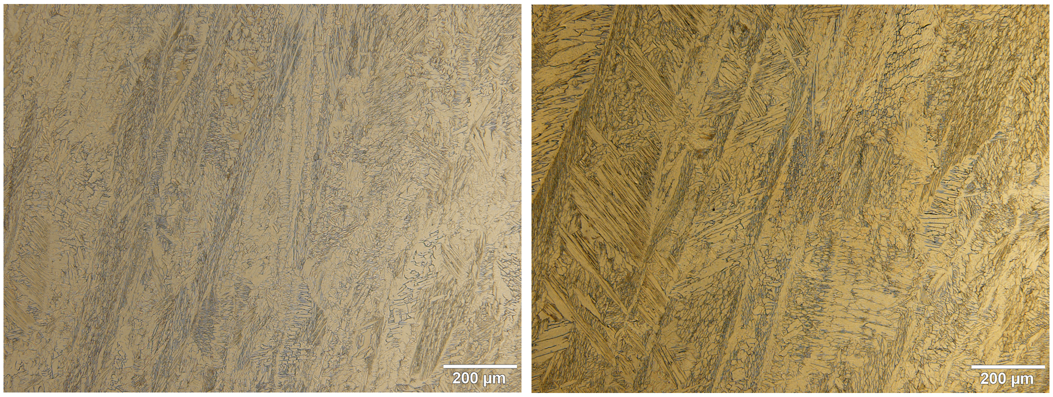

(a) 204 $\frac{J}{mm}$ sample columnar structure (b) Columnar structure in high heat

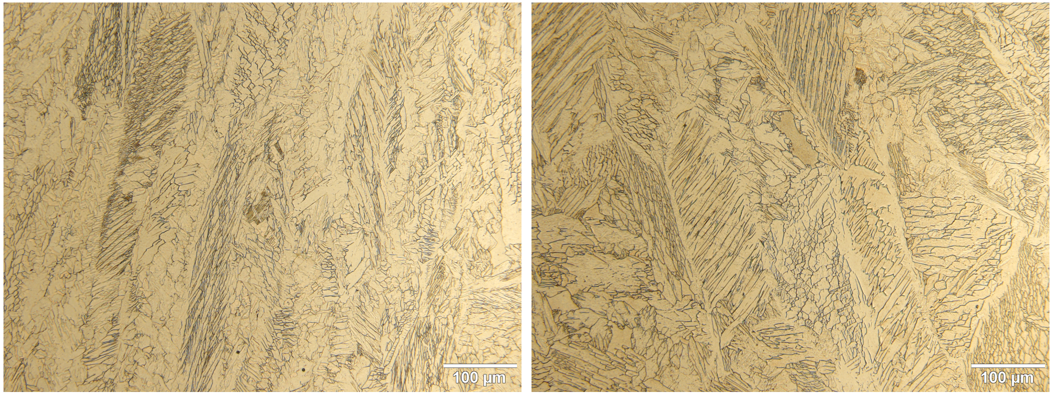

(c) 204 $\frac{J}{mm}$ microstructure (d) 640 $\frac{J}{mm}$ microstructure

Figure 4.11: Major microstructural features in low and high heat input samples

rate sample was 67 μm^2 and the average grain size in the low cooling rate sample was 99 μm^2, indicating a small amount of coarsening with a lower cooling rate. However, more data from the range of heat inputs would be required to confirm the coarsening trend indicated by these values.

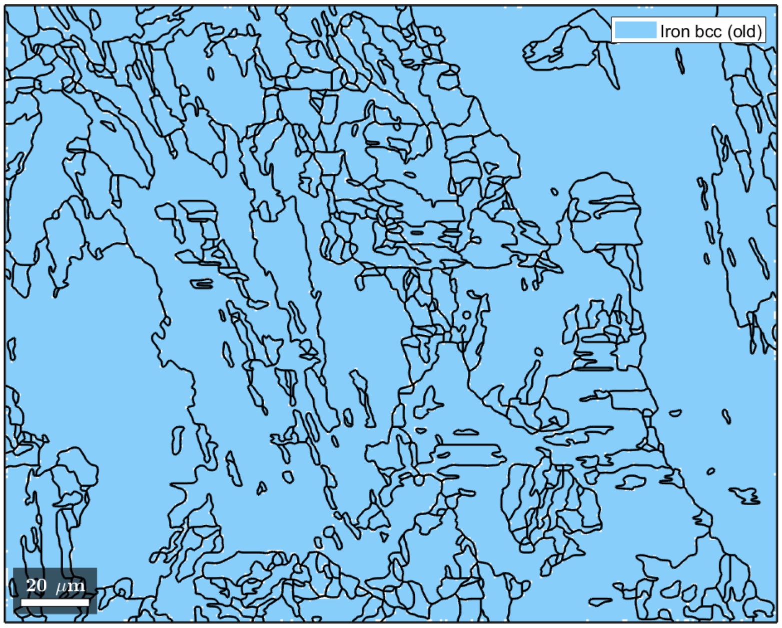

(a) Phase map

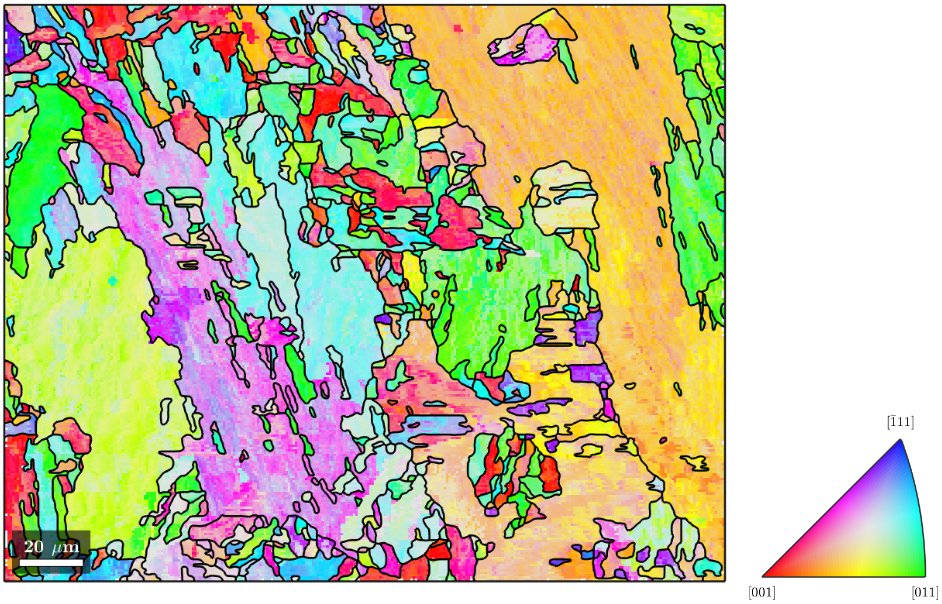

(b) Grain orientation

Figure 4.12: 240 $\frac{J}{mm}$ WAAM sample EBSD

4.4 DSC

Differential scanning calorimetry (DSC) was used to create samples with lower cooling rates and observe the solidified microstructure. Samples were created at cooling rates of 2, 10, and 20 $\frac{°C}{min}$.

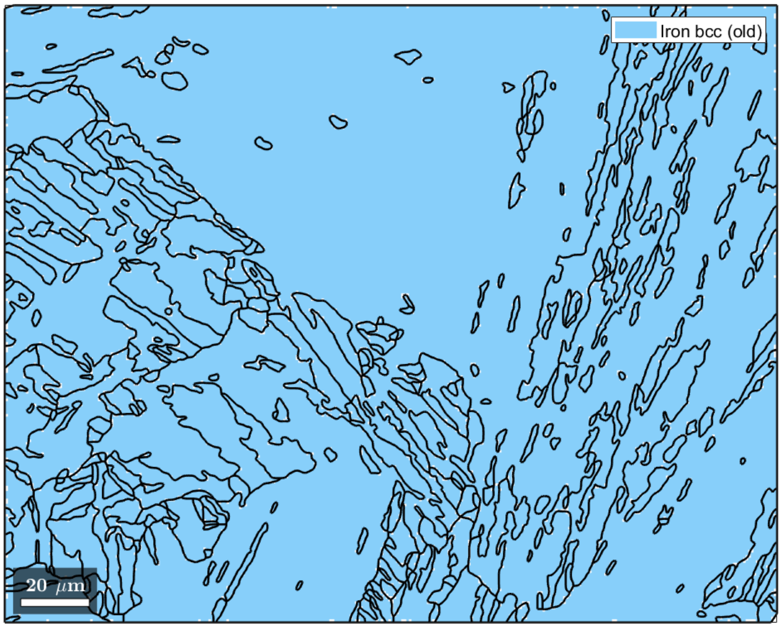

(a) Phase map

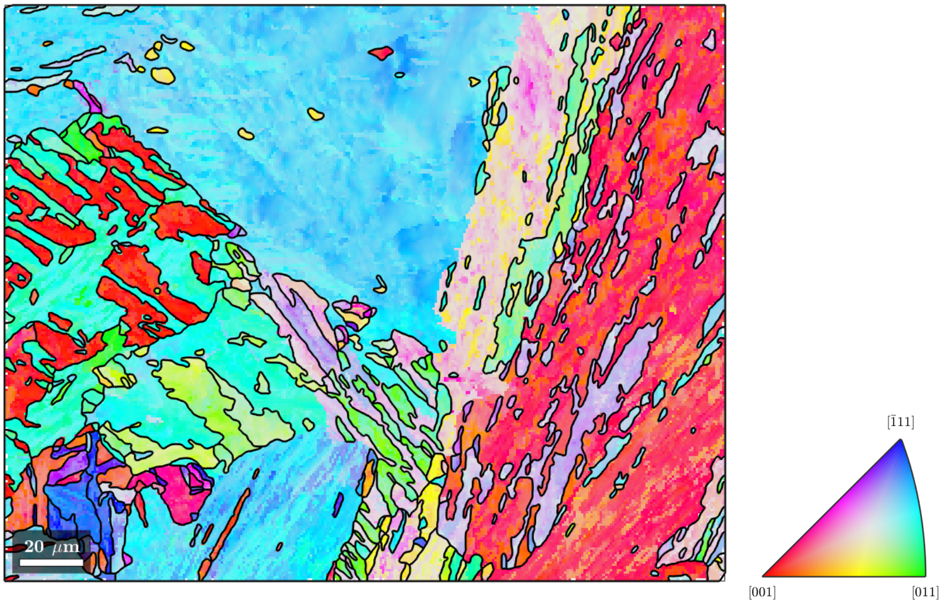

(b) Grain orientation

Figure 4.13: 640 $\frac{J}{mm}$ WAAM sample EBSD

In Figure 4.14, the microstructure of samples created in the DSC from 2 - 4 mm pieces of previously unmelted welding wire can be seen. At each cooling rate, the DSC samples featured the same matrix phase with a second, interdendritic phase. As the cooling rate increases, the scale of the microstructure is refined.

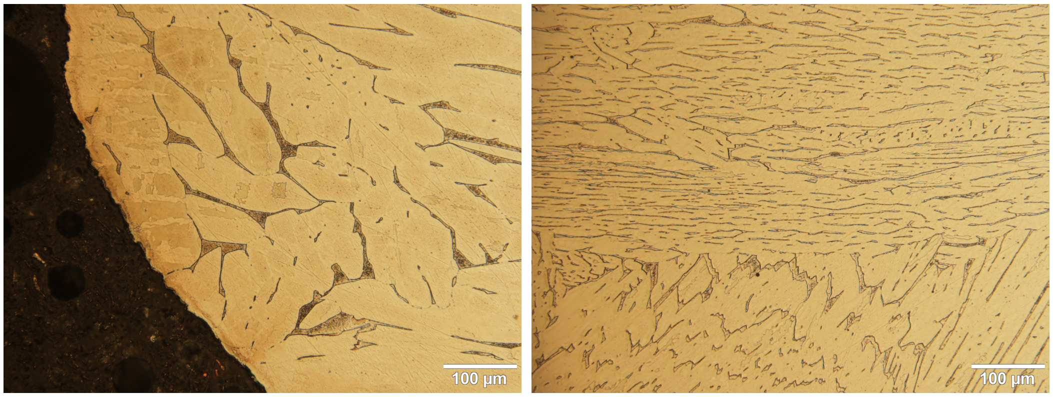

(a) 2 $\frac{^\circ C}{min}$ sample (b) 10 $\frac{^\circ C}{min}$ sample

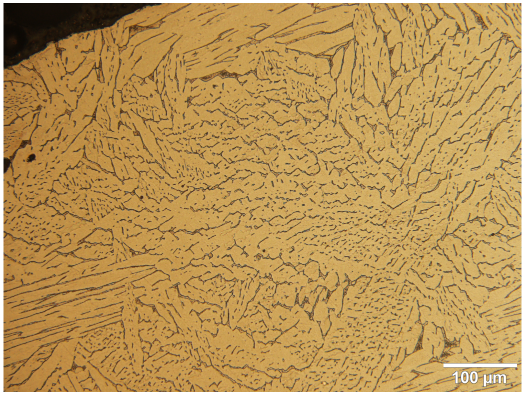

(c) 20 $\frac{^\circ C}{min}$ sample

Figure 4.14: DSC samples from welding wire

To identify the phases present, EBSD was preformed on the 2 $\frac{K}{min}$ wire sample. The results of the EBSD phase map can be seen in Figure 4.15. The DSC wire sample was fully BCC through the thickness of the sample. The fully BCC EBSD results, combined with the duplex structure indicate that the DSC samples consisted of a martensitic matrix with interdendritic δ-ferrite, the same phase makeup seen in the WAAM samples.

For more information on the heat flow during DSC testing, modulated heat flow curves can be found in Appendix D.

More DSC runs were completed on a 17-4 PH sample bar, the composition of which can be seen in 3.4.4. Micrographs of the samples at cooling rates of 2, 10, and 20 $\frac{^\circ C}{min}$ can be seen in Figure 4.16. At every cooling rate studied, this different composition of 17-4 PH solidified with a lower fraction of δ-ferrite. This demonstrates that the composition sensitivity Vunnam et. al.

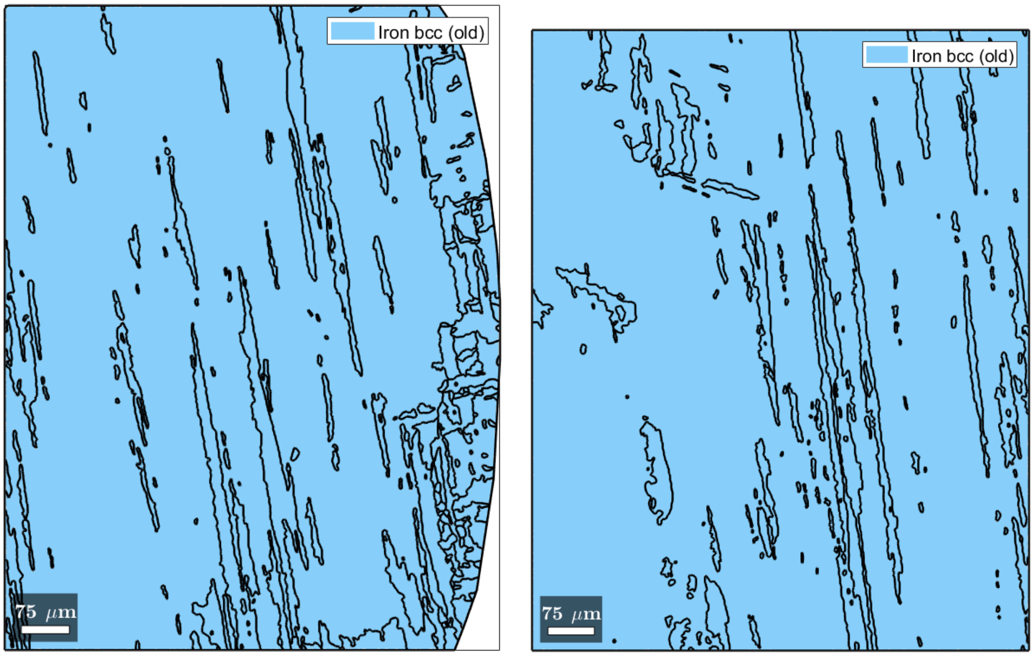

(a) 2 $\frac{K}{min}$ sample (b) 2 $\frac{K}{min}$ sample

Figure 4.15: EBSD of DSC welding wire samples

and Sabooni et. al. witnessed at high cooling rates is present at very slow cooling rates as well [39], [47].

4.5 Summary

IA powders were created over a range of cooling rates. Over the range of cooling rates created, the powders featured a mix of martensitic and dendritic microstructures. At the lowest cooling rates, the powders were entirely martensitic. As the cooling rate increased, a mix of martensitic and dendritic microstructures appeared, with some powder particles showing both martensite and dendrites. At the highest cooling rates studied, the powder was almost entirely dendritic with very few martensitic particles. EBSD analysis showed that all the powder particles were fully BCC as the martensite has a low enough carbon content to index as BCC and the dendritic microstructure was a retained δ-ferrite structure as a result of austenite by-passing at high cooling rates.

In the WAAM samples, the range of heat inputs gave a cooling rate range

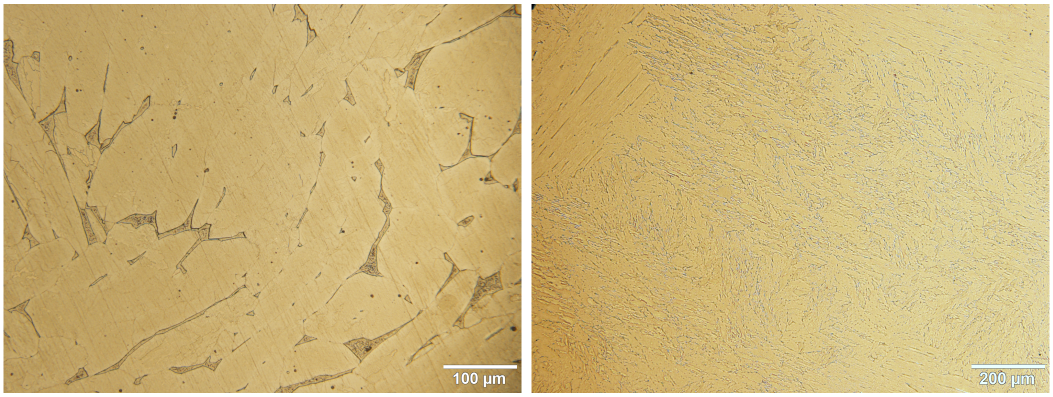

(a) 2 $\frac{K}{min}$ bar sample (b) 10 $\frac{K}{min}$ bar sample

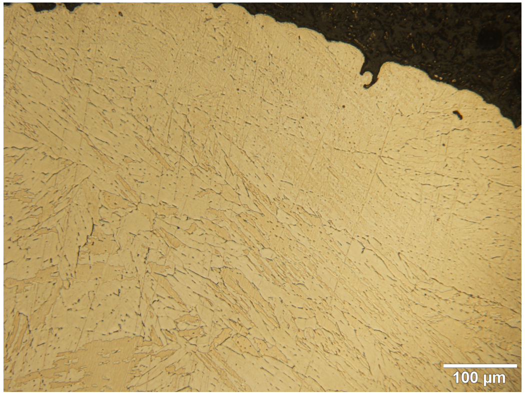

(c) 20 $\frac{K}{min}$ bar sample

Figure 4.16: DSC samples from sample bar

of 486 - 139 $\frac{^{\circ}C}{s}$ Across the entire heat input range, the WAAM beads had a columnar microstructure through the thickness of the bead with an equiaxed region along the top of the bead. EBSD showed the beads were made up of a BCC structure which was a mix of δ-ferrite and martensite. A very small amount of FCC was indexed ($\leq 0.05\%$) indicating there was little to no retained austenite in the samples.

Finally, DSC samples were created at cooling rates of 2 - 20 °C/min. Despite the slow cooling rates, EBSD and OM data showed that the microstructure of the DSC samples was a mixture of martensite and interdendritic δ-ferrite. A different composition of 17-4 PH solidified with a much lower fraction of δ-ferrite, showing that the alloy is sensitive to composition at very low cooling rates as well as very high ones, as had previously been shown.

Chapter 5

Cooling Rates

In order to characterize the effect of the thermal history on all 17-4 PH samples the cooling rates were obtained for both the IA powders and the WAAM samples.

5.1 Powder Cooling Rates

Cooling rates for the average diameter of each powder size range were calculated based on the model described in 3.1.2. In order to use the model, a series of material and gas properties had to be known. The properties of 17-4PH used in the cooling rate calculations can be seen in Table 5.1. More information on how the specific heat of the alloy was determined can be found in Appendix C.

Table 5.1: 17-4PH properties [60], [61]

Property	Value
Start Temperature (K)	1973
Liquidus (K)	1713
Emissivity	0.7
Specific Heat ($\frac{J}{kgK}$)	4060
Density $\frac{kg}{m^3}$	6900

In addition to the properties of the steel, gas properties were used in the heat transfer calculations. All IA in this work took place in a helium gas environment, the properties of which are shown in Table 5.2.

Table 5.2: Helium Gas Properties [62], [63]

Property	**Value**
Density $\frac{kg}{m^3}$	$37.303T^{-0.9559}$
Viscosity $(Pa \cdot s)$	$4.3678T^{0.6702} * 1e-7$
Specific Heat $\frac{J}{kgK}$	5197
Conductivity $\frac{W}{mK}$	$0.2778 * 1e-2 * T^{0.7025}$

The liquid cooling curve for each powder particle size range can be seen in Figure 5.1.

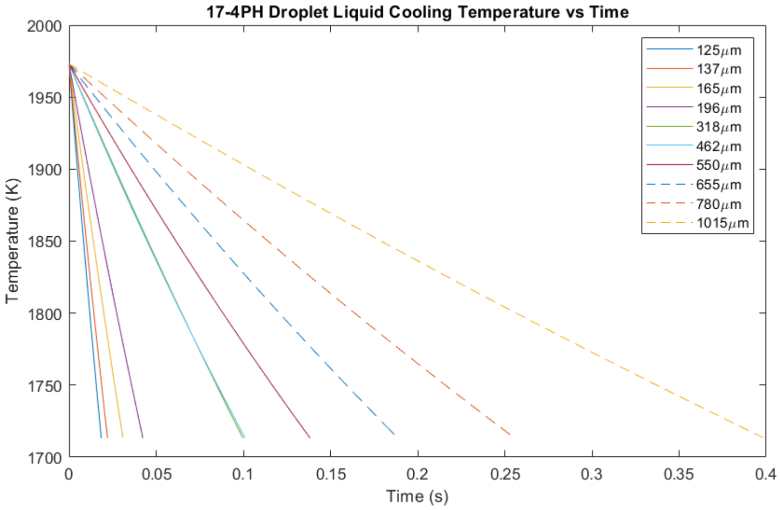

Figure 5.1: Liquid cooling curves for IA powder size ranges

The particle cooling rates varied over the sizes produced by atomization from about 650 K/s for the largest 1000 μm particles to over 14000 K/s for the smallest 125 μm particles.

5.2 WAAM Solidification Cooling Rates

The solidification cooling rates were obtained from pyrometer data. Separate cooling curves were extracted from a data file containing information for both a cold and warm bead. The lower temperature limit of the pyrometer's range was 550 $°C$. Therefore, cooling curves were considered to start when the pyrometer detected the welding arc and end when the sample cooled to 550 $°C$. A sample cooling curve can be seen in Figure 5.2. The curve can be seen to be represented by two major sections. On the far left of the curve, there is a point cloud composed of a large amount of scattered data. This section of scattered data is the signal saturation as the plasma passed through the measurement zone. At approximately 1500 $^{\circ}C$, there is a slight dip and then rebound in the recorded temperature as the saturation passed and the pyrometer began to measure the actual deposited bead.

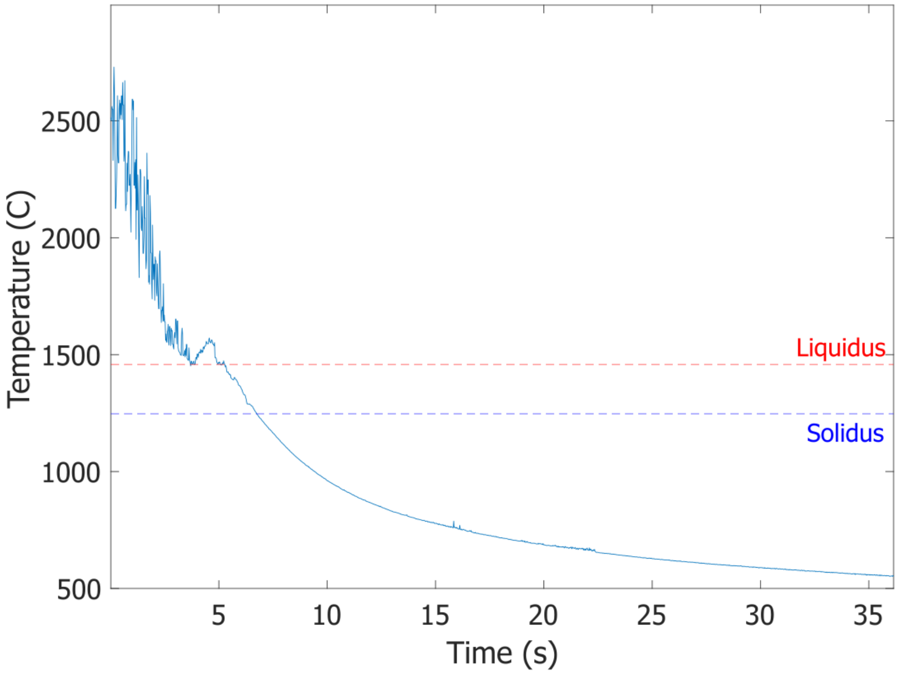

Figure 5.2: Full cooling curve of a single experimental bead

Since the solidification cooling curve was the data of interest, the portion of the cooling curve between the liquidus and solidus was then extracted. A linear regression was used to fit the data and the resulting slope was used to calculate the solidification cooling rate of each bead. A representative solidification cooling curve can be see in Figure 5.3.

The solidification cooling rate of each bead was plotted versus the heat input of the welding parameters (Figure 5.4).

From the plot of solidification cooling rates, it can be seen that as the heat input of the welding process was increased, the solidification cooling rate decreased. This decrease in heat input can be attributed to the significant

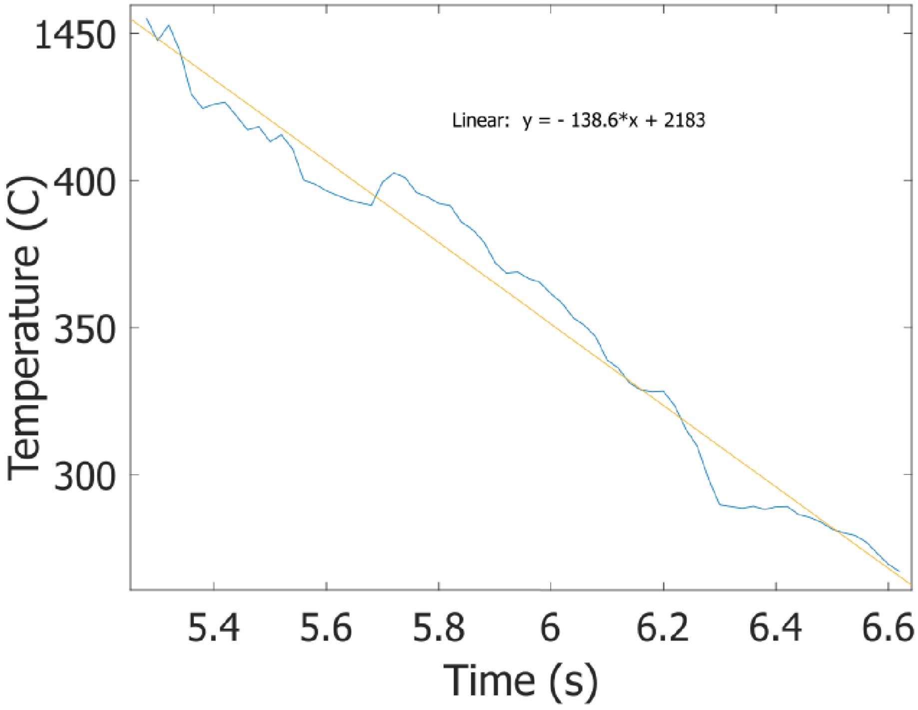

Figure 5.3: Solidification cooling curve of a single experimental bead

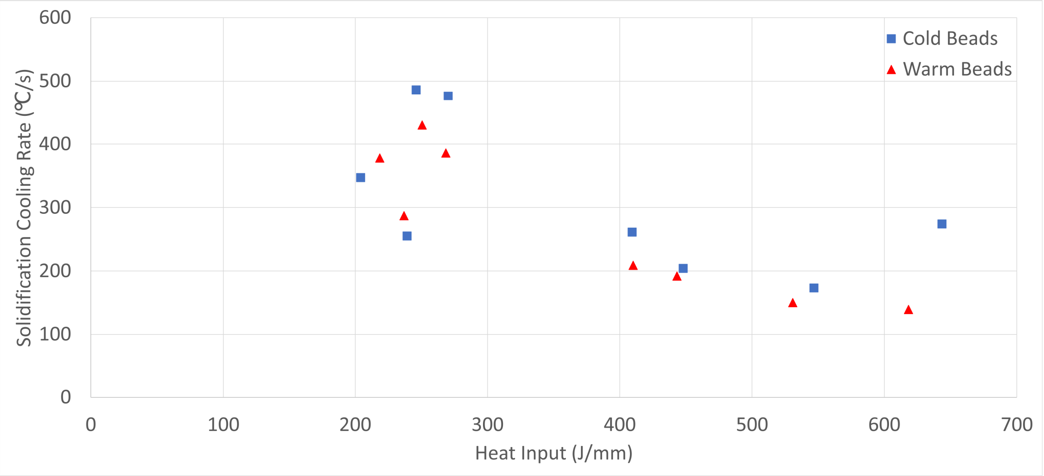

Figure 5.4: Solidification cooling rate versus heat input

increase in deposited material at higher heat input which will be quantified later on. There is also likely some heat saturation of the substrate at the highest heat inputs. As the heat input is increased, the small substrate plates become saturated with heat and heat cannot be removed from the weld plates as efficiently by conduction. This is reflected in the trend shown in Figure 5.4

where there is a leveling off in the decrease in solidification cooling rate above 500 $\frac{J}{mm}$.

In the solidification cooling rate data, the highest cooling rate point appears to be an experimental outlier. However, when the scatter in the 200 - 300 $\frac{J}{mm}$ heat input range is considered, it appears that this outlying point is due to normal experimental scatter. The source of this experimental scatter involves several possible experimental conditions. While all measured beads were within the stable welding region, there was still some surface waviness, leading to the possibility of local thick or thin regions being measured by the pyrometer. The GMAW process is also a consumable electrode process, meaning that any small damage to the wire surface can result in a loss of arc stability, a factor that would also contribute to experimental scatter.

5.3 Modeling of Solidification Cooling Rates

During the experimental WAAM process, a model was developed to predict the solidification cooling rates of initial weld passes using the Abaqus AM modeling package. Full details of the model can be found in Anqi Shao's master's thesis [64]. A comparison of a representative full weld bead solidification cooling curve with the solidification cooling curve predicted by the Abaqus model can be seen in Figure 5.5. Overall, the model predicted the general trend of the cooling curve very well. There is some mismatch due to the variation in the recorded thermal data. An especially poor fit can be seen in the 1000 - 550 $°C$ range as the model fails to predict the lower temperature cooling. Additionally, the model does not present the same scatter and signal saturation as seen in the experimental data due to the plasma. However, for the actual solidification cooling rate, the model generally gave reliable predictions. A comparison of model and experimental cooling rates can be seen in Figure 5.6. Generally, the cooling rates predicted were slightly lower than experimental values but fell within a 15% error. More analysis on the model's strengths and weaknesses and the work done to correct for them can be found in [64].

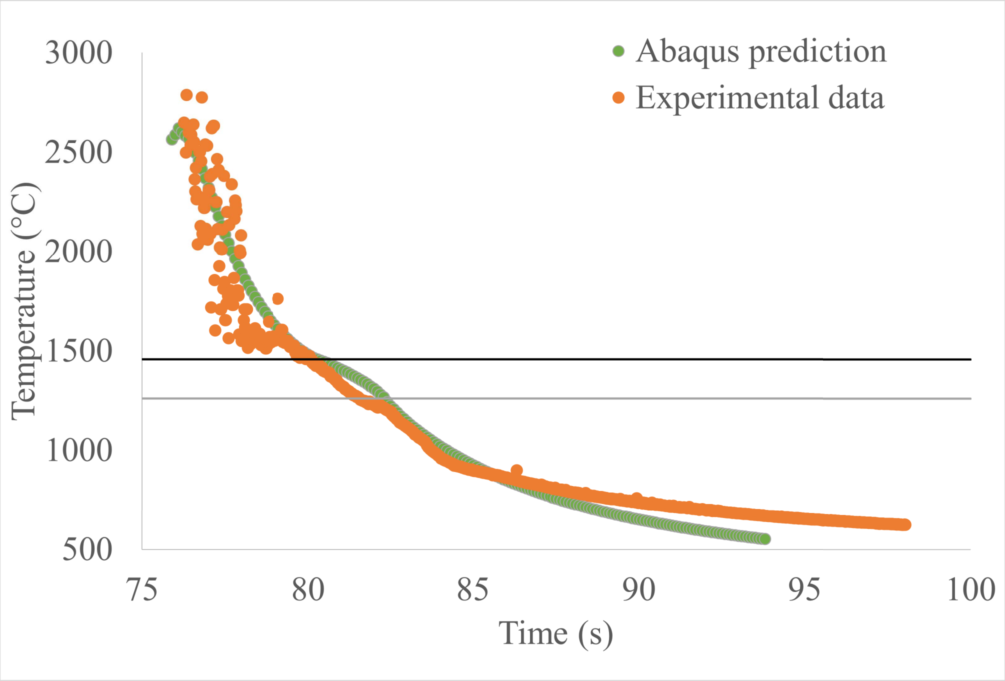

Figure 5.5: Abaqus model and experimental cooling curve comparison (liquidus and solidus marked)

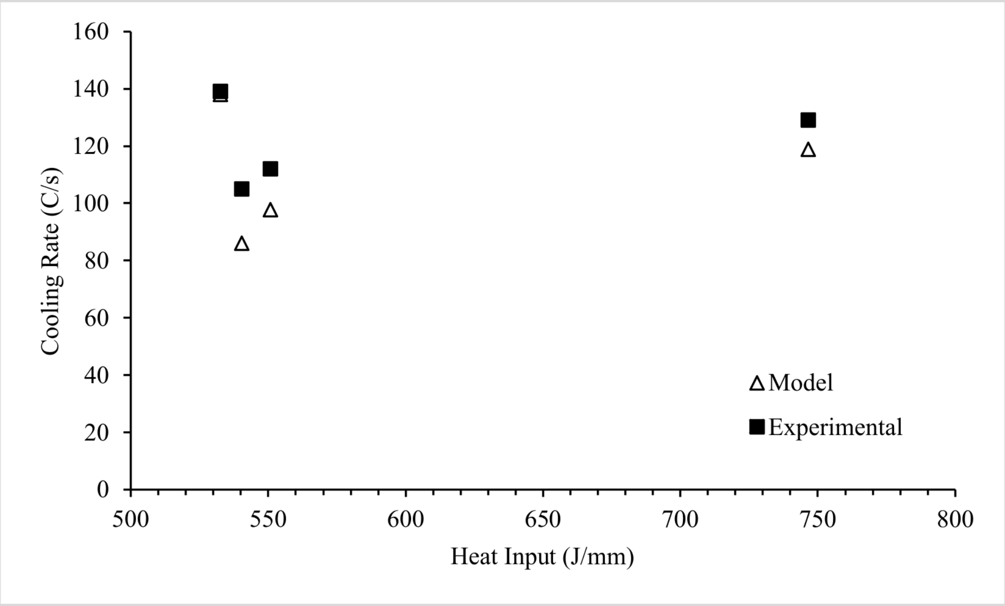

Figure 5.6: Abaqus model and experimental solidification cooling rate comparison [65]

5.4 Summary

17-4 PH samples were created using IA atomization and WAAM. Using a model created for the atomization method, liquid cooling rates were calculated for the IA samples. Over a range of powder sizes from about 100 - 1100 μm, the liquid cooling rate of the powders ranged from about 650 - 12000 °C/s. The WAAM cooling rates were captured using a two-colour pyrometer. The solidification cooling rates for the WAAM samples ranged from about 140 - 490 °C/s.

Chapter 6

Discussion

6.1 Microstructure Map

To establish a digital library of the solidification patterns, velocity of solidification measurements must be taken for each WAAM sample.

6.1.1 Angle of Columnar Growth

In order to determine the velocity of solidification, the angle of the columnar grains had to be taken for each weld bead sample. As the weld bead interface with the substrate plate demonstrated different amounts of penetration into the substrate plate due to local differences in heat input, it was not considered as a true horizontal point of reference. The calculation of the velocity of solidification was dependent on the trigonometric relationship with TTS and in order for the calculated values to be accurate, the horizontal plane used to find the angle of columnar growth had to be parallel to the movement of the torch. The bottom of the substrate plate was used to establish this true horizontal and all columnar growth angles were taken with respect to it. The relationship between the angle of columnar solidification and heat input has been plotted in Figure 6.1

Over the range of heat inputs tested there was not a large change in the angle of solidification. As the heat input increased, there was a slight decrease in the angle of solidification measured but the trend is not a significant one.

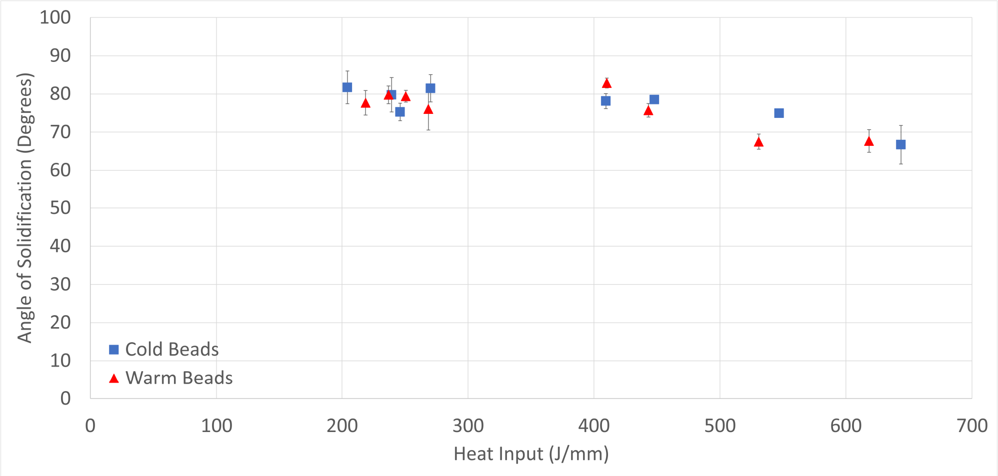

Figure 6.1: Angle of columnar solidification versus heat input

6.1.2 Bead Cross-Sectional Area

As GMAW is a consumable electrode process, increasing the heat input resulted in a significant change in the amount of material deposited. In order to account for the effect of this changing bead size, the cross-sectional area must be determined for each WAAM sample. To determine the cross-sectional area and account for any small variance along the length of the bead, two parallel cuts were made on either side of the pyrometer measurement area. The samples were mounted and the bead area was taken as an average of the two samples from each bead. The change in cross-sectional area can be visualized in Figure 6.2.

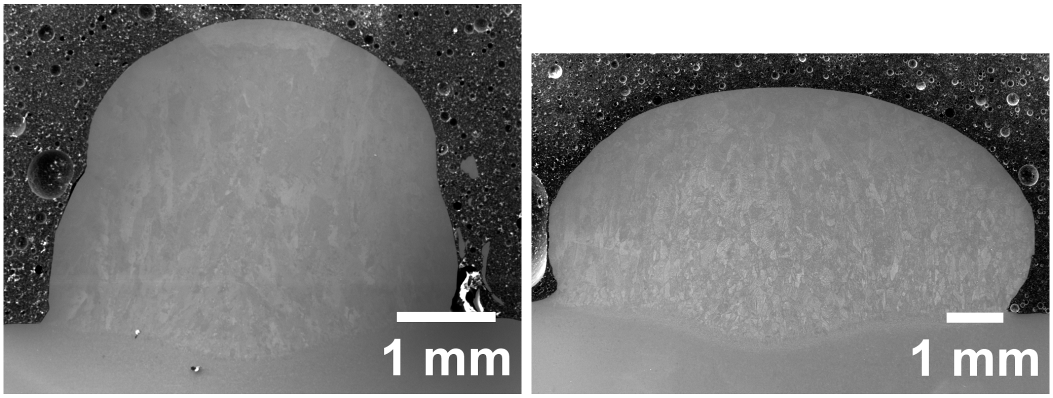

(a) 204 $\frac{J}{mm}$ sample cross-section (b) 644 $\frac{J}{mm}$ sample cross-section

Figure 6.2: Cross-Section of lowest and highest heat input samples

The relationship between cross-sectional bead area and the heat input has been plotted in Figure 6.3. It can be observed that there was a strong linear increase in the bead cross-sectional area as the heat input was increased in the WAAM process. This strong increasing trend in bead cross-sectional area increases the potential productivity of the WAAM process while limiting the potential dimensional accuracy. Additionally, as more material is deposited per mm of torch movement, it contributes to slower cooling rates at higher wire feed speeds.

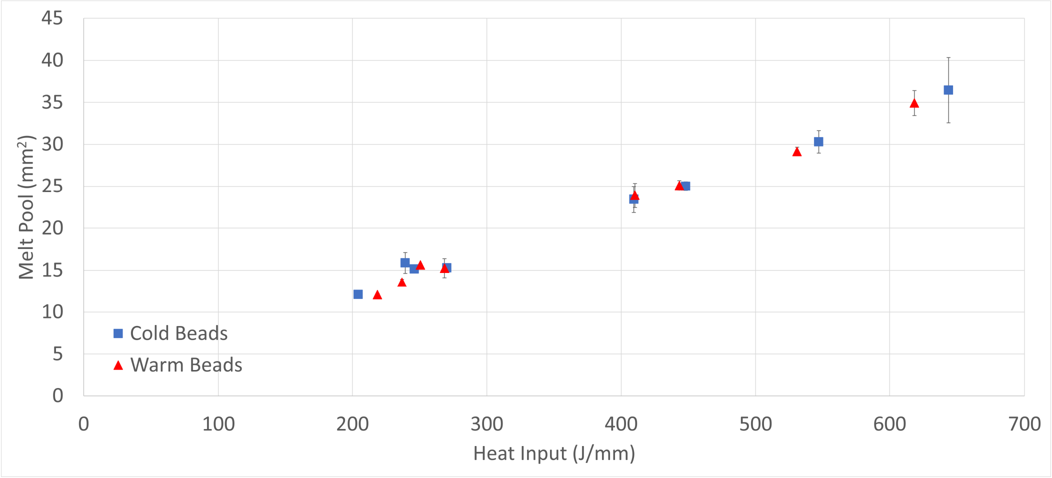

Figure 6.3: Cross-sectional bead area versus heat input

6.1.3 Normalized Velocity of Solidification

In order to reasonably consider the velocity of solidification, the large change in bead volume had to be accounted for. The bead cross-sectional area increased from 12 mm^2 to 36 mm^2 over the range of heat inputs studied meaning that at the highest heat inputs there was three times as much material to solidify as at the low range. To account for this change, the velocity of solidification was normalized with respect to the cross-sectional area so that the same amount of solidifying material was considered in each case. The relationship between normalized velocity of solidification and heat input has been plotted in Figure 6.4.

Overall, it can be seen that while the velocity of solidification does decrease with increasing heat input, mirroring the trend seen in solidification cooling

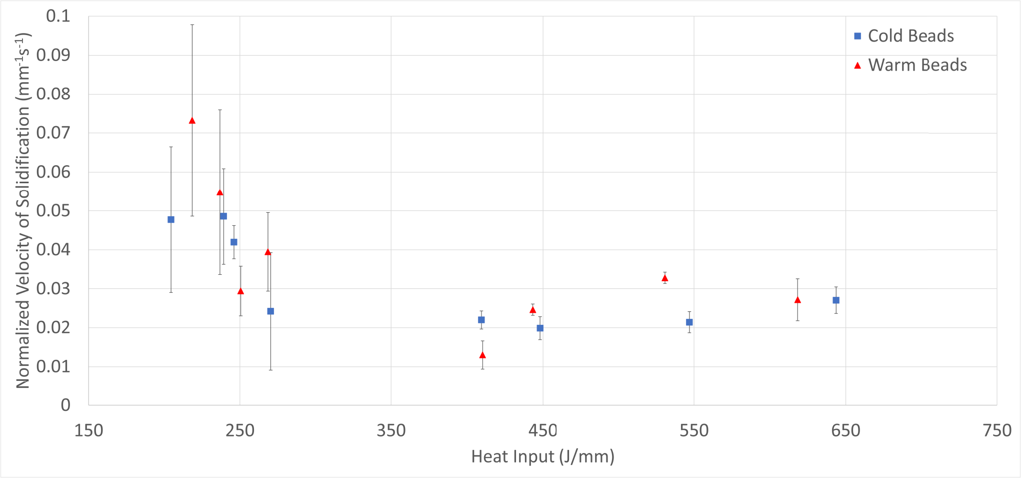

Figure 6.4: Normalized velocity of solidification versus heat input

rate, there is not a very significant change in either the angle of solidification or the velocity of the solidification front. In previous work, when using laser-based AM, the steep thermal gradients through the thickness of the melt pool led to changing velocities of solidification and changing solidification modes as the melt pool solidified [57]. In cases like these, angle of columnar growth measurements and velocity of solidification is a powerful tool to understand the kinetics of solidification [57], [66]. However, it has been shown here that in the more modest thermal gradients seen in WAAM, the results from columnar growth and velocity of solidification calculations show trends but provide little additional information about the solidification.

6.2 Effect of Cooling Rate on Microstructure and Properties

In order to assess the effect of changing cooling rates on the microstructure and mechanical properties, secondary dendrite arm spacing measurements were taken for all IA powders, ferrite fractions were quantified for IA powders and WAAM samples, and microhardness measurements were taken for all samples.

6.2.1 Secondary Dendrite Arm Spacing

Secondary dendrite arm spacing (SDAS) measurements were taken for every powder size with measurable dendrites to determine the effect of cooling rate on the scale of the microstructure and to establish the relationship between the liquid cooling rate and the SDAS. All measurements are of the dendritic portion of partially or fully dendritic particles. The relationship between SDAS and particle size can be seen in Figure 6.5

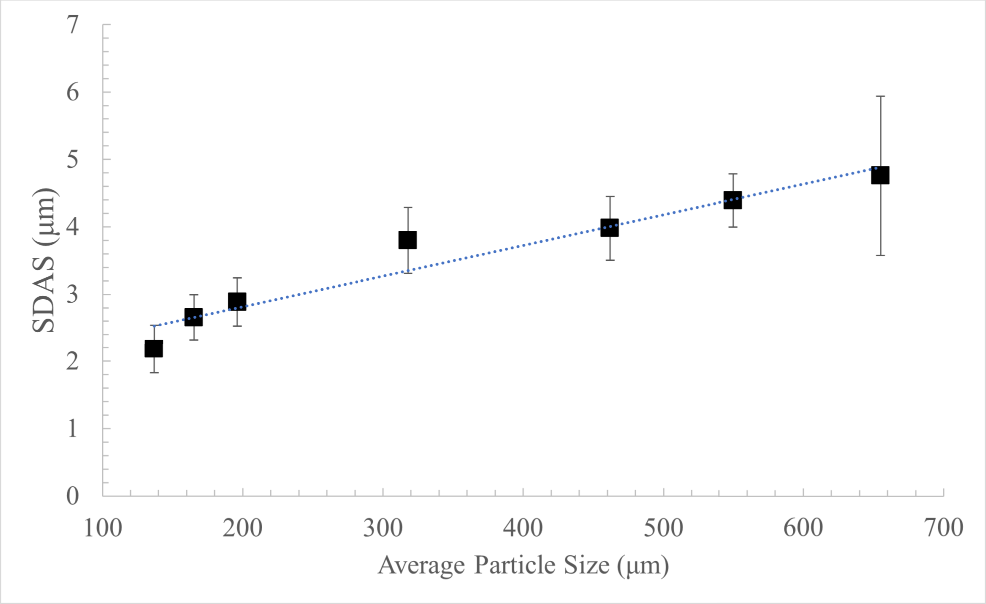

Figure 6.5: Secondary dendrite arm spacing versus particle size

As the powder particle size increases, the liquid cooling rate decreases (ie. cooling times are longer), as a result the SDAS increases. The direct relationship between SDAS and liquid cooling rate can be seen in Figure 6.6.

A linear regression is applied to the relationship between SDAS and liquid cooling rate to define the relationship as described in 3.4.5. The R-squared of 0.99 indicated the fit was excellent and the experimental data complied well with the theoretical relationship. Based on the linear regression, the material constants were found to be a B of 67.3 and an n of 0.36. There is no data available in other research on these material constants for 17-4PH, however Löser et. al. report a B of 68 and an n of 0.45 for a generic stainless steel [56]. The B found in this work corresponds very well to the value reported in

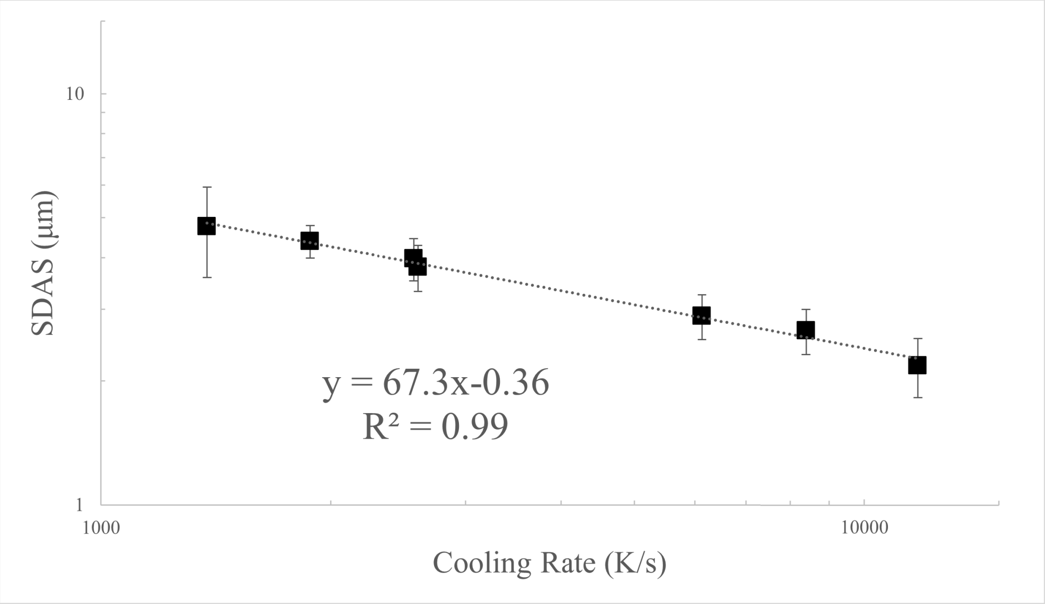

Figure 6.6: Secondary dendrite arm spacing versus liquid cooling rate

Löser but the n diverges fairly significantly. However, when derived from first principles, n is a geometric factor of $\frac{1}{3}$ [67], [68]. With this understanding, the experimental value of 0.36 for n, corresponds very closely with the expected value. The good fit of the linear regression and the good agreement of the materials constants with literature and fundamental values suggests that the calculated values for B and n can be used with confidence in the future to relate liquid cooling rate and SDAS for 17-4PH.

6.2.2 Effect of Cooling Rate on δ-Ferrite Fraction

In order to more precisely determine the effect of the cooling rate on the microstructure, δ-ferrite fractions were quantified for a selection of all cooling rates studied.

For the IA powder samples, the number of fully ferritic versus fully martensitic powder droplets were characterized for each size range. The relationship between δ-ferrite fraction and liquid cooling rate is plotted in Figure 6.7. At the lowest cooling rates, all the particles were fully martensitic and no dendritic samples were observed. The first evidence of austenite by-passing occurred at liquid cooling rates of 1400 °C/s, where 46 % of the powder was fully ferritic.

The δ-ferrite fraction increased steadily with decreasing cooling rate. While there was still martensitic particles at all cooling rates studied, at cooling rates faster than 8400 °C/s more than 90% of the powder particles were fully ferritic.

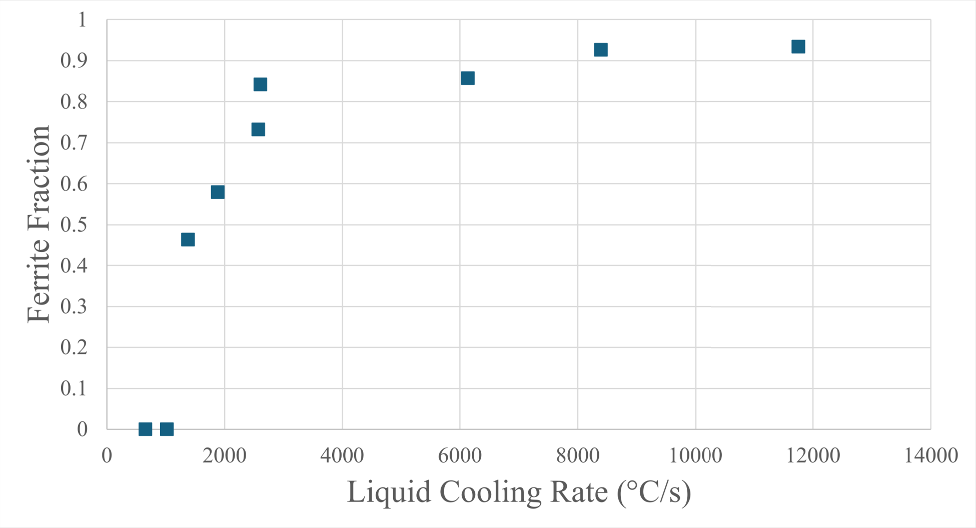

Figure 6.7: IA powder δ-ferrite fraction versus liquid cooling rate

In the WAAM samples, the ferrite fraction was determined using a manual point count method as described in ASTM E562-19 [69]. The relationship between solidification cooling rate and δ-ferrite fraction can be seen in Figure 6.8. The ferrite fraction of the WAAM samples varied from about 0.1 - 0.25 over the range of cooling rates studied. While there does seem to be a slight decrease in ferrite fraction as the cooling rate increases, the high degree of uncertainty in the data gives low confidence in this trend. Samples with the highest standard deviation represent samples that had large retained δ-ferrite grains as opposed to only narrow interdendritic retained δ-ferrite. All samples measured represent two-dimensional slices through a three-dimensional sample, depending on where the slice is taken it is easy to over- or under-represent the amount of δ-ferrite present, contributing to the wide standard deviations seen in the data.

6.2.3 Effect of Cooling Rate on Microhardness

Microhardness measurements were taken for all DSC and WAAM samples as well as for those IA powder samples that were large enough to be accurately

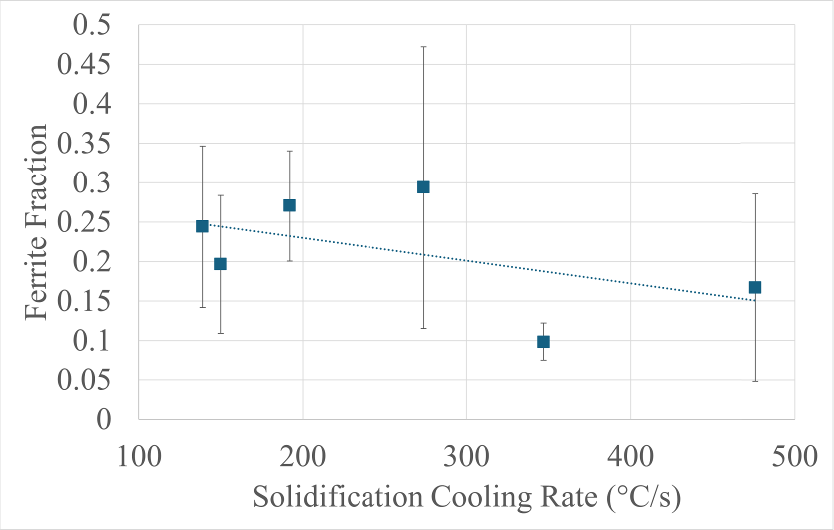

Figure 6.8: WAAM δ-ferrite fraction versus solidification cooling rate

measured. The relationship between microhardness and solidification cooling rate for DSC and WAAM samples can be seen in Figure 6.9. Overall, as the cooling rate increased, an increase in microhardness can be seen. As all of the samples measured here consist of martensite and δ-ferrite, this increase in hardness is likely due to grain refinement.

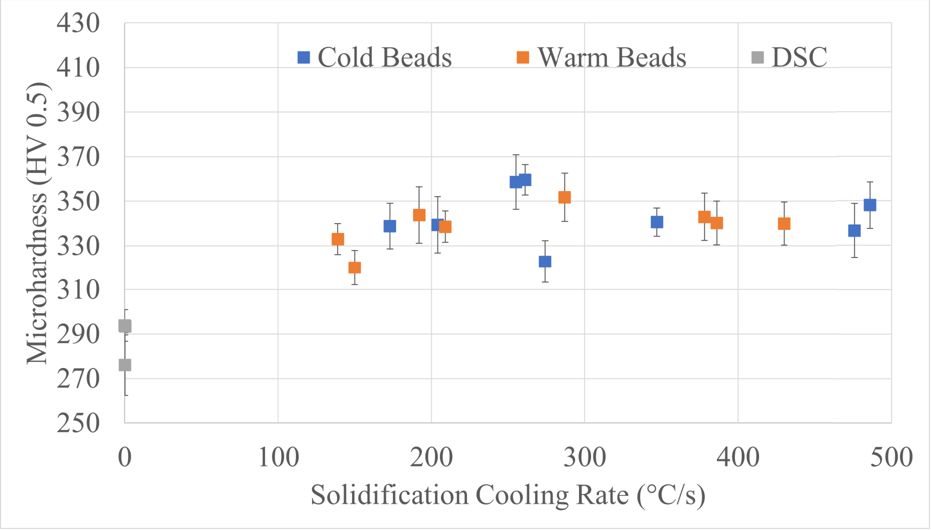

Figure 6.9: Microhardness of WAAM and DSC samples vs solidification cooling rate

To compare the effect of cooling rate over a greater range of cooling rates, liquid cooling rates were calculated for the WAAM samples. Liquid cooling rates were calculated using the same method as shown in 5, using the portion of the pyrometer data after the plasma signal saturation has passed and above the liquidus of the material. The relationship between microhardness and liquid cooling rate can be see in Figure 6.10, where the powder hardness values were taken only from fully martensitic powder particles. As before, a significant increase in microhardness can be seen from the DSC cooling rate range to the WAAM samples. The powder samples, on the other hand, are much softer than the WAAM samples, in the range of the DSC hardness. As seen in the earlier micrographs, the IA powders contain solidification shrinkage porosity which will contribute to a decrease in microhardness even when the area measured had no visible porosity. There is a slight decrease in the microhardness over the range of powder cooling rates measured. This indicates that the powder samples that appear fully martensitic still contain a large fraction of untransformed ferrite as the cooling rate increases and less time is available for the austenite transformation needed to form martensite.

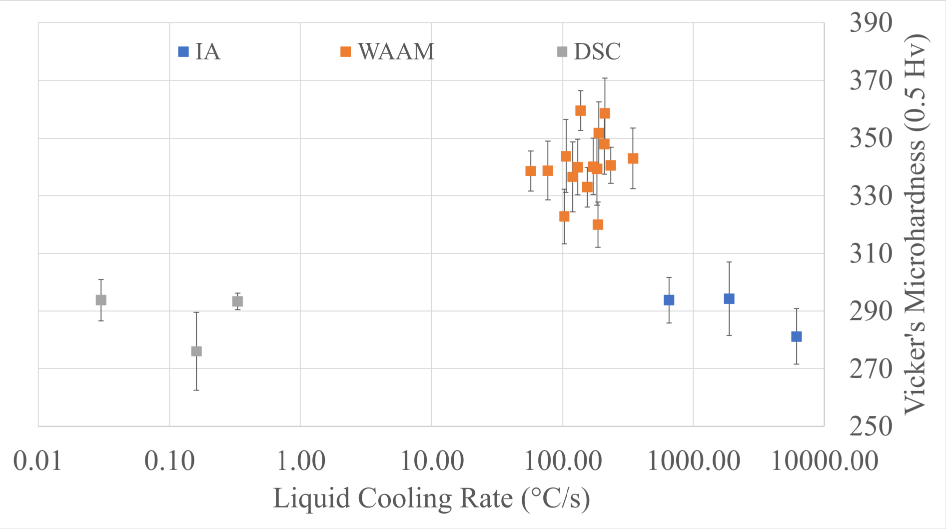

Figure 6.10: Effect of liquid cooling rate on microhardness with DSC (grey), WAAM (orange), and powder (blue) samples

6.3 Summary

Trends relating to the increasing the WAAM heat input were observed with respect to various responding variables. As the heat input of the WAAM process was increased the angle of columnar growth did not vary greatly, but a slight decrease was observed. As WAAM is a consumable electrode process, the wire feed speed increases as the heat input increases. Due to this relationship, as the heat input was increased, a strong linear increase in bead area was observed. The velocity of solidification was normalized with respect to the cross-sectional bead area and the resulting normalized velocity of solidification decreased as the heat input was increased, reflecting a slower solidification front movement as the solidification cooling rate decreased.

The effect of cooling rate on microstructure and properties was investigated. In the IA powders, secondary dendrite arm spacing was related to the cooling rate. Based on the well-known relationship between SDAS and cooling rate, the material constants B and n of 17-4 PH were found to be 67.3 and 0.36, respectively. These values fit very well with literature and fundamental values. In the IA powder samples, fully retained δ-ferrite powder particles were found to occur starting at cooling rates of 1400 °C/s. Above 8400 °C/s, the IA powder samples were almost entirely δ-ferrite. In the WAAM samples, increasing cooling rate resulted in slightly lower δ-ferrite fractions in the as-deposited microstructure. High uncertainty gives low confidence to this trend. Finally, microhardness measurements were taken for IA powder, WAAM, and DSC samples. A marked increase in microhardness is observed from the DSC cooling rate range to the WAAM cooling rate range. However, this hardness increase does not continue into the IA powder cooling rate range. IA powders show a significant decrease in microhardness compared to WAAM powders due to retained δ-ferrite.

Chapter 7

Conclusions

17-4PH is a precipitation hardenable stainless steel alloy that provides an attractive combination of corrosion resistance and mechanical strength that leads to its use in a range of industries including marine, nuclear, aerospace, and paper. These wide industrial applications make 17-4PH a desirable candidate for additive manufacturing (AM) to enable on-the-spot replacement part printing at various distributed locations. To be used as an industrial AM alloy, the solidification behaviour of 17-4 PH must be well-understood.

To study the solidification behaviour of 17-4 PH, samples were created using differential scanning calorimetry (DSC), wire and arc additive manufacturing (WAAM), and impulse atomization (IA). In DSC samples that featured cooling rates from 2 - 20 °C/min a martensitic matrix with interdendritic δ-ferrite was observed. To create uniform, single-pass beads using a WAAM system, a stable welding region was established for 17-4PH stainless steel over a torch travel speed of 4.1 - 2.5 $\frac{mm}{s}$ and a wire feed speed of 38.5 - 76.2 $\frac{mm}{s}$. These parameters gave current of voltage parameters of 80 - 130 A and 12 - 14 V, respectively for an overall heat input range of 200 - 650 $\frac{J}{mm}$. The cooling rates, calculated from two-colour pyrometer data ranged from 140 - 490 °C/s. In the higher cooling rate WAAM samples, the microstructure featured a largely columnar microstructure with a small equiaxed region at the surface of the bead.

The phases in the WAAM samples, similar to those of the DSC consisted of martensite and δ-ferrite. The fraction of δ-ferrite over the range of heat inputs measured was fairly uniform, with an average δ-ferrite fraction of 0.21 ± 0.09 in the WAAM samples. The IA powders had a liquid cooling rate range of 600 - 12000 °C/s. In the IA samples, two major morphologies were observed, martensitic lathes and dendrites. Based on EBSD data, the dendrites were identified as δ-ferrite. At the lowest cooling rates, the powder particles were completely martensitic. As the cooling rate was increased, the alloy did not spend enough time in the austenite forming region of solidification while cooling and reached room temperature as δ-ferrite. Starting at cooling rates 1900 °C/s, more than 50 % of the powder particles were fully δ-ferrite. At the highest cooling rates, more than 90 % of the powder experienced austenite by-passing and was fully δ-ferrite.

To further study the solidification behaviour of the WAAM beads over the cooling rates studied, the velocity of the solidification front in the beads was measured from the angle of solidification of the columnar microstructure. As the heat input of the WAAM process was increased a slight decrease in the angle of growth was observed. As WAAM is a consumable electrode process, the wire feed speed increases as the heat input increases. Due to this relationship, as the heat input was increased, a strong linear increase in bead area was observed. The velocity of solidification was normalized with respect to the cross-sectional bead area and the resulting normalized velocity of solidification decreased as the heat input was increased, reflecting a slower solidification front movement as the solidification cooling rate decreased.

To assess the effect of the microstructural changes on the alloy, microhardness measurements were taken for all the samples. From the DSC to the WAAM samples, the microhardness increased from 290 HV 0.5 to a maximum of 360 HV 0.5. These samples are composed of the same microstructural phases so this increase in hardness is likely due to grain refinement from the increasing cooling rate. The microhardness of the IA powders was around 290 HV 0.5 at all cooling rates measured. This significant drop in hardness at higher cooling rates is likely due to a combination of porosity and retained δ-ferrite in samples that appear fully martensitic.

While this study covered a wide range of cooling rates, much work remains to be done to fully characterize the solidification of 17-4 PH. As AM processes involve repeated passes of the heat source, more work is required to characterize the microstructure of the second bead and the effect on the initial deposited microstructure. It was also seen in the DSC work that the initial solidification structure is very sensitive to composition differences even within the alloy definition. The effect of this sensitivity over a wider range of cooling rates should be studied. Additionally, this work focused on one AM process but the same process could be applied to any AM method. The wide range of AM fabrication methods have a wide range of heat inputs and cooling rates and it would be beneficial to characterize to complete the picture of the initial solidification of 17-4 PH under different conditions. More work could be done using Abaqus modelling to improve the fit of the model on the lower temperature range of the cooling curve. Finally, 17-4 PH is solutionized and aged before use to bring out the alloy's characteristic high hardness and strength. The effect of this common industrial heat treatment on these varying initial solidification structures should be studied.

References

[1] *Additive manufacturing - general principles - terminology*, ISO/ASTM 52900:2021(E), ASTM, 2015.

[2] D. Bourell and T. Wohlers, "Introduction to additive manufacturing," *ASM Handbook*, vol. 24, 2020.

[3] P. Stavropoulos, *Additive Manufacturing: Design, Process, and Applications*. SpringerBriefs, 2023.

[4] R. P. Martukanitz, "Directed-energy deposition processes," *ASM Handbook*, vol. 24, 2020.

[5] *Additive manufacturing - design - directed energy deposition*, ASTM F3413 - 19, ASTM, 2020.

[6] T. A. Rodrigues, V. Duarte, R. M. Miranda, T. G. Santos, and J. P. Oliveira, "Current status and perspectives on wire and arc additive manufacturing (waam)," *Mat*, vol. 12, no. 7, p. 1121, 2019.

[7] S. Selvi, A. Vishvaksenan, and E. Rajasekar, "Cold metal transfer (cmt) technology - an overview," *Defence Tech*, vol. 14, no. 1, pp. 28–44, 2018.

[8] C. W. B. Group, *Gas metal arc transfer modes - part 1 - short circuiting and globular*, `https://www.cwbgroup.org/association/how-it-works/gas-metal-arc-transfer-modes-part-1-short-circuiting-and-globular`, Last Accessed on Jan 14, 2024, 2024.

[9] B. Cong, J. Ding, and S. Williams, "Effect of arc mode in cold metal transfer process on porosity of additively manufactured al-6.3% cu alloy," *Int J Adv Manuf Technol*, vol. 79, no. 9–12, pp. 1593–1606, 2015.

[10] *Additive Manufacturing, Design, Functionally Graded Additive Manufacturing*. ASTM International, 2021.

[11] M. Murayama, Y. Katayama, and K. Hono, "Microstructural evolution in a 17-4 ph stainless steel after aging at 400 c," *Met Mat Trans A*, vol. 30A, pp. 345–353, 1999.

[12] W. Yoo, J. Lee, K. Youn, and Y. Rhyim, "Study on the microstucture and mechanical properties of 17-4 ph stainless steel depending on heat treatment and aging time," *Solid State Phenom*, vol. 118, pp. 15–20, 2006.

[13] F. Niessen, N. Tiedje, and J. Hald, "Kinetics modeling of delta-ferrite formation and retainment during casting of supermartensitic stainless steel," *Mat and Des*, vol. 118, pp. 138–145, 2017.

[14] *Standard specification for hot-rolled and cold-finished age-hardening stainless steel bars and shapes*, ASTM A564/A564M - 13, ASTM, 2017.

[15] T. Lienert, T. Siewert, S. Babu, and V. Acoff, *Asm handbook, volume 6a: Welding fundamentals and processes*, 2011.

[16] A. Bhaduri, S. Sujith, G. Srinivasan, T. Gill, and S. Mannan, "Optimized postweld heat treatment procedures for 17-4 ph stainless steels," *Weld. J.*, vol. 74, no. 5, p. 153, 1995.

[17] D. Kotecki, "Welding of stainless steels," *ASM handbook*, vol. 6, pp. 677–707, 1993.

[18] S. Washko and G. Aggen, "Wrought stainless steels," *Properties and selection: irons, steels, and high-performance alloys*, pp. 841–907, 1990.

[19] M. B. Balajaddeh and H. Naffakh-Moosavy, "Pulsed nd: Yag laser welding of 17-4 ph stainless steel: Microstructure, mechanical properties, and weldability investigation," *Optics & Laser Technology*, vol. 119, p. 105 651, 2019.

[20] A. Caballero, J. Ding, S. Ganguly, and S. Williams, "Wire + arc additive manufacture of 17-4 ph stainless steel: Effect of different processing conditions on microstructure, hardness, and tensile strength," *J. Mater. Process. Technol.*, vol. 268, pp. 54–62, 2019.

[21] G. E. Linnert, "Welding precipitation-hardening stainless steels," *Weld. J.*, vol. 36, no. 1, p. 9, 1957.

[22] R. J. Hamlin, "Investigation of precipitation and hardening response of maraging stainless steels 17-4 and 13-8+ mo during multi-pass welding," PhD thesis, Lehigh University, 2017.

[23] J. Lippold and W. Savage, "Solidification of austenitic stainless steel weldments: Part 2—the effect of alloy composition on ferrite morphology," *Weld. J.*, vol. 59, no. 2, 48s–58s, 1980.

[24] J. Elmer, S. Allen, and T. Eagar, "Microstructural development during solidification of stainless steel alloys," *Metall. Mater. Trans. A*, vol. 20, pp. 2117–2131, 1989.

[25] F. Pickering, *Physical Metallurgy and the Design of Steels*. Applied Science Publishers Ltd., 1978.

[26] H. Bhadeshia and R. Honeycombe, *Steels: microstructure and properties*. Butterworth-Heinemann, 2017.

[27] A. Ziewec, A. Sielinka-Lipiec, and E. Tasak, "Microstructure of welded joints of x5crnicunb16-4 (17-4 ph) martensitic stainless steel after heat treatment," *Arch of Met and Mat*, vol. 59, no. 3, pp. 965–970, 2014.

[28] M. R. Stoudt, C. E. Campbell, and R. E. Ricker, "Examining the relationship between post-build microstructure and the corrosion resistance of additively manufactured 17-4ph stainless steel," *Materialia*, vol. 22, p. 101 435, 2022.

[29] W. Smith, *Structure and Properties of Engineering Alloys*. McGraw-Hill Book Company, 1981.

[30] U. Viswanathan, S. Banerjee, and R. Krishnan, "Effects of aging on the microstructure of 17-4 ph stainless steel," *Materials Science and Engineering: A*, vol. 104, pp. 181–189, 1988.

[31] L. Quackatz, A. Griesche, and T. Kannengießer, "Rapid solidification during welding of duplex stainless steels–in situ measurement of the chemical concentration by laser-induced breakdown spectroscopy (libs)," in *IOP Conference Series: Materials Science and Engineering*, IOP Publishing, vol. 1274, 2023, p. 012 018.

[32] S. Li, Y. Wang, and X. Wang, "Influence of mo additions on the mechanical properties of cast duplex stainless steels before and after thermal aging," *Metals*, vol. 9, no. 3, p. 295, 2019.

[33] K. Weman, *Welding processes handbook*. Elsevier, 2011.

[34] S. Kou, *Welding metallurgy*. John Wiley & Sons, 2020.

[35] S. David, J. Vitek, R. Reed, and T. Hebble, "Effect of rapid solidification on stainless steel weld metal microstructures and its implications on the schaeffler diagram," Oak Ridge National Lab.(ORNL), Oak Ridge, TN (United States), Tech. Rep., 1987.

[36] Y. Lu, H. Yu, and R. D. Sisson Jr, "The effect of carbon content on the c/a ratio of as-quenched martensite in fe-c alloys," *Materials Science and Engineering: A*, vol. 700, pp. 592–597, 2017.

[37] M. Alnajjar, F. Christien, K. Wolski, and C. Bosch, "Evidence of austenite by-passing in a stainless steel obtained from laser melting additive manufacturing," *Additive Manufacturing*, vol. 25, pp. 187–195, 2019.

[38] R. Schroeder, G. Hammes, C. Binder, and A. N. Klein, "Plasma debinding and sintering of metal injection moulded 17-4ph stainless steel," *Materials Research*, vol. 14, pp. 564–568, 2011.

[39] S. Vunnam, A. Saboo, C. Sudbrack, and T. L. Starr, "Effect of powder chemical composition on the as-built microstructure of 17-4 ph stainless steel processed by selective laser melting," *Additive Manufacturing*, vol. 30, p. 100 876, 2019.

[40] C. Das, H. Dey, G. Srinivasan, S. Albert, A. Bhaduri, and A. Dasgupta, "Weldability of 17-4ph stainless steel in overaged heat treated condition," *Science and Technology of Welding and Joining*, vol. 11, no. 5, pp. 502–508, 2006.

[41] S. Gaudez, J. Macchi, G. Geandier, S. Denis, and S. Y. Allain, “Thermodynamic approach to describe the martensite phase transformation kinetics via the stabilization of austenite,” *Metall Mater Trans A*, pp. 1–15, 2024.

[42] T. Furuhara, K. Kikumoto, H. Saito, T. Sekine, T. Ogawa, S. Morito, and T. Maki, “Phase transformation from fine-grained austenite,” *ISIJ international*, vol. 48, no. 8, pp. 1038–1045, 2008.

[43] L. Facchini, N. Vicente Jr, I. Lonardelli, E. Magalini, P. Robotti, and A. Molinari, “Metastable austenite in 17–4 precipitation-hardening stainless steel produced by selective laser melting,” *Advanced Engineering Materials*, vol. 12, no. 3, pp. 184–188, 2010.

[44] H. K. Rafi, D. Pal, N. Patil, T. L. Starr, and B. E. Stucker, “Microstructure and mechanical behavior of 17-4 precipitation hardenable steel processed by selective laser melting,” *Journal of materials engineering and performance*, vol. 23, pp. 4421–4428, 2014.

[45] Y. Sun, R. J. Hebert, and M. Aindow, “Effect of laser scan length on the microstructure of additively manufactured 17-4ph stainless steel thin-walled parts,” *Additive Manufacturing*, vol. 35, p. 101 302, 2020.

[46] H. Lashgari, C. Kong, E. Adabifiroozjaei, and S. Li, “Microstructure, post thermal treatment response, and tribological properties of 3d printed 17-4 ph stainless steel,” *Wear*, vol. 456, p. 203 367, 2020.

[47] S. Sabooni, A. Chabok, S. Feng, H. Blaauw, T. Pijper, H. Yang, and Y. Pei, “Laser powder bed fusion of 17–4 ph stainless steel: A comparative study on the effect of heat treatment on the microstructure evolution and mechanical properties,” *Additive Manufacturing*, vol. 46, p. 102 176, 2021.

[48] J. Valloton, D. Herlach, H. Henein, and D. Sediako, “Microstructural quantification of rapidly solidified undercooled d2 tool steel,” *Metall Mater Trans A*, 2017.

[49] J. B. Wiskel, H. Henein, and E. Maire, “Solidification study of aluminum alloys using impulse atomization: Part i: Heat transfer analysis of an atomized droplet,” *Canadi Metall Quarterly*, vol. 41, no. 1, pp. 97–110, 2002.

[50] J. B. Wiskel, K. Navel, H. Henein, and E. Maire, “Solidification study of aluminum alloys using impulse atomization: Part ii. effect of cooling rate on microstructure,” *Canadi Metall Quarterly*, vol. 41, no. 2, pp. 193–204, 2002.

[51] J. Valloton, A.-A. Bogno, M. Rappaz, and H. Henein, “Numerical model of rapidly solidified droplets of al–33 wt pct cu eutectic growth,” *Metall Mater Trans A*, vol. 53, no. 2, pp. 460–469, 2022.

[52] *Optris ctratio 2m technical data*, Optris Infrared Sensing, Portsmouth, NH, 2021.

[53] *Practice for microetching metals and alloys*, ASTM International Standard E0407-07, 2015.

[54] *Standard test methods for determining average grain size*, ASTM International Standard E112 - 13, 2014.

[55] E. Vandersluis and C. Ravindran, "Comparison of measurement methods for secondary dendrite arm spacing," *Metall Microstruc Anyl*, vol. 6, no. 1, pp. 89–94, 2017.

[56] W. Loser, S. Thiem, and M. Jurisch, "Solidification modelling of microstructures in near-net-shape casting of steels," *Mat Sci Eng A*, vol. 173, no. 1–2, pp. 323–326, 1993.

[57] M. Gremaud, "Solidification rapide: Étude microstructurale des alliages al-fe après fusion superficielle par laser," PhD thesis, EPFL, 1990.

[58] Y. Li, Y. Liu, C. Liu, C. Li, and H. Li, "Mechanism for the formation of z-phase in 25cr-20ni-nb-n austenitic stainless steel," *Mat Lett*, vol. 233, pp. 16–19, 2018.

[59] D. Olson, "Prediction of austenitic weld metal microstructure and properties," *Welding Research Supplement*, 281-s –295-s, 1985.

[60] J. Lang and I. Fieldhouse, "Measurement of thermal properties. progress report no. 4 for august and september, 1957," Illinois Inst. of Tech., Chicago. Armour Research Foundation, Tech. Rep., 1957.

[61] Y. Mahmoodkhani, U. Ali, S. Imani Shahabad, A. Rani Kasinathan, R. Esmaeilizadeh, A. Keshavarzkermani, E. Marzbanrad, and E. Toyserkani, "On the measurement of effective powder layer thickness in laser powder-bed fusion additive manufacturing of metals," *Progress in Additive Manufacturing*, vol. 4, pp. 109–116, 2019.

[62] R. C. Weast, *CRC handbook of chemistry and physics.* CRC Press Inc., Boca Raton, FL, 1986.

[63] J. Welty, G. L. Rorrer, and D. G. Foster, *Fundamentals of momentum, heat, and mass transfer.* John Wiley & Sons, 2020.

[64] A. Shao, *Modelling of the thermal history during submerged arc welding and wire and arc additive manufacturing*, M.Sc. thesis, University of Alberta, 2022.

[65] A. McDonald, A. Shao, K. Meszaros, A. Qureshi, M. Rappaz, T. Wolfe, and H. Henein, "Microstructure map of rapidly solidified 17-4ph stainless steel," in *Proc. 62nd Conf. Metall.* 2023, pp. 489–492.

[66] M. Zimmermann, M. Carrard, and W. Kurz, "Rapid solidification of al-cu eutectic alloy by laser remelting," *Acta Metallurgica*, vol. 37, no. 12, pp. 3305–3313, 1989.

[67] H. Jones, *Rapid Solidification of Metals and Alloys*. The Institution of Metallurgists, 1983, pp. 40–45.

[68] L. Tian, Y. Guo, J. Li, F. Xia, M. Liang, and Y. Bai, "Effects of soldification cooling rate on the microstructure and mechanical properties of a cast al-si-cu-mg-ni piston alloy," *Materials*, vol. 11, no. 7, p. 1230, 2018.

[69] *Standard test method for determining volume fraction by systematic manual point count*, ASTM International Standard E562-19, 2019.

[70] S. N. E. M. Ibrahim, *Plasma transferred arc additive manufacturing using 17-4 precipitation hardened stainless steel*, M.Sc. thesis, University of Alberta, 2020.

[71] B. L. Bramfitt and A. O. Benscoter, *Metallographer's Guide - Practices and Procedures for Irons and Steels*. ASM International, 2002.

Appendix A

Etching Trials

When identifying and analysing microstructures in samples, proper etching is a vital component to allow for phase identification. With the variety of phases and structures observed in the range of solidification times studied in this work, etching to reveal the structures was not a trivial task. The three different etchants studied will be discussed in this chapter.

A.1 Kalling's Reagent

Previous work on 17-4PH recommended etching with Kalling's reagent [70]. The results of this etchant on both powder and bulk samples can be seen below.

A.1.1 Powder Sample Etching

In powder samples, Kalling's reagent resulted in extremely undifferentiated samples. Martensite is darkened when etching with Kalling's [71], and this was seen in the larger, slower cooling rate samples (Figure A.1a). However, the samples with a dendritic structure were not well etched. The only place that dendrites were consistently visible was around the center of powders that experienced shrinkage porosity. This phenomenon can be observed in Figure A.1b. For powder particles that were fully dendritic had some slight colouring to suggest the existence of the structure but the etching was not strong enough to allow for good quality imaging or analysis (Figure A.1c). In other powder particles, grain boundaries were clearly defined. However, particles with clearly etched grain boundaries experienced fairly severe pitting with no other visible phases, as seen in Figure A.1d.

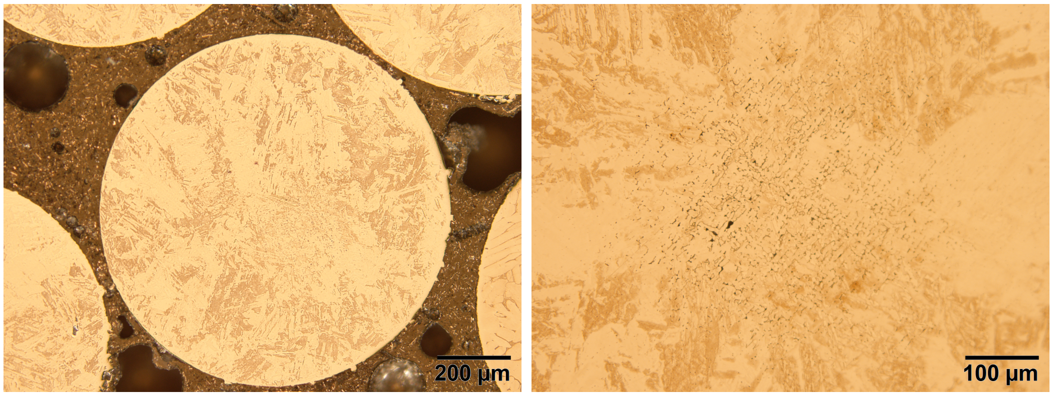

(a) A 1.18 mm - 850 μm martensitic particle etched with Kalling's reagent

(b) Well-etched dendrites due to shrinkage porosity

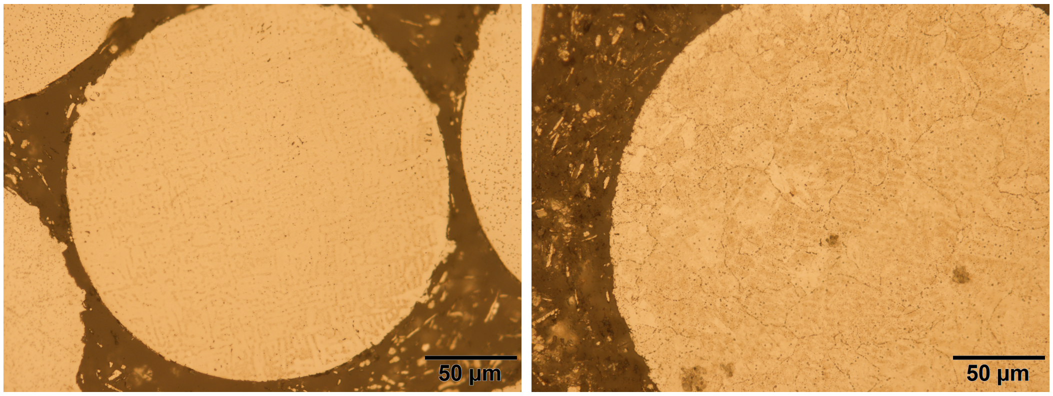

(c) Poorly etched dendrites in a 250 - 212 μm particle

(d) Well-etched grain boundaries in a 355 - 300 μm particle

Figure A.1: IA powder samples etched with Kalling's reagent

A.1.2 WAAM Sample Etching

In WAAM samples, Kalling's reagent etched δ ferrite very well but was not effective in revealing additional texture or details in the rest of the microstructure. When etched with Kalling's reagent, grains were very clearly defined as can be seen in Figure A.2. However, while the outline of the structure was very clear under SEM, there was not sufficient detail revealed with Kalling's in the rest of the structure for this to be the preferred etchant for bulk samples.

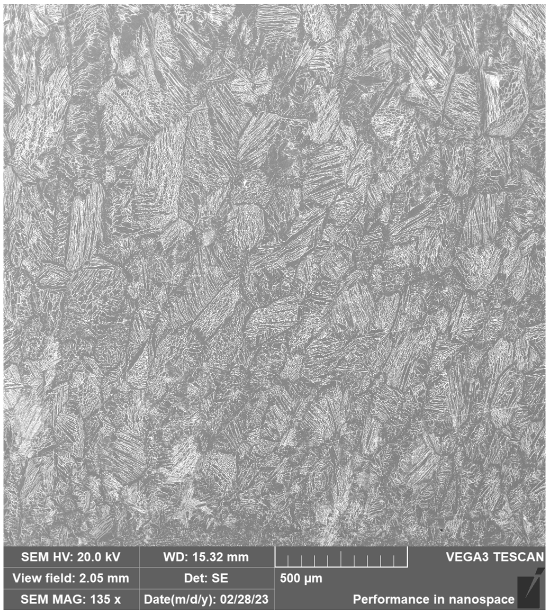

Figure A.2: Visible grains in 17-4PH WAAM sample, Kalling's reagent etch

A.2 Vilella's Reagent

Vilella's reagent is a recommended etchant for precipitation hardening stainless steels [53]. The version used in this work included the optional 3% H_2O_2 to accelerate the reaction. Vilella's was tested on both powder and bulk samples with the results shown below.

A.2.1 Powder Sample Etching

In order to etch powder samples fully, etching times of up to 12 minutes were used without evidence of significant overetching. Various samples etched with Vilella's reagent can be seen in Figure A.3. Vilella's reagent was able to successfully etch the dendritic δ ferrite structure seen in the high cooling rate samples (Figure A.3a). Additionally, the fully martensitic particles etched very well, with well-delineated lathes visible (Figures A.3b and A.3c).

For samples in the highest size range that consisted of a large fraction of martensite with smaller sections of δ ferrite dendrites, the dendrites were often under-etched when the martensite was fully etched (Figure A.4). This made a proper etch of the particles with a combined microstructure very challenging. However, even in samples with this challenge, both phases were clearly delineated and visible.

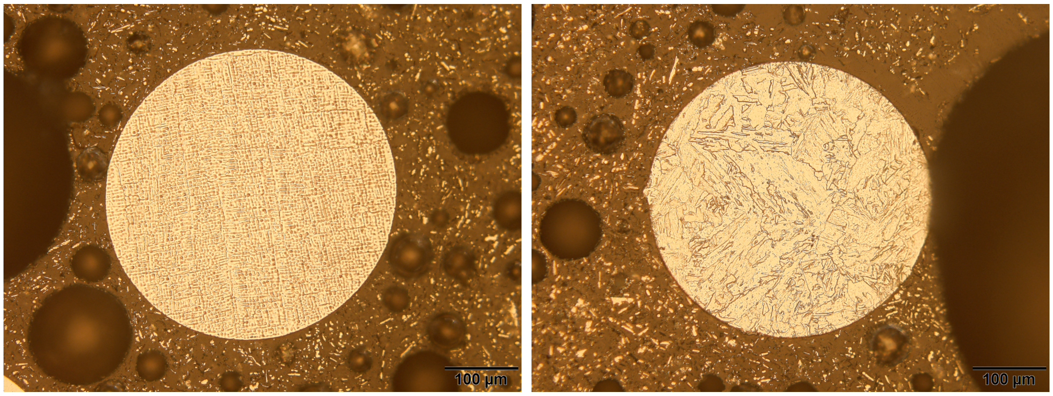

(a) A 500 - 425 μm dendritic particle etched with Vilella's reagent

(b) A 500 - 425 μm martensitic particle etched with Vilella's reagent

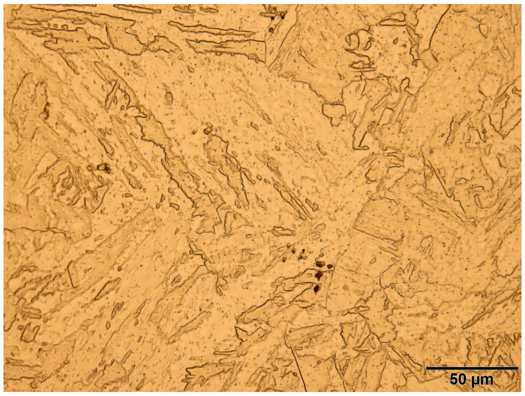

(c) Higher magnification of martensite etched with Vilella's reagent

Figure A.3: IA powder samples etched with Vilella's reagent

A.2.2 WAAM Sample Etching

The general structure of the WAAM beads was etched very clearly with a good visualization of the columnar solidification of the beads and a very clear boundary revealed between the bead and the base plate (Figure A.5). As shown in Figure A.6, Vilella's reagent was capable of providing a good etch of

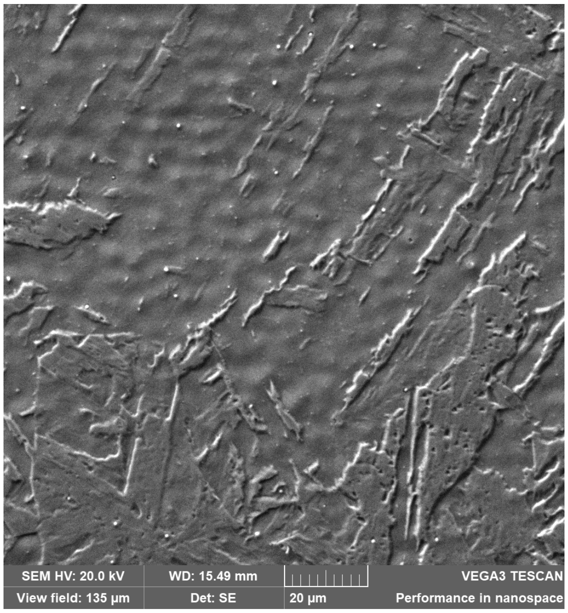

Figure A.4: Under-etched dendrites in a martensitic-dendritic particle

general structure. In Figure A.6b, the excellent etching of δ ferrite structures in particular can be observed.

Figure A.5: Columnar grains in a WAAM bead

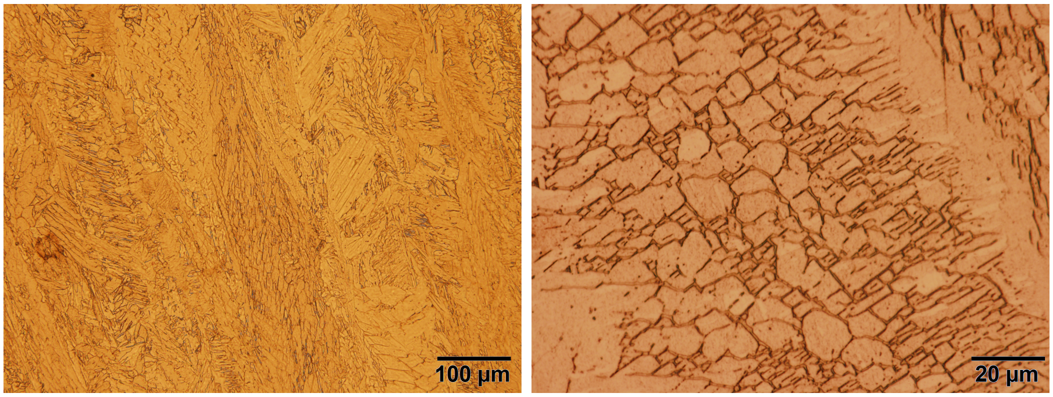

(a) WAAM sample microstructure (b) Higher magnification

Figure A.6: WAAM samples etched with Vilella's reagent

A.3 Fry's Reagent

While Vilella's reagent gave very good results of the general microstructure, the length of the etching and the failure to fully visualize texture within some features led to more etchant trials. Samples were immersion etched for 10-12 seconds.

A.3.1 Powder Sample Etching

The effect of Fry's reagent on IA powder samples can be seen in Figure A.7. Fry's reagent gave very clear visualization of dendritic features in 17-4PH IA powders. A clear view of a dendritic structure in a 1.18 mm - 850 μm size range powder can be seen in Figure A.7a. However, compared to samples etched using Vilella's reagent, martensite in the samples was less clearly revealed. An example of an etched martensitic sample can be seen in Figure A.7b.

A.3.2 WAAM Sample Etching

For bulk 17-4PH samples, the effect of Fry's reagent as an etchant can be seen in Figure A.8. While the bead-substrate interface is still clearly visible (Figure A.8a), it is not as well-etched as samples etched with Vilella's reagent due to the way Fry's etches the δ ferrite stringers. However, the etching of the major microstructural constituents in the WAAM beads is very clear and well-defined using Fry's reagent at both low (Figure A.8b) and high magnifications (Figure

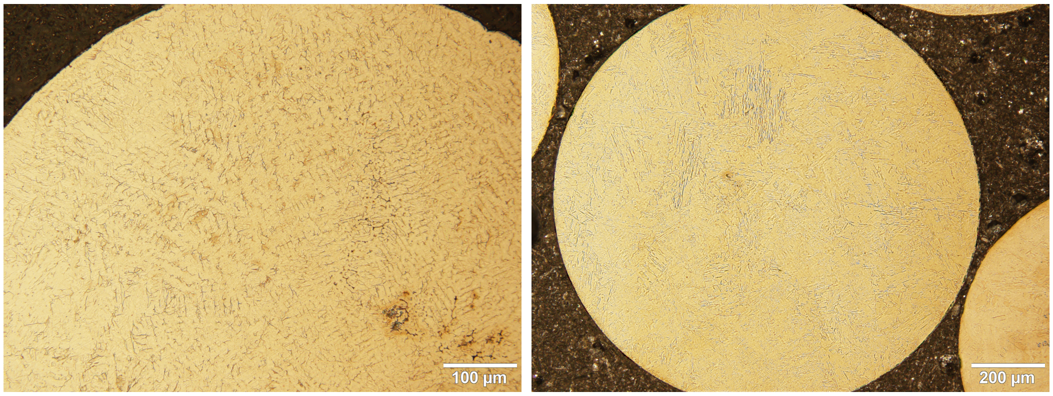

(a) A 1.18 mm - 850 μm particles with dendrites (b) A 1.18 mm - 850 μm particle with visible martensite

Figure A.7: IA powder samples etched with Fry's reagent

A.8c).

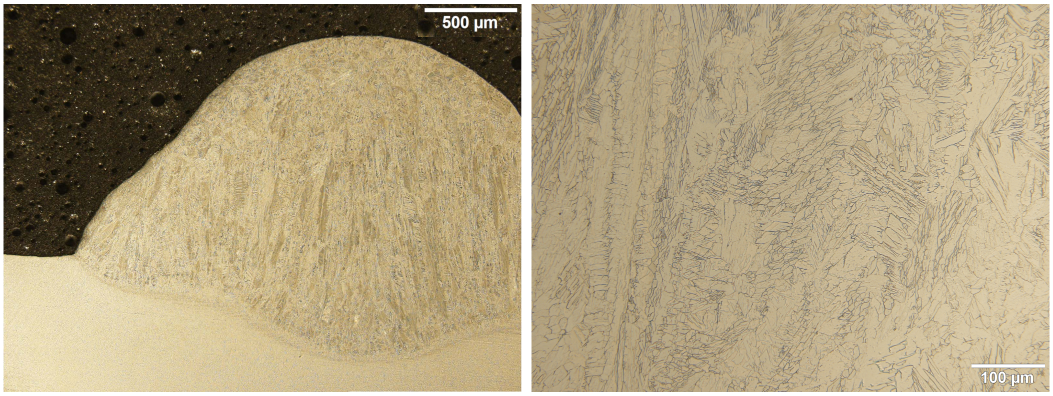

(a) Weld bead - substrate plate interface (b) WAAM sample microstructure

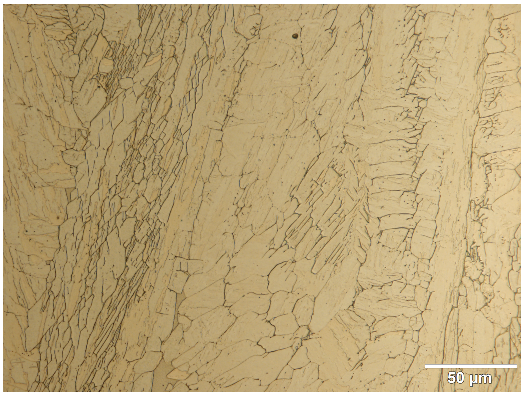

(c) Higher magnification of WAAM sample microstructure

Figure A.8: WAAM samples etched with Vilella's reagent

A.4 Etchant Recommendations

Etching of 17-4PH steel is not a trivial matter and the etchant used depends on the type of sample that is being etched. For high cooling rate samples that featured a meta-stable δ ferrite dendritic structure combined with a martensitic lathe structure, Vilella's reagent was the superior etchant for visualizing all structures. Additionally, Vilella's reagent is preferred when precise identification of weld-substrate interfaces must be done. Due to the extremely long etch times (up to 12 minutes) and volatility of the required picric acid, Vilella's is not the most suitable etchant for bulk 17-4PH samples if other etchants can be used. Fry's reagent provides an extremely clear etch of all bulk microstructure with etching times a fraction of what is required from Vilella's, making Fry's reagent the preferred etchant for all bulk samples.

Appendix B

Impulse Atomized Powder Microstructures

Microstructures from powders in the midrange powder sizes are presented here. Dendritic and martensitic particles can be seen at all these size ranges. Note also the presence of porosity in most powder particles.

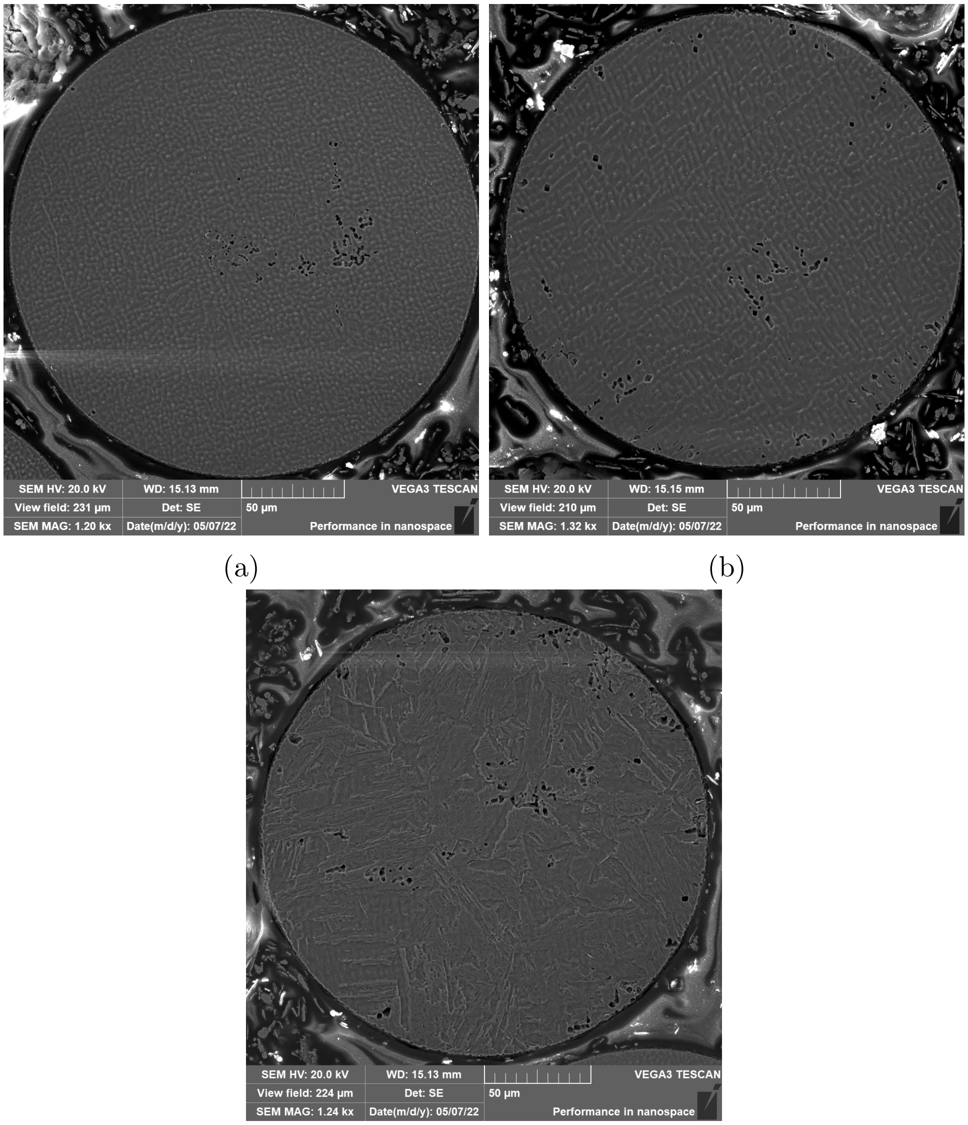

(a) (b)

(c)

Figure B.1: Microstructures in the 250 - 212 μm size range

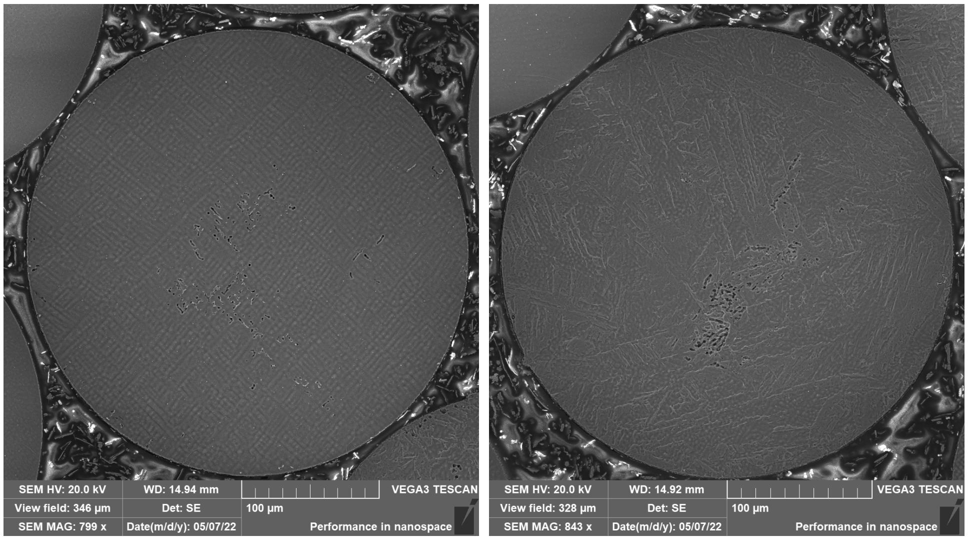

(a) (b)

Figure B.2: Microstructures in the 355 - 300 μm size range

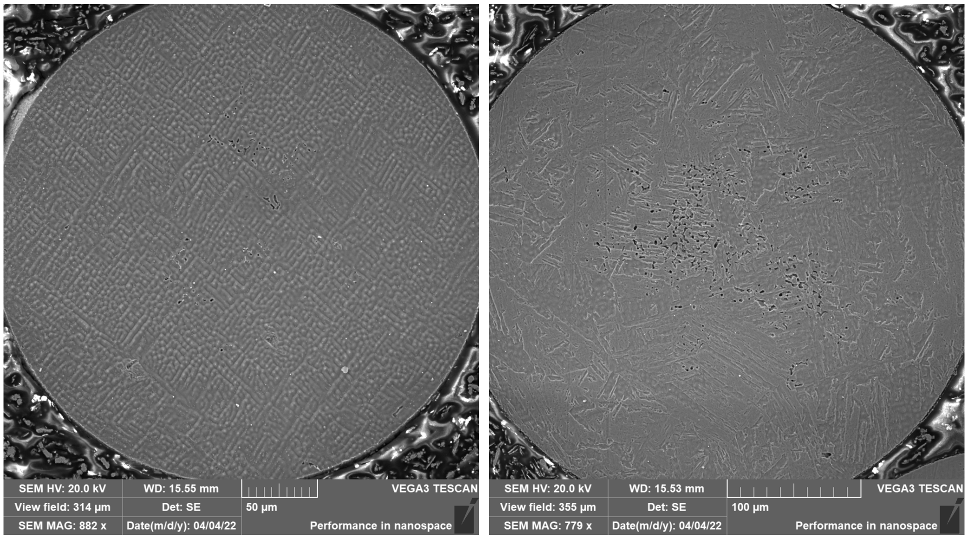

(a) (b)

Figure B.3: Microstructures in the 425 - 355 μm size range

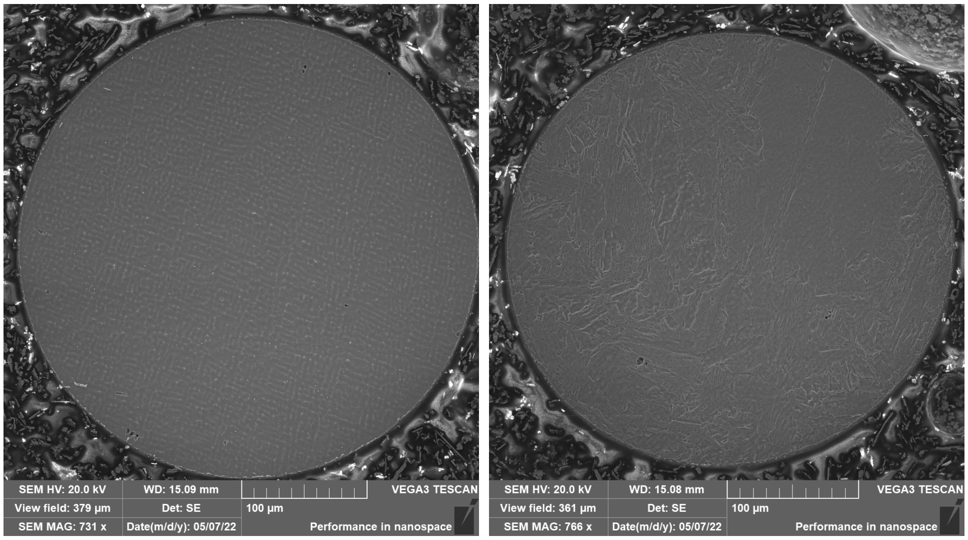

(a) (b)

Figure B.4: Microstructures in the 500 - 425 μm size range

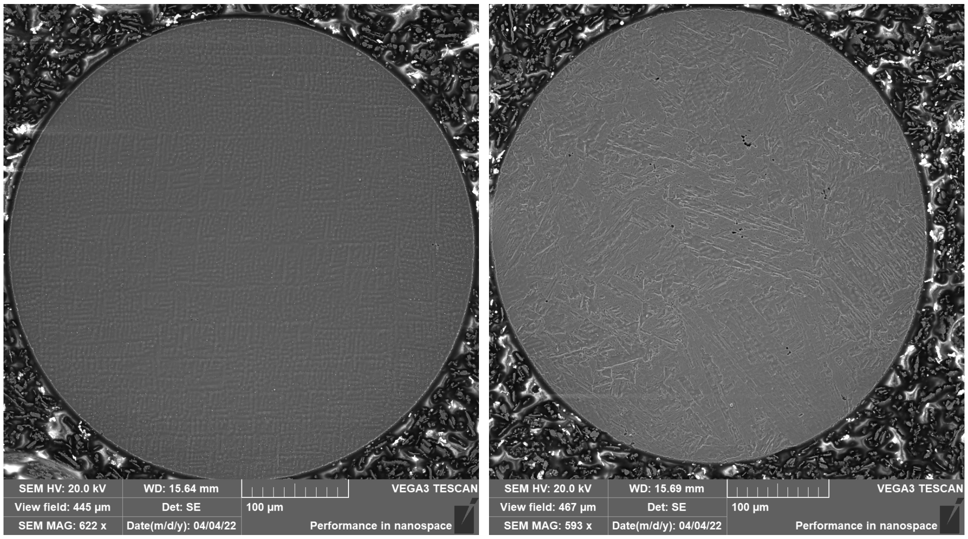

(a) (b)

Figure B.5: Microstructures in the 600 - 500 μm size range

Appendix C

Specific Heat Capacity of IA Liquid Metal

To calculate the specific heat capacity of the liquid metal, a DSC run from Netzsch laboratories was used. The full first heating C_p figure can be seen in Figure C.1. Since the cooling rates calculated for the IA powder samples were liquid cooling rates, the liquid portion of the graph after the major melting peak was used to give a specific heat capacity of 4060 $\frac{J}{kgK}$.

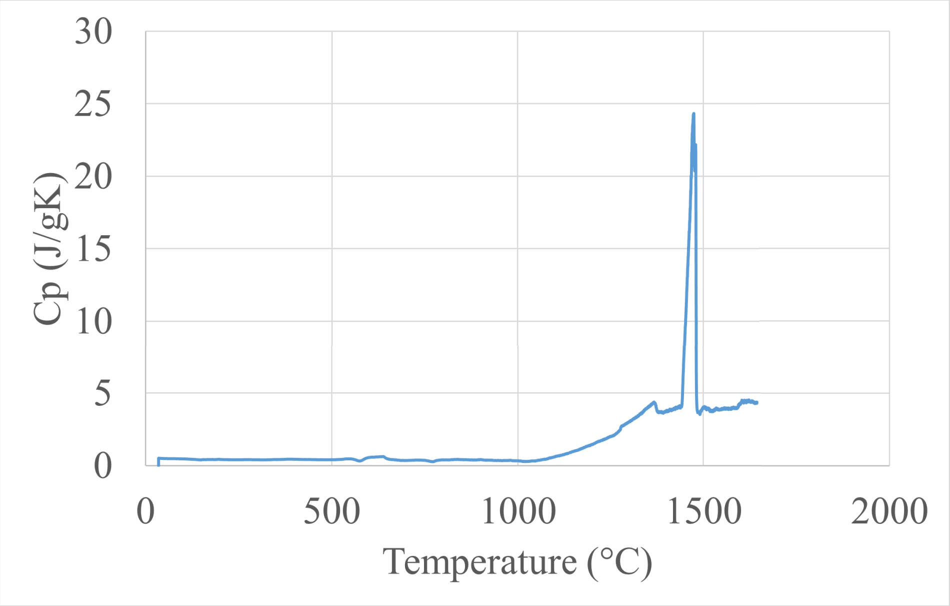

Figure C.1: C_p in first heating of 17-4 PH sample

Appendix D

DSC Modulated Heat Flow

The DSC heating curve can be used to confirm the final microstructure of the DSC sample. In Figure D.1, the modulated heat flow for the 2 $\frac{K}{min}$ welding wire sample can be seen. There are peaks at $\tilde{1}440$ °C on heating and cooling that represent the melting and solidification of the δ-ferrite phase. The second peak on cooling occurs at around 1300 °C in this sample. This second peak corresponds with values seen for the formation temperature of austenite in 17-4 PH samples [37]. EBSD of the samples showed that there is no remaining austenite in the samples at room temperature, indicating that another phase change must occur that is not captured on this modulated heat flow diagram. The transition to martensite occurs over the 130 - 32 °C range. In the Figure **??**, this temperature range is obscured and does not provide good data on any possible phase changes. It is likely, based on all other data about the alloy, that this phase change occurred.

The same phase changes shown in the heat flow graph for the 2 $\frac{K}{min}$ welding wire sample are also shown in the heat flow graphs for the rest of the samples. Heat flows can be seen for the 10 $\frac{K}{min}$, 20 $\frac{K}{min}$ welding wire and 10 $\frac{K}{min}$ test bar samples in Figures D.2, D.3, and D.4, respectively.

PH wire 2 Kmin(1).png

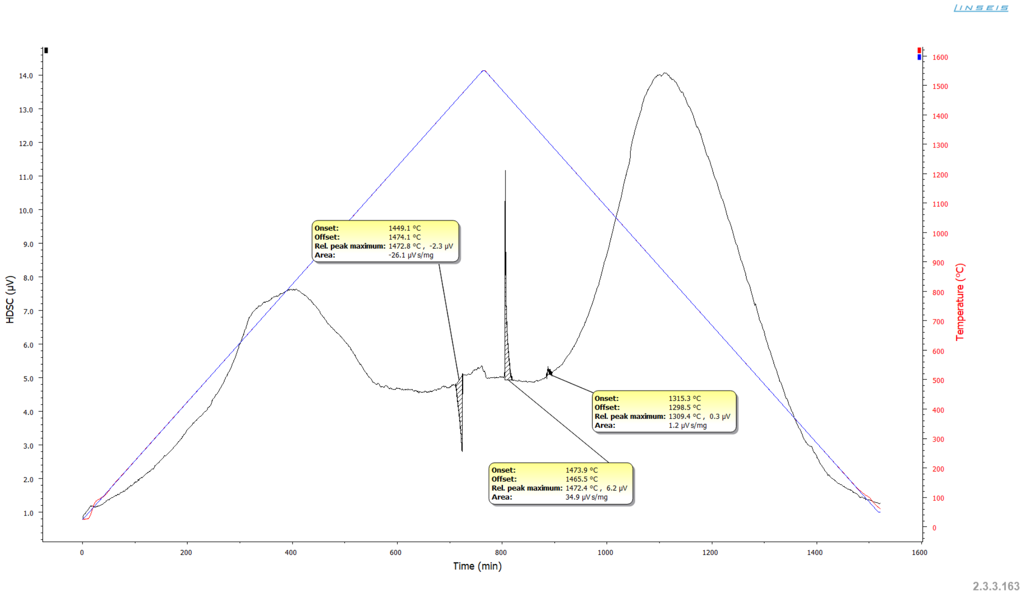

Figure D.1: Modulated heat flow for 2 $\frac{K}{min}$ welding wire

PH wire 10(2).png

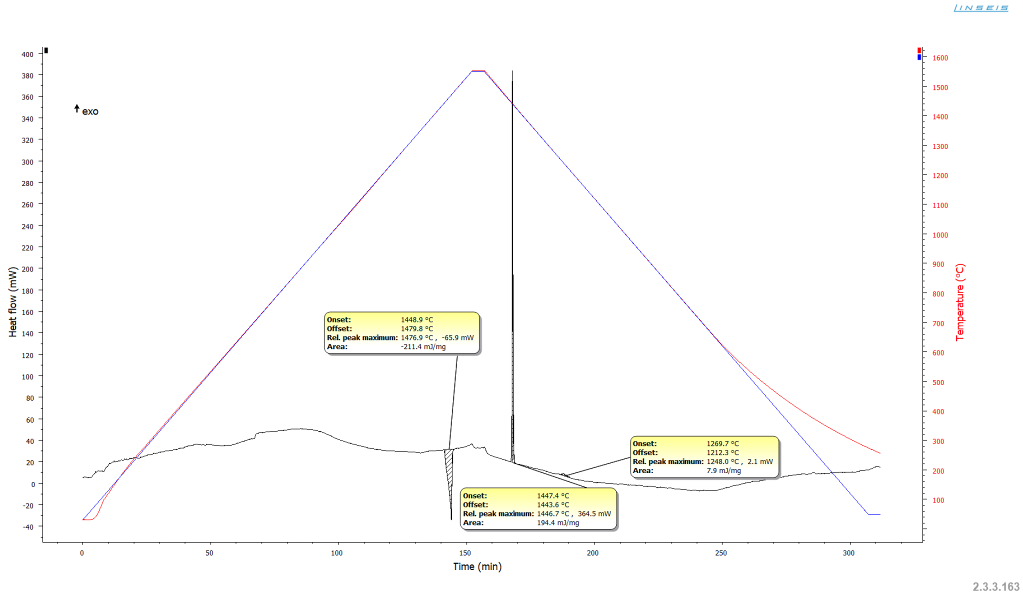

Figure D.2: Modulated heat flow for 10 $\frac{K}{min}$ welding wire

PH wire 20 Kmin(1).png

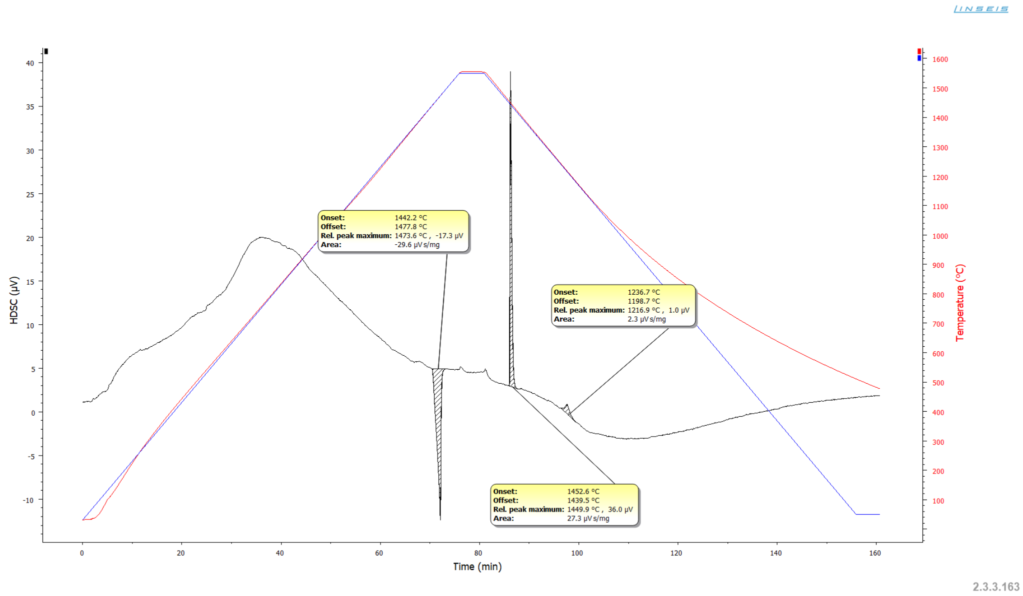

Figure D.3: Modulated heat flow for 20 $\frac{K}{min}$ welding wire

PH bar 10.png

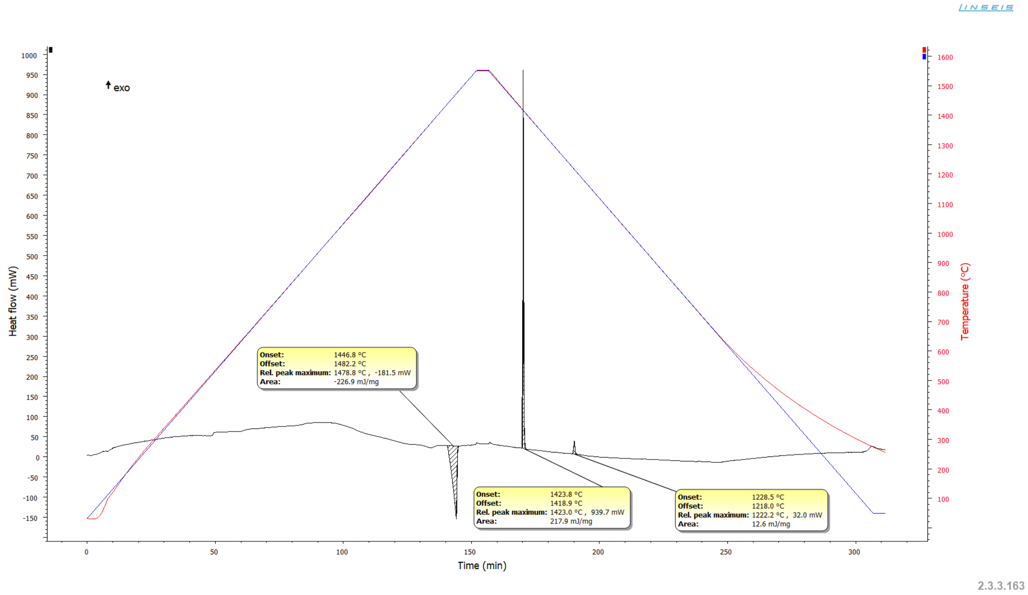

Figure D.4: Modulated heat flow for 10 $\frac{K}{min}$ test bar